SYNTHESIS AND CHARACTERISATION OF ZEOLITES FOR POTENTIAL USE AS SUPPORTS FOR LOW-TEMPERATURE FISCHER-TROPSCH WAX HYDROCRACKING CATALYSTS

by

KHUTSO MOKAMI

DISSERTATION

Submitted in partial fulfilment of the requirements for the degree of

MASTER OF SCIENCE

in

CHEMISTRY

in the

FACULTY OF SCIENCE AND AGRICULTURE

(School of Physical and Mineral Sciences)

at the

UNIVERSITY OF LIMPOPO

SUPERVISOR: Prof. M. P. Mokhonoana

2015

Dedication

To the almighty God, My mother Asinah Mosibudi Mokami, my siblings Khomotso Phuti Mokami and Kgothatso Mokami, my daughters Kgotlelelo and Katlego and to my grandmother Caroline Mokami.

Declaration

I declare that the dissertation hereby submitted to the University of Limpopo, for the degree of Master of Science in Chemistry has not previously been submitted by me for a degree at this or any other university; that it is my work in design and in execution, and that all material contained herein.

…….. ……..

Surname, Initials (title) **Date**

Acknowledgements

First off I would like to thank my supervisor Prof. M. P. Mokhonoana for his dedicated support, guidance and enduring patience during the course of this work. I would also like to thank the following people and institutions for every help they offered, without them it was going to be very difficult for this work to be completed successfully:

- Prof J. Dunlevey and Ms T. Makhohliso at the University of Limpopo Geology department for XRD analysis.
- Mr T. N. Phahlaamohlaka at University of Witwatersrand Chemistry department (Catomat) for BET surface area measurements analysis.
- Dr R. Brosius at the University of Cape Town Chemical Engineering department for catalytic activity experiments.
- The Physics department at the University of Cape Town and Dr P. B. Ramatsetse at the University of Pretoria for SEM analysis.
- The University of Cape Town for a top-up to purchase a new Parr reactor after our home-built reactor broke down.
- The Chemistry department at University of Limpopo for offering me an opportunity to do post-graduate degree (MSc) at their instuition and helping me throughout from the day I registered this degree.
- SASOL Inzalo foundation and DST-NRF centre of excellence in catalysis (C* change) for financial support.
- Above all, I would like to thank the almighty God for giving me all the strength and for being with me through good and bad.

Abstract

In this study, the use of 10-member ring zeolites with different silica-to-alumina ratios (SARs) as supports for palladium (Pd) to produce hydrocracking catalysts was investigated. The syntheses of zeolites ZSM-22, ZSM-48, ZBM-30 and ZSM-23 were carried out under hydrothermal conditions, and the resulting materials were characterised with XRD, SEM and BET surface area measurements, prior to activity tests. Successful synthesis of ZSM-48 and ZBM-30 remained elusive for the major part of this study, and these zeolites could therefore not be catalytically tested.

The XRD patterns showed pure ZSM-22 materials with different SARs (60, 80 and 120) were successfully synthesised using hexamethylenediamine (HMDA) as a structure-directing agent (SDA) and a synthesis gel with pH 12. However, at synthesis gel pH 13, cristobalite and ZSM-5 impurity phases tend to form in addition to ZSM-22. Relative % XRD crystallinity of the materials prepared at synthesis gel pH 12 decreased with a decrease in SAR, and there was no specific trend for the response of a particular SAR to changes in pH from 12 to 13. SEM micrographs showed needle-shaped crystals with lengths in the range 0.6 - 1.2 µm. The BET surface area of the ZSM-22 with SAR of 60 was found to be 189 m^2/g, which is around the theoretical BET surface area of ZSM-22 materials and the presence of impurities lowered the surface area of the ZSM-22 materials.

The synthesis of ZBM-30 using triethylenetetramine (TETA) and a (1 TETA : 1 pyrrolidine) mixture as SDAs was also attempted. The XRD patterns showed that a completely amorphous material was obtained when using TETA as SDA and ZSM-39 was produced when using the mixture as SDA. The XRD patterns revealed that impurity-free ZSM-23 materials were successfully synthesised with SAR > 60, and that with SAR of 60, ZSM-5 was produced instead. Relative % XRD crystallinity of the impurity-free ZSM-23 materials increased with an increase in SAR from 80 to 120. SEM micrographs of the impurity-free ZSM-23 materials showed needle-shaped crystals of around 0.9 µm in length. The predominantly ZSM-5 material had the highest BET surface area compared to the impurity-free ZSM-23 materials. ZSM-48 synthesis was attempted using HMDA (produced ZSM-22), pyrrolidine (produced ZSM-23) and hexamethonium bromide ($HMBr_2$) as SDAs. The XRD and SEM

analysis showed only $HMBr_2$ successfully directed the synthesis of impurity-free crystalline ZSM-48 at prolonged synthesis time of 168 h. ZSM-48 crystals were also needle-shaped and 4.2 - 11.3 µm in length.

The incipient wetness impregnation method was used to achieve 0.5 wt. % Pd loadings on the catalysts. The hydrocracking of *n*-hexadecane (*n*-C_{16}) over the catalysts was studied at conditions typical of catalytic cracking of LTFT products. At 225 ^{o}C, the Pd/ZSM-22 (80) and Pd/ZSM-23 (80) were highly selective to cracking products, with excessive secondary cracking occurring over these catalysts, as indicated by the C_4/C_{12} ratios of 11.3 and 5.2, respectively. Excessive secondary cracking (C_4/C_{12} = 11.7) was also observed over Pd/ZSM-23 (60). However, the Pd/ZSM-22 (60) and Pd/ZSM-23 (120) catalysts achieved a C_4/C_{12} ratio close to 1.0, suggesting closeness to ideal hydrocracking behaviour. The Pd/ZSM-22 (60) (C_4/C_{12} of 1.9) catalyst, was physically mixed with Pd/ZSM-5 (90) (C_4/C_{12} = 6.4) and catalytically tested for the hydrocracking of *n*-C_{16}. This Pd/ZSM-5/ZSM-22 catalyst achieved a remarkable C_4/C_{12} = 1.1, which is less than what was achieved over the individual catalysts. On the basis of the C_4/C_{12}, this catalyst's behaviour is close to that of an ideal hydrocracking behaviour. In summary, Pd/ZSM-22 (80), Pd/ZSM-22 (120) and Pd/ZSM-23 (80) catalysts are promising for diesel-selective catalysis and need further exploration.

Table of contents

List of figures

List of tables

List of abbreviations and acronyms

ASA	Amorphous silica-alumina
BEA	Zeolite β
BET	Brunauer-Emmett-Teller
CHA	Chabazite
ERI	Erionite
EU	Edinburgh University
FAU	Faujasite
FCC	Fluid catalytic cracking
FER	Ferrierite
FT	Fischer Tropsch
FTIR	Fourier-transform infra-red
$HMBr_2$	Hexamethonium bromide
HMDA	Hexamethylenediamine
i-C_{16}	Isomerised hexadecane
IUPAC	International Union of Pure and Applied Chemistry
IZA	International Zeolite Association
LTFT	Low-temperature Fischer-Tropsch
MFI	Mobil Five
MTG	Methanol-to-gasoline
MTO	Methanol-to-olefins
MTT	Mobil Twenty Three

NH_3-TPD	Ammonia temperature-programmed desorption
NMR	Nuclear magnetic resonance
OFF	Offretite
SAR	Silica-to-alumina ratio
SDA	Structure-directing agent
SEM	Scanning electron microscopy
TETA	Triethylenetetramine
TON	Theta-1
ULSD	Ultra-low sulphur diesel
USY	Ultra stable Y zeolite
VGO	Vacuum gas oil
WHSV	Weight hourly space velocity
XRD	X-ray diffraction
ZSM	Zeolite Socony Mobil

CHAPTER 1

General Introduction

1.1 Discovery and definition of zeolites

Zeolites were discovered in 1756 by a Swedish mineralogist, Axel Fredrik Cronstedt [1]. The name “zeolite” is derived from the two Greek words “zeo” and “lithos”, meaning “to boil” and “stone”, respectively. Thus, the word “zeolites” means boiling stones, in accordance with Cronstedt’s observation that heating stilbite in a blowpipe produced water vapour [1]. Since this discovery, several mineralogists and scientists contributed to the development of zeolites [2, 3].

1.2 Structures of zeolites

Zeolites are crystalline, microporous, hydrated aluminosilicates based on a 3-dimensional framework of AlO_4^{5-} and SiO_4^{4-} tetrahedra linked by sharing the corner oxygen atoms. Their cavities or channels are occupied by water and exchangeable cations [3]. A representative empirical formula of a zeolite is

$$M_{2/n}O.\ Al_2O_3.\ x\ SiO_2.\ y\ H_2O,$$

where x and y are the numbers of silica units and water molecules per unit cell, respectively, while M represents a Group I or II exchangeable cation with valence n [3, 4]. The Si/AI ratios of zeolites vary from 1 to ∞, because according to the Lowenstein rule, AI-O-Al links are forbidden [4]. The Lowenstein rule clearly indicates that when two tetrahedra are linked together by an oxygen atom and one centre is occupied by aluminium atom, then the only allowed atom to occupy the other centre must be an atom with valence of 4 or more [4]. The building units of zeolites, namely, primary building units (tetrahedron), secondary building units (*e.g.,* sodalite, pentasil) and tertiary building units (comprised of the same or different arrangements of secondary building units) are shown in figure 1.1 [5].

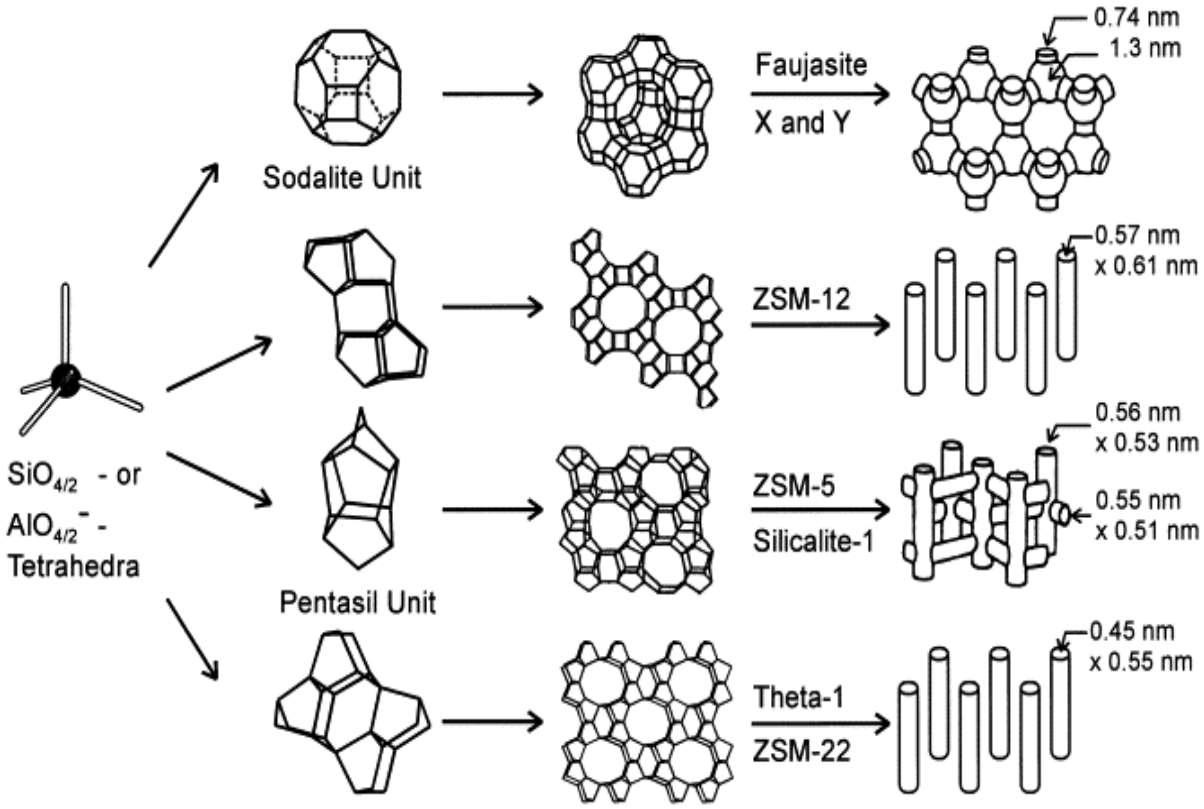

Figure 1.1 Structure, micropore system and dimensions of zeolites [5].

Figure 1.1 shows the zeolite structures with different micropore systems and dimensions, built from different secondary building units, *e.g*., the structure of faujasite (FAU) results from the connection of sodalite *via* their hexagonal faces [5]. There are over 40 natural zeolites and 213 synthetic zeolites, as reported by the structure commission of International Zeolite Association (IZA) [6]**.** Natural zeolites such as offretite (OFF), ferrierite (FER), erionite (ERI) and chabazite (CHA) have been known for almost 250 years as aluminosilicate minerals. Their occurrence could be due to geological processes [7]. They crystallise from the hydrothermal or hot-spring activity, which involves reaction between solutions and basaltic lava flows [8]. The natural zeolites are named based on where they were discovered or the scientist who discovered them and not based on their composition or structure [3, 7]. On the other hand, synthetic zeolites are named based on the connectivity of their tetrahedral atoms using topological symmetry and not considering the changes in the unit cell size and symmetry [8].

These naturally-occurring zeolites are of limited value because they contain undesired impurity phases, lack uniformity as nature did not optimise their properties for catalytic applications [5, 8]. Examples of synthetic zeolites are ZSM-5 (MFI), ZSM-23 (MTT), ZSM-22 (TON), zeolite Y (FAU), zeolite beta (BEA) and many more [2]. The three letter code (in brackets) attached to each zeolite above is based on their topology [9]. Zeolites are also classified according to their pore sizes as illustrated in figure 1.2.

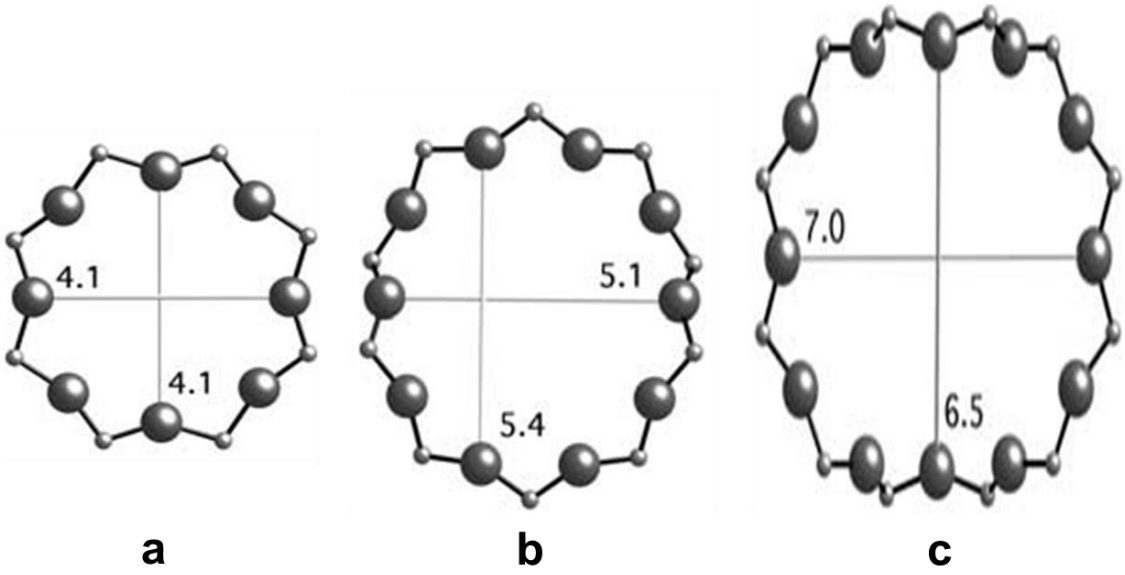

Figure 1.2 Classification of zeolites based on their pore sizes: (a) Small pore, (b) Medium pore and (c) Large pore [9].

The size of a zeolite pore is determined by the number of tetrahedra linked together, *e.g.,* eight tetrahedra form an 8-member ring (small pore*, e.g.,* Zeolite A), ten tetrahedra form a 10-member ring (medium pore, *e.g.,* ZSM-5) and twelve tetrahedra form a 12-member ring (large pore*, e.g.,* mordenite) (figure 1.2) [9].

Aluminosilicate zeolites are formed by isomorphous substitution of Al^{3+} for Si^{4+}. The substitution can be performed either during synthesis or using a post-synthesis method, and it imparts a negative charge to the zeolite framework [8 - 10]. This negative charge can be counter-balanced by a metal, non-metal or organic cation [10].

1.3 Hydrothermal synthesis of zeolites

Hydrothermal synthesis refers to the synthetic reactions conducted at higher temperature (100 - 1000 ^{o}C) and pressure (10 - 1000 bar) using water as a solvent within a sealed container or high-pressure autoclave [8]. The first hydrothermal synthesis of zeolites in the laboratory was carried out by St. Claire-Deville [11] in 1862 when he synthesised the zeolite named levynite in the late 1940s, Barrer [12] and Milton [13] synthesised zeolites by converting mineral phases under the action of strong salt solutions at fairly high temperatures (170 - 270 ^{o}C). The hydrothermal synthesis of zeolites carried out by the likes of St. Claire-Deville, Barrer and Milton, utilised only inorganic reaction components [11 - 13].

The use of quaternary ammonium cations as structure-directing agents (SDAs) was introduced by Kerr *et al.* [14], when they synthesised a silica-rich version of zeolite A, named zeolite ZK-4 in 1961 [14]. Mobil Oil Corporation first synthesised high-silica zeolite β, with the silica-to-alumina ratio (SAR) in the range 10 < SAR < 200 using tetraethylammonium as SDA [15], followed by the discovery of another high-silica zeolite ZSM-5 [16]. Following the development of the synthesis of zeolites using quaternary ammonium cations, mostly in the 1960s, several new families of zeolite-like or zeolite-related materials were discovered [17].

Synthetic zeolites are conventionally synthesised from aluminosilicate gels in the presence of SDAs or templates under hydrothermal conditions [18]. Different cations or organic SDAs can be used to synthesise different or iso-structural zeolites. Linear (unbranched) organic SDAs are used to synthesise 1-dimensional zeolites such as ZSM-22 and ZSM-48 whilst branched organic SDAs are used to synthesise 2-dimensional and 3-dimensional zeolites such as FER, ZSM-5, *etc.* [16, 17]. Depending on the method followed in synthesising a zeolite, different ways of mixing or the order of addition of reactants can be used. Figure 1.3 shows a schematic representation of how zeolites are synthesised.

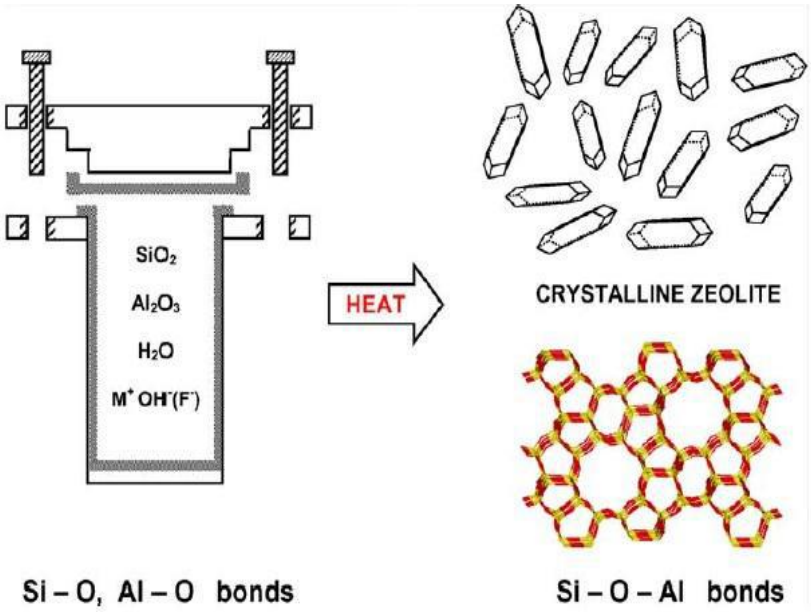

Figure 1.3 Hydrothermal synthesis of zeolites [19].

A number of changes take place during the hydrothermal synthesis (depicted in figure 1.3). Different amorphous silica and alumina sources are mixed together with a cation source, usually in a basic medium. The aqueous reaction mixture is heated at higher temperature (typically 100 ^{o}C) in a sealed autoclave. During this synthesis the reactants remain amorphous until the temperature reaches the desired value. After the above “induction period”, nucleation occurs and crystalline zeolite product can be detected. As time progresses, essentially all the amorphous material is converted into an approximately equal mass of zeolite crystals, and the formed zeolite crystals are then recovered by filtration, followed by washing and drying [19].

It is recommended that the autoclaves used in the synthesis of zeolites be filled to between 30 and 70 volume % in the case of aqueous reaction mixtures, and heated to between 100 and 200 ^{o}C in order to maintain a liquid phase and leave sufficient space to maintain the autogenous pressure generated [20].

1.4 Catalytically important properties of zeolites

The catalytic properties (activity, product selectivity and shape selectivity) of zeolites are related to their physicochemical properties such as acidity, topology, morphology, chemical composition, surface area, the ability to separate reactants from products, and high adsorption capacity [21]. These catalytic properties are of great importance in a wide range of industrial and agricultural applications. A brief description of structural properties that are central to zeolite catalysis is outlined in sections 1.4.1 - 1.4.4.

1.4.1 Zeolite acidity

Zeolites are solid acids, with the acid strength equivalent to that of liquid acids. However they are less corrosive, less toxic, environmentally-friendly and can be easily regenerated after deactivation in catalytic reactors [22, 23]. Brønsted acid sites are formed when the negative charge produced by the isomorphous substitution of Si^{4+} by Al^{3+} is compensated by a proton (introduced by ion-exchange with NH_4^+ ions followed by thermal decomposition) [5, 24]. Figure 1.4 shows the Brønsted acidity of a zeolite that results from the hydroxyl bridge forming between the aluminium and silicon atoms in the framework [25].

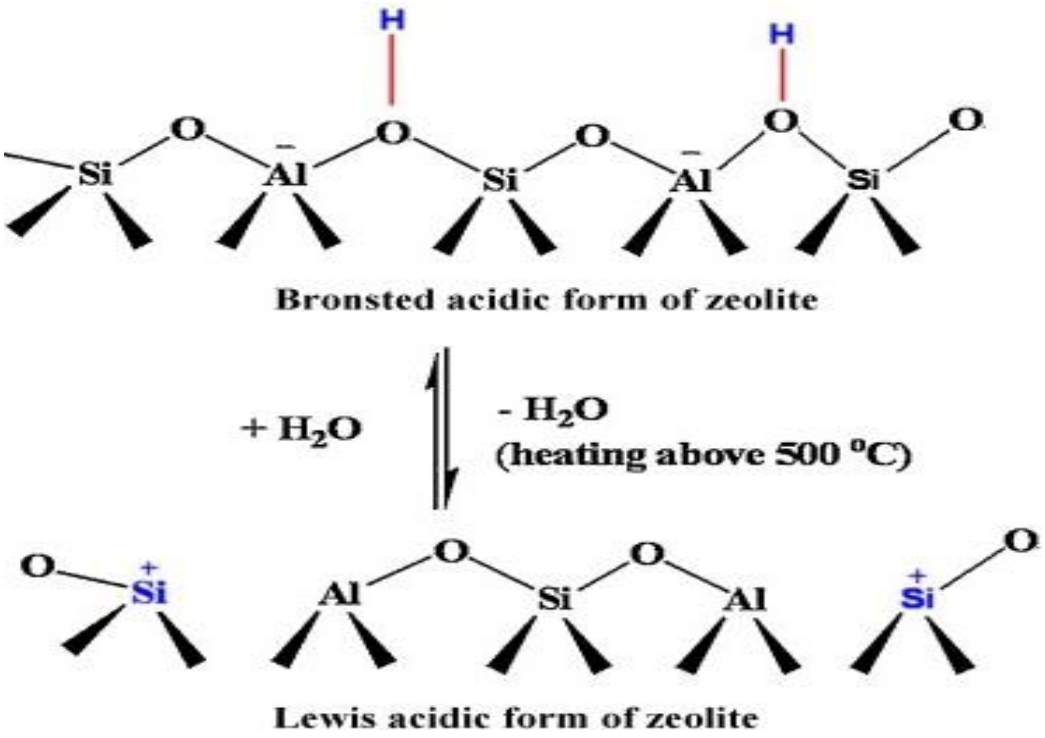

Figure 1.4 Brønsted acid and Lewis acid sites of zeolites [25].

Also shown in figure 1.4 is the Lewis acidity, resulting from the dealumination of the zeolite by either steaming or calcination. This causes the hydroxyl bridge to break, thereby producing defects in the framework structure, with a consequent migration of aluminium atoms to the outer surface of the zeolite [5, 25, 26].

There is a strong correlation between the SAR and zeolite acidity, wherein the acidity decreases with the increase in SAR of the zeolite [22, 26]. This correlation arises from the tetrahedrally-coordinated aluminium atom, which corresponds to one Brønsted acid site. Thus, the number of acid sites is directly related to the framework aluminium content of a zeolite [5, 22].

Dempsey [27, 28] demonstrated that the acid strength per aluminium is a maximum when the framework aluminium ions have no second nearest neighbour aluminium. Zeolites that are essentially devoid of aluminium still show some presence of acidity, which is due to the terminal hydroxyl groups on the zeolite exterior [29]. The acid strength of OH groups in the H-form of zeolites not only depends on SAR, but also on the degree of cation exchange and the degree of dehydroxylation [29]. Acidic functions (*i.e.,* the Brønsted acid sites of the zeolite) play an important role in several industrial processes such as isomerisation,

hydrocracking, alkylation, fluid catalytic cracking (FCC), methanol-to-gasoline (MTG) and methanol-to-olefins (MTO), just to name a few [30]. The work of Giannetto *et al.* [31] has also revealed the role of zeolite acidity in the hydrocracking and hydroisomerisation of *n*-heptane over Pt/H-Y zeolites, who observed lower activity at higher SAR. It is therefore important to measure the acidity of zeolites in order to understand the effect of acidity on their catalytic performance in industrial processes [23, 30]. Three factors are important in correlating zeolite acidity and catalytic activity, *viz.,* the total number of acid sites, the ratio of Brønsted to Lewis acid sites and the acid strength distribution [32].

The acidity of zeolites is conventionally investigated using physicochemical techniques such as ammonia temperature programmed desorption (NH_3-TPD), Fourier transform infrared (FTIR) spectroscopy of adsorbed pyridine, and solid-state nuclear magnetic resonance (^{27}Al NMR) spectroscopy [5, 23, 33]. The information provided by these techniques is briefly described in sections 1.4.1.1 - 1.4.1.3.

1.4.1.1 Ammonia temperature programmed desorption

The NH_3-TPD involves chemisorption of gaseous ammonia onto a zeolite at a fixed temperature, *e.g.*, 100 ^{o}C. This is followed by a programmed ramping of the temperature while monitoring the amount of ammonia that desorbs from the zeolite as temperature increases [33]. The position of the peaks in the TPD profile determines the strength of the acid sites, thus allowing the acid site distribution to be classified as weak, intermediate and strong. Peaks in the TPD profile at lower temperatures (around 180 ^{o}C) correspond to weak acid sites, while those around 250 ^{o}C correspond to intermediate acid sites, and those at higher temperatures (around 500 ^{o}C) correspond to strong acid sites [33]. The drawback of the NH_3-TPD technique is its inability to differentiate between Brønsted and Lewis acid sites, as NH_3 adsorption is not specific to the Brønsted acid sites [33].

1.4.1.2 Fourier transform infrared spectroscopy

The FTIR spectroscopic studies using pyridine as a probe molecule relies on the interaction of pyridine with Brønsted and Lewis acid sites on the zeolite [5, 23]. Infrared bands at 1545 cm^{-1} correspond to pyridine adsorbed on Brønsted acid sites, while those in the range 1440 - 1465 cm^{-1} correspond to pyridine adsorbed on Lewis acid sites [5, 23]. Therefore, it is possible to distinguish between Brønsted acid sites and Lewis acid sites based on IR spectroscopy. The vibrational modes of surface hydroxyl groups can also be detected at OH stretching in the region 3800 - 2500 cm^{-1} [23].

1.4.1.3 Solid-state nuclear magnetic resonance spectroscopy

The ^{27}Al MAS NMR spectroscopy gives information about the nature of the coordination sphere of aluminium in zeolites [23, 33]. In the ^{27}Al MAS NMR spectrum of a zeolite, a peak between 55 ppm and 85 ppm corresponds to the tetrahedrally-coordinated Al species associated with the Brønsted acid sites, and a peak between -10 ppm and 20 ppm corresponds to the octahedrally-coordinated Al species associated with the Lewis acid sites [23, 33].

1.4.2 Morphology of zeolites

The morphology (appearance, size and shape) of zeolite crystals depends on parameters such as the gel composition, chemistry at the crystal surface and the kinetics of crystal growth [34]. It is often studied using scanning electron microscopy (SEM) [34]. It is important to study the morphology because it affects the catalytic activity and selectivity. Diffusion limitations of guest molecules in micropores, the catalytic adsorption and other guest-transport dependent performances of molecular sieve materials are strongly influenced by particle morphology [35].

The precise control of the crystal morphology and the direction of the crystal growth are of great importance and interest [35]. The synthesis of a zeolite with an appropriate crystal size has, therefore, to be a compromise between selectivity

and activity [36]. Several catalytic reactions involving zeolites are sensitive to zeolite's crystal size and the crystal size governs the selectivity in these reactions. For example, nanocrystalline ZSM-5 showed a higher conversion (8.75 %) in *n*-hexane cracking than microcrystalline ZSM-5 (3.5 %) [36]. This observation was attributed to mass transfer limitations, since the zeolite nanocrystals effectively exclude mass transfer limitations compared to zeolite microcrystals. The authors' reasoning was also supported by the product distribution obtained, with nanocrystalline ZSM-5 yielding higher alkene/alkane ratios and higher selectivity to propylene than microcrystalline ZSM-5 [36].

1.4.3 Surface area and porosity

Zeolites with pore diameters in the range 0.3 - 2.0 nm are classified as microporous, while those with pore diameters in the range 2.0 - 50 nm as mesoporous, and those with pores larger than 50 nm as macroporous [9, 37, 38]. Surface areas and pore sizes of zeolites are commonly investigated using nitrogen adsorption at a temperature of -196 ^{o}C using the Brunauer-Emmett-Teller (BET) equation [39]. The external surface area is the surface that includes all the cracks which are wider and less deep as defined by Gregg and Sing [39], and can also be defined as the area available for multilayer physical adsorption. A prerequisite for heterogeneous catalysis to occur is the adsorption of reactants on the inner or outer surface of the catalyst, followed by dissociation of the reactants. This dissociation is accompanied by a surface reaction, which is often rate-determining in a catalytic reaction, and then desorption of the products [38].

The pore openings of zeolites are directly proportional to the external surface area, and affect the velocity of diffusion of reagent molecules into the channels or the product molecules out of the channels [40, 41]. As a result they affect the catalytic performance of zeolites, because the size/shape-selective catalysis in the internal surface proceeds at a lower rate for larger crystals. Side reactions occur more when the desired reaction is diffusionally retarded [41].

The role of BET surface area in the catalysis involving hydrocracking of polystyrene was demonstrated by Fuentes-Ordonez *et al*. [42]. Their study was based on catalysts designated as Pt/h-HZSM-5 (hierarchical) and Pt/FER and

catalysts with increased external surface area, namely Pt/HZSM-5 (conventional) and Pt/ITQ-6 (dealuminated FER). Table 1.1 summarises the different surface area of the conventional and treated catalysts.

Table 1.1 : Surface areas of the four different catalysts studied by Fuentes-Ordonez *et al*. [42].

Catalyst	Total surface area (m^2/g)	External surface area (m^2/g)
Pt/FER	339	158
Pt/HZSM-5 (conventional)	383	186
Pt/ITQ-6	460	436
Pt/h-HZSM-5 (hierarchical)	718	597

As shown in table 1.1, surface area analysis revealed that the treated Pt/ITQ-6 and Pt/h-HZSM-5 (hierarchical) had the highest surface areas compared to the conventional Pt/FER and Pt/HZSM-5. The BET surface areas had an effect on the activity of the catalysts and figure 1.5 below shows the results obtained with varying reaction temperature.

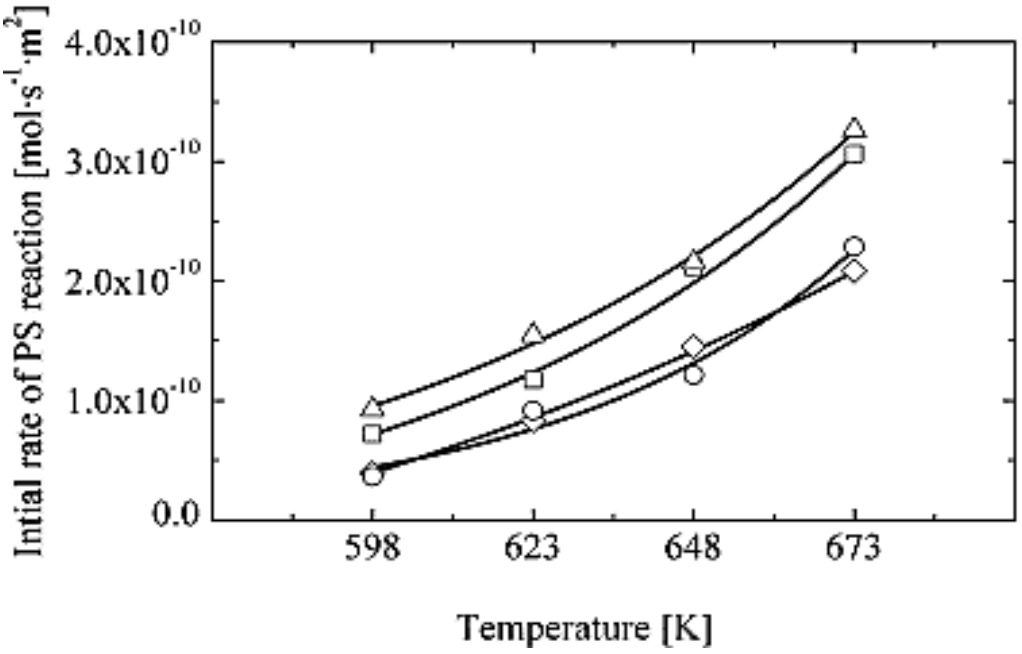

Figure 1.5 The activity as a function of the reaction temperature of catalysts: (○) Pt/HZSM-5, (◇) Pt/h-HZSM-5, (▵) Pt/FER, and (□) Pt/ITQ-6 [42].

The activity of the catalysts in terms of initial polystyrene hydrocracking rates as shown in figure 1.5 was calculated as conversion versus time. The Pt/h-HZSM-5 and Pt/ITQ-6 catalysts, with increased external surface area, were about 3 times more active than Pt/HZSM-5 and Pt/FER catalysts, suggesting that high external surface area favours high activity. This observation was ascribed to the fact that high external surface area offered lower restrictions to mass transfer and, as a consequence, the polystyrene molecules easily accessed the active sites of the catalysts. The product distribution of cracked products confirmed this observation, whereby the catalysts with high external surface area (improved accessibility to active sites) yielded less oligomers and aromatics, which was due to the easy access of the polymer to the active sites [42].

1.4.4 Shape selectivity

Weisz and Frilette [43] first described and demonstrated the concept of shape-selectivity by using artificially incorporated catalytic materials within salt forms of zeolite A in the early 1960s, and the significance of this concept was recognised immediately [43]. The active sites of zeolite catalysts are located within the pores, whose dimensions and shape may strongly influence both the reaction pathway, as well as the diffusion of reactants and products [44]. By analogy with reactions catalysed by strong acids (liquid acids), zeolites also catalyse hydrocarbon-based reactions *via* the formation of carbenium or carbonium ion intermediates. The final product distribution is influenced by steric and transport restrictions imposed by the narrow zeolite pore structure [32]. Shape-selectivity in zeolite catalysts is divided into three categories, *viz.,* reactant-, transition-state-, and product-shape selectivity. Each type of shape-selectivity is shown in figure 1.6, and briefly explained in the accompanying text [32, 43, 44]:

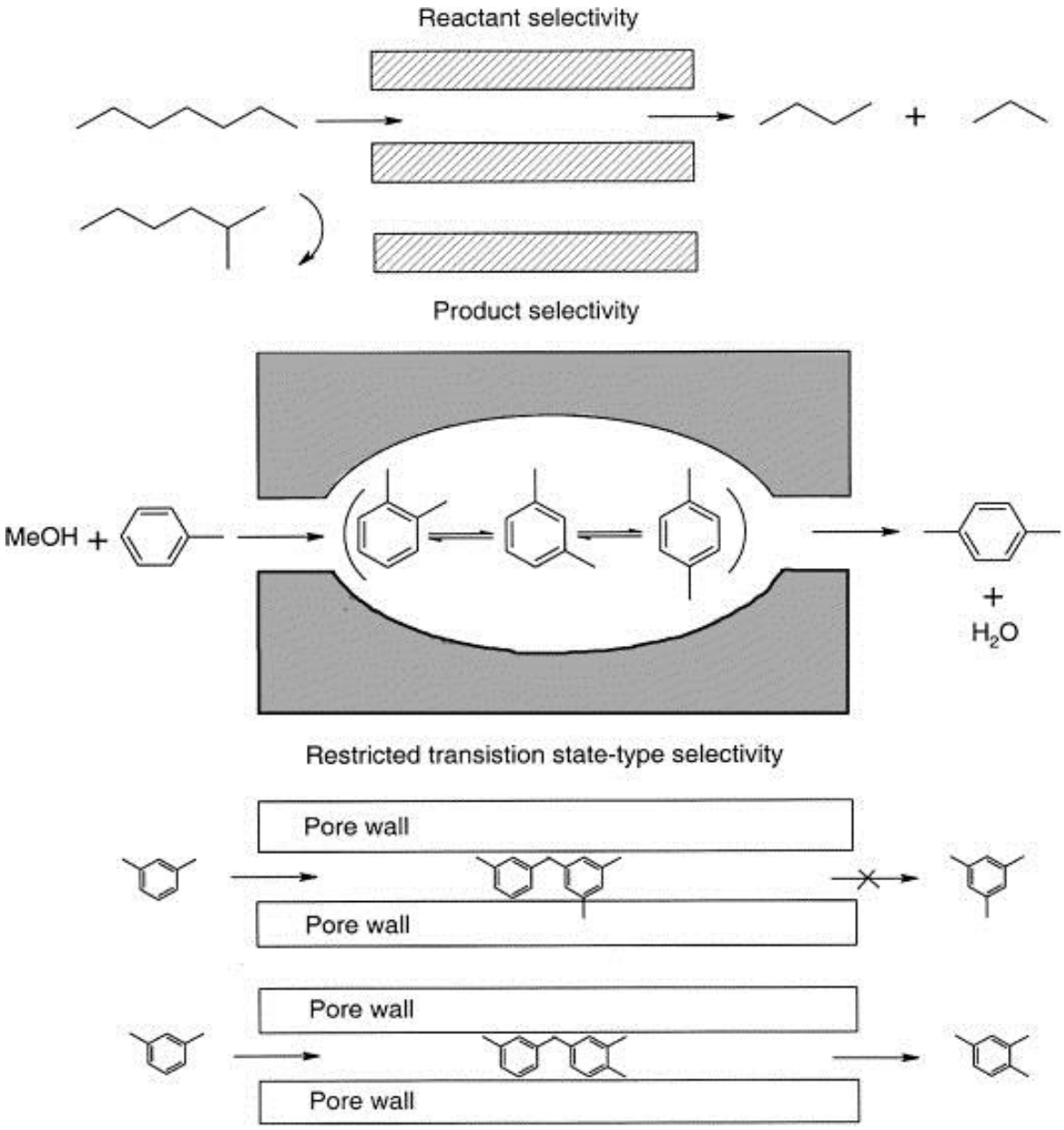

Figure 1.6. Three categories of shape selectivity in zeolite catalysts [43].

(i) Reactant shape-selectivity arises when some molecules in a reaction mixture can enter the pores and react in catalyst pores, while those which are too large to diffuse through the pores cannot react.

(ii) Product shape-selectivity occurs when some of the products formed in the catalyst pore are too bulky to diffuse out and are converted into less bulky molecules (*e.g.,* by equilibration or cracking). Large product molecules cannot diffuse out and eventually deactivate catalytic sites by blocking the pores.

(iii) Transition-state shape-selectivity occurs when certain reactions are prevented because the corresponding transition state requires more space than available inside the pores. Reactions requiring smaller transition states proceed unhindered to form smaller product molecules.

An important point to note is that reactant shape-selectivity and product shape-selectivity are identical in their nature and have their origin in mass transfer effects, which depend on the crystal size of the zeolites. The transition state shape-selectivity is an intrinsic chemical effect and independent of the crystal size [43].

Sugi [45] examined the isopropylation of biphenyl catalysed by H-mordenite zeolite and observed that shape-selectivity had an effect on product distributions, since the least bulky isomers of 4,4-diisopropylbiphenyl formed among other diisopropylbiphenyl isomers [45]. The shape-selective catalysis observed was attributed to steric restriction of the transition state and to the entrance of bulky substrates into the pores [45]. The findings demonstrate the importance of shape selectivity, since it governs the type of products formed, the type of reactants and transition state allowed during reactions. Because of shape selectivity some important reactions will not occur, and it is important to consider shape selectivity in any reaction, in order to be able to rationalise the results obtained.

1.5 Zeolites used in this study

The zeolites used in this study are 10-member ring zeolites and are 1-dimensional. The structures, dimensions and brief description of these zeolites are given in sections 1.5.1 - 1.5.4. The table 1.2 shows a comparison of the dimensions of these zeolites.

Table 1.2 : The dimensions of the zeolites used in this study.

Zeolite type	Framework type	Dimensions	Reference
ZSM-22	TON	0.45 nm x 0.55 nm	[9]
ZSM-48	MRE	0.53 nm x 0.56 nm	[46]
ZBM-30	MRE	0.53 nm x 0.56 nm	[47]
ZSM-23	MTT	0.52 nm x 0.45 nm	[9]

The pore dimensions of the zeolites differ slightly as shown in table 1.2. On the basis of these pore dimensions, one would expect similar performance and product distribution when they are used as catalytic components. Because they are synthesised differently, their properties such as surface area, porosity and acidity will differ.

1.5.1 ZSM-22

The first synthesis recipe of ZSM-22 was reported in a Mobil patent of 1985 [48]. It was synthesised using diethylamine hydrochloride or hexamethylenediamine (HMDA) as the SDA at 149 ^{o}C for a total crystallisation time of 3 - 19 days, from a synthesis gel with the following molar composition:

$$x \text{ HMDA} : y\ Na_2O : z\ Al_2O_3 : 100\ SiO_2 \quad (x = 0.01 - 2.0,\ y = 0 - 2.0,\ z = 0 - 5)$$

Its framework topology is similar to that of zeolites Theta-1, ISI-1 and NU-10, containing parallel, elliptical, 10-member ring, non-intersecting tubular pores with cross-sectional diameters of 0.45 nm x 0.55 nm, as shown in figure 1.7 [9, 49].

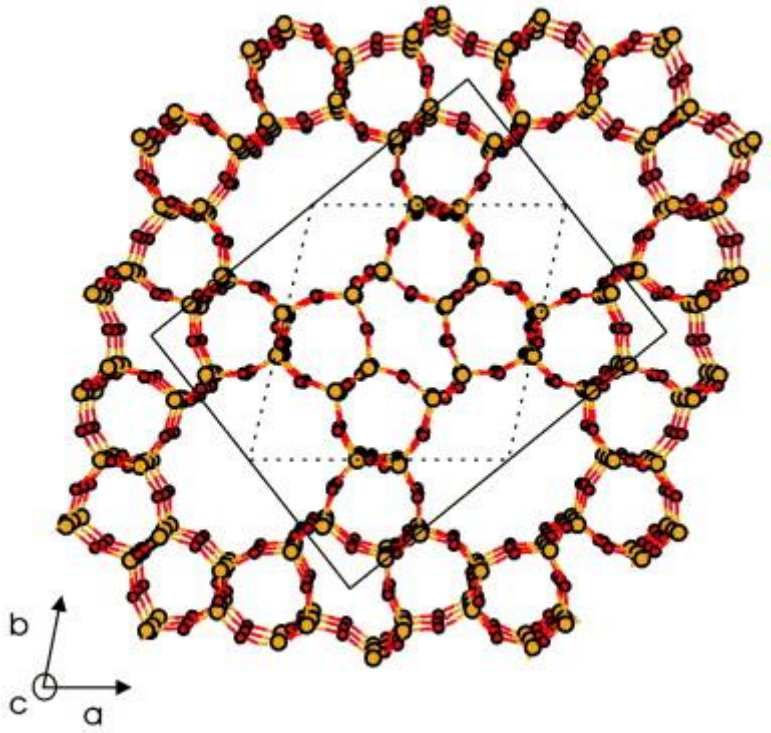

Figure 1.7. The channel system of ZSM-22 [49].

Zhang *et al.* [50] synthesised this zeolite at 160 ^{o}C for 34 h from a synthesis gel with a molar composition of:

$$y\ SiO_2 : Al_2O_3 : HMDA : KOH : x\ H_2O \quad (y = 70, 110, x = 0.2, 0.3, 1.0, 35)$$

This synthesis procedure is rated better than that reported by Dwyer [48] because of shorter crystallisation time [50]. Cristobalite and ZSM-5 usually form as impurities during the synthesis of zeolite ZSM-22 and are difficult to avoid [51]. This zeolite forms rice-like crystals up to 16 µm in length and 5 µm in width [50].

The zeolite ZSM-22 has been used in a wide range of petroleum refinery processes such as catalytic dewaxing, xylene isomerisation, alkylation of aromatic hydrocarbons and 1-butene isomerisation reactions [52]. As a good hydroisomerisation catalyst, it plays a key role in boosting the gasoline octane rating and producing diesel with high cetane number and good cold-flow properties [53]. Even though some researchers have shown that this zeolite to be highly selective to hydroisomerisation, Bouchy *et al*. [54] showed that it was poorly selective to branching of octadecane (*n*-C_{18}) (isomer yield = 60 %) compared to medium-pore zeolites such as ZBM-30 (isomer yield = 76 %) and ZSM-48 (isomer

yield = 78 %). The amount of multi-branched isomer yield of 48 % was lower than that of ZBM-30 and ZSM-48 catalysts, which was attributed to the fact that some of the multi-branched isomers were converted to cracking products.

1.5.2 ZSM-48

The zeolite ZSM-48 was found as an impurity phase in ZSM-39, with a structure based on ferrierite sheet linked via bridging oxygens located in a mirror plane [55]. Mobil scientists were the first to synthesise impurity-free ZSM-48 zeolite using a mixture of sodium silicate, sulphuric acid, tetramethylammonium chloride, water and propylamine at 320 ^{o}C for 46 h [55, 56]. ZSM-48 can also be synthesised using other SDAs such as diethylamine or dipropylamine. Suzuki *et al*. [57] prepared highly crystalline ZSM-48 from a reaction mixture containing pyrrolidine as the SDA. The OH^{-}/SiO_2 and SARs in the synthesis mixtures were identified as key factors that affect the crystallinity and purity of ZSM-48 [58]. This zeolite has a disordered high-silica structure with 1-dimension, and consists of 10-member rings, with nearly straight symmetrical channels having dimensions 0.53 nm x 0.56 nm [46]. The 2 µm crystals are rod-/needle-like and have no uniform crystal morphology [59]. The structure of ZSM-48 is best described as a random intergrowth of two different, but structurally related polytypes shown in figure 1.8 [60].

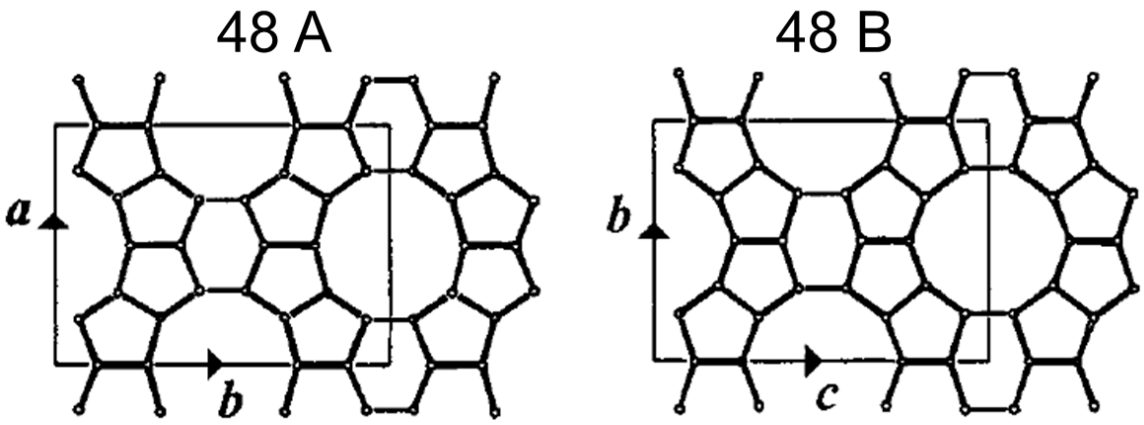

Figure 1.8. Polytypes of ZSM-48 [60].

The two polytypes are described by two layers with different topologies. Each polytype can be constructed using only one type of layer. Schlenker *et al.* [46] proposed that intergrowth between 48A and 48B can be easily achieved without changing the connectivity within the constituent layers, as the connection modes between the two polytypes are equal [46, 60]. The experimental diffraction pattern and the calculated diffraction pattern of a random intergrowth of these two polytypes are in fairly good agreement [46].

ZSM-48 exhibits unique catalytic and shape selective characteristics in the methanol-to-hydrocarbons and alkene isomerisation processes [59]. In the production of high-quality diesel fuel, ZSM-48 acts as a good dewaxing catalyst as demonstrated by Gennetti *et al*. [61] using low-temperature Fischer-Tropsch (LTFT) wax (C_{15} - C_{45}) as feed, at reaction temperatures of 358 - 371 ^{o}C and a platinum loading of 0.6 wt. %. This catalyst produced quality diesel with cold-flow properties having low pour point [(-21) - (-34) ^{o}C] and cloud point [(-8.6) - (-3.1) ^{o}C] [61]. Good isomer yields of 56 - 78 % were also obtained using this catalyst during the hydrocracking and hydroisomerisation of long *n*-alkanes such as *n*-C_{18} [54].

1.5.3 ZBM-30

ZBM-30 is a 10-member ring, 1-dimensional zeolite [62]. It is similar in structure to the zeolites ZSM-48, EU-2, EU-11 and ZBM-30, with dimensions of 0.53 nm x 0.56 nm. This group of zeolites is consequently referred to as the ZBM-30 family of zeolites [47]. Due to the uncertainty on the exact structure of the ZBM-30, there is no IUPAC code assigned to this zeolite and its related zeolites (*i.e.,* ZSM-48, EU-2 and EU-11) [63]. It is synthesised using triethylenetetramine (TETA) as an organic SDA [45]. Other organic amines used as SDAs for its synthesis include alkylamines, alkyldiamines, alkyltriamines, alkyltetramines, alkylpentamines, alkylhexamines, as well as pyrrolidine and its derivatives [62]. ZBM-30 has characteristic X-ray diffraction peaks listed in Table 1.3.

Table 1.3 : X-ray diffraction data of ZBM-30 [62].

d (nm)	I/I_0
1.160	36
1.082	15
0.580	11
0.418	100
0.387	79
0.284	16

As a catalyst or catalyst support, ZBM-30 may be useful for the transformations of hydrocarbons and more particularly in catalytic dewaxing reactions [62]. Bouchy *et al.* [54] investigated the activity of ZBM-30 in the hydroisomerisation of *n*-C_{18} in comparison with catalysts based on EU-2 and EU-11, as a function of contact time (figure 1.9).

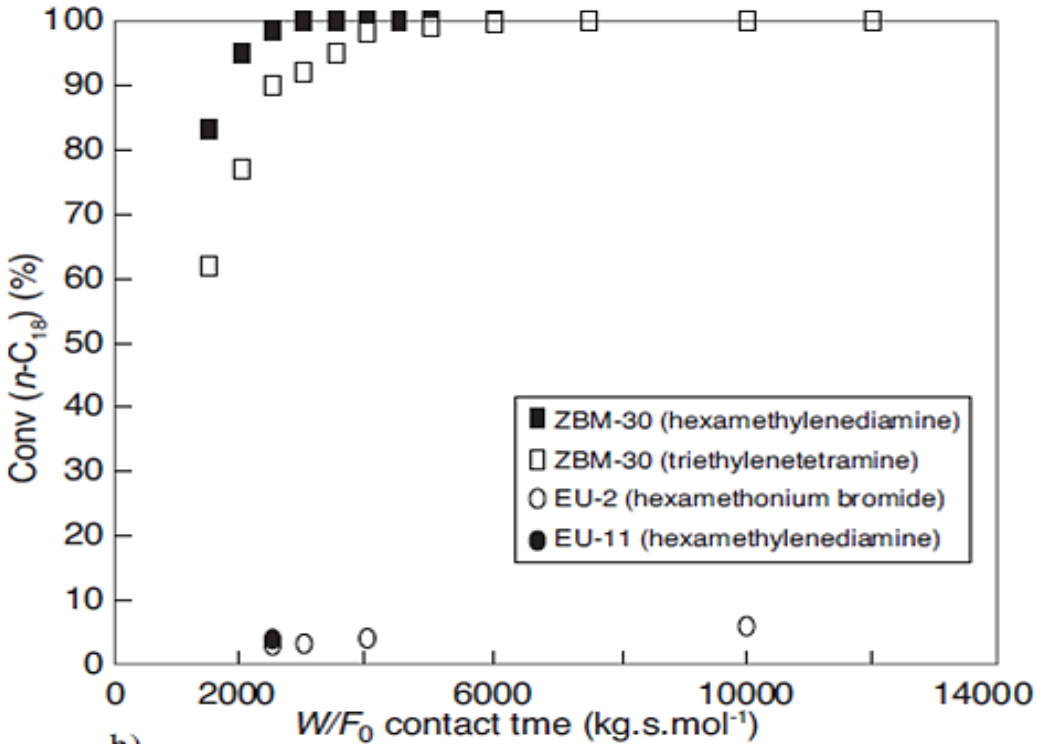

Figure 1.9. Conversion of C_{18} over zeolites ZBM-30, EU-2 and EU-11 catalysts at 233 ^{o}C [54].

It is evident from figure 1.9 that ZBM-30 (SAR = 108) prepared using HMDA exhibited highest activity compared to EU-2 (SAR = 216) and EU-11 (SAR = 84). The activity of ZBM-30 prepared using HMDA increased with contact time up to 4000 kg.s.mol^{-1}, after which it remained constant and equal to that of ZBM-30 prepared using TETA. The authors also showed that there was no obvious relationship between catalytic activity and SAR of the supports [54]. The catalytic performance of ZBM-30 based catalysts in cracking and isomerisation reactions of *n*-C_{18} is illustrated in figure 1.10.

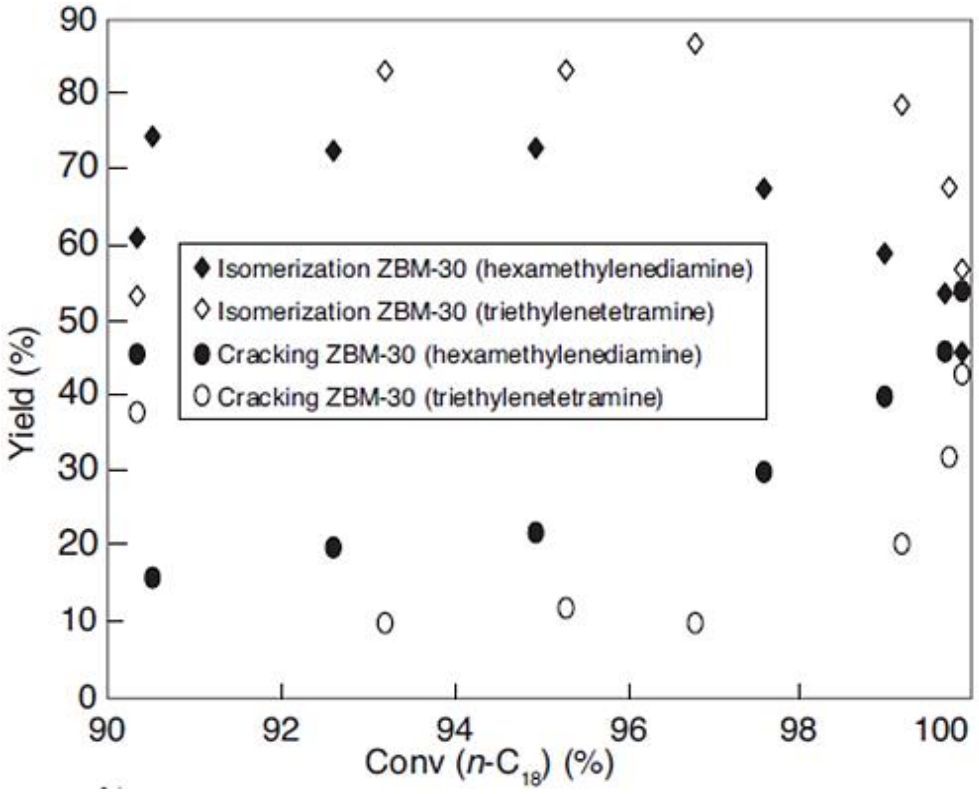

Figure 1.10. Product yield as a function of C_{18} conversion for ZBM-30 catalyst [54].

The figure shows that the yield of cracking products increased with increasing conversion for both ZBM-30 (obtained using HMDA and TETA as SDAs) catalysts and ZBM-30 (obtained using HMDA as SDA) catalyst was more selective to cracking products. Worth noting is that the selectivity to isomerised products yield decreased with an increase in conversion for both catalysts, and interestingly ZBM-30 (obtained using HMDA as SDA) catalyst was less selective to isomerised products than the other ZBM-30-based catalyst [54]. These results show that ZBM-30 (obtained using HMDA) is a good hydrocracking catalyst.

The ZBM-30 (SAR = 90) based catalyst was combined with poorly-crystallised Y zeolite (SAR = 36.4), and compared with the catalyst based only on poorly-crystallised Y zeolite during the hydrocracking of vacuum gas oil (VGO) (properties: sulphur = 15 ppm and nitrogen = 5 ppm) to middle distillates (C_{10} - C_{20}) [47]. The performance of these catalysts was studied at reaction temperatures in the range 380 - 420 ^{o}C. The conversion was 80 %, with middle distillate selectivity of 68 % for the combined ZBM-30/Y zeolite catalyst, and Y zeolite achieved 65 % middle distillate selectivity [47].

1.5.4 ZSM-23

Zeolite ZSM-23 is a high-silica zeolite, possessing non-interconnected 1-dimensional, 10-member ring channels as well as tear-drop-shaped pores with diameters of 0.52 nm x 0.45 nm (figure 1.11) [9, 59, 64]. Its 10-member ring channels can be described as having small pore extensions or side pockets [59].

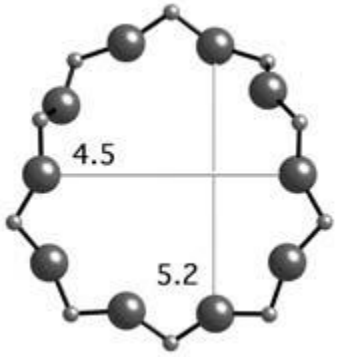

Figure 1.11. The dimensions of ZSM-23 viewed along [001] plane [9].

As shown in figure 1.11, the dimensions of ZSM-23 suggest that the cavities of this zeolite can accommodate a sphere or a molecule with a diameter less than 0.5 nm [10, 59]. The first zeolite ZSM-23 synthesis recipe using pyrrolidine as SDA was patented in the late 1970s by Plank *et al.* [65]. The synthesis was carried out at 180 ^{o}C for 7 days [65]. Zeolite ZSM-23 can also be synthesised using various SDAs such as diisopropanolamine, isopropylamine, diquat-7, diquat-8 and diquat-12 [66].

Varieties of industrially-relevant reactions, such as isomerisation, cracking alkylation, *etc.*, are catalysed by ZSM-23. It has a high catalytic activity and selectivity in the isomerisation of *n*-butane, because of its unique pore structure and strong surface acidity. Also, this zeolite shows high activity in the cracking of *n*-butene to ethene and propylene [67].

In the hydrocracking of long *n*-alkanes such as *n*-dodecane, Pt/ZSM-23 showed higher catalytic activity than Pt/ZSM-22 and Pt/ZSM-22/ZSM-23 catalysts [68]. Amongst the three catalysts, Pt/ZSM-23 was selective to hydrocracking, achieving the highest cracking yield of above 35 % at a reaction temperature of 320 ^{o}C,

compared to 27.5 % and 17.5 % cracking yields of Pt/ZSM-22 and Pt/ZSM-22/ZSM/23, respectively. Secondary cracking reactions could not be avoided on the Pt/ZSM-23, since more of propane and butane were detected in cracking products [68]. The Pt/ZSM-22 and Pt/ZSM-22/ZSM-23 catalysts favoured isomerisation and showed minimal secondary cracking.

1.6 Applications of zeolites: The hydrocracking process

1.6.1 The hydrocracking process

Hydrocracking is a refinery process for producing light fuels from petroleum feeds by catalytic cracking in the presence of hydrogen [69]. The hydrocracking technology was developed in Germany in the period between 1915 and 1945 [70]. The first commercial hydrocracking process, which was named the Bergius, went on stream in 1927 in Germany [70]. It was then established in the late 1950s after more catalysts were developed for this process by Chevron and Union Oil [71].

The hydrocracking mechanism shown in figure 1.12 is currently the most accepted mechanism [54, 72].

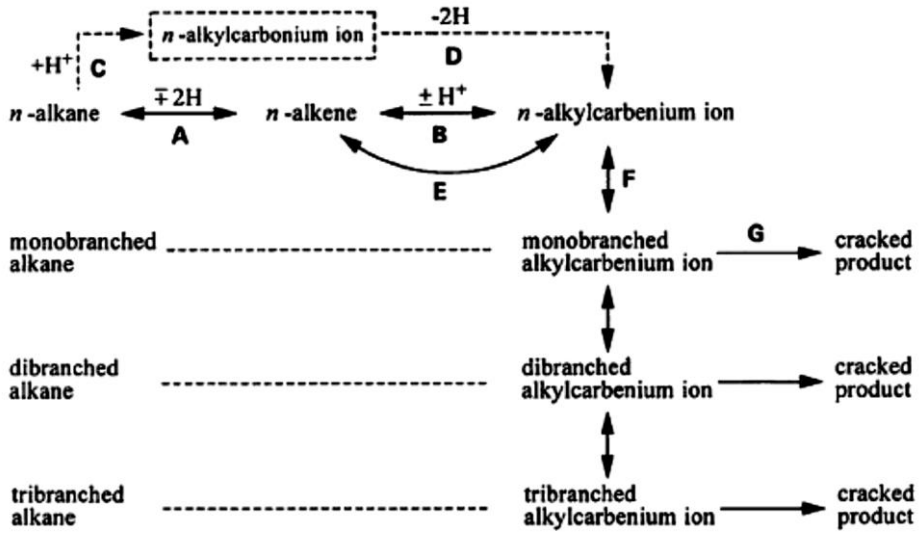

Figure 1.12. Classical hydrocracking mechanism [72].

The steps labelled in the figure above are described below.

A : Hydrogenation-dehydrogenation on metallic sites.

B : Protonation-deprotonation on acid sites.

C : Addition of proton to form alkylcarbonium ion on acid sites.

D : Dehydrogenation to form alkylcarbenium ion.

E : Competitive adsorption-desorption of alkene and carbenium ion on acid sites.

F : Rearrangement of alkylcarbenium ion.

G : Cracking of alkylcarbenium ion.

According to the hydrocracking mechanism, paraffins hydrogenate (A) on the metal sites of the catalyst and the corresponding olefins diffuse to the Brønsted acid sites, where they are protonated (B and C) to produce alkylcarbenium ions. The alkylcarbenium ions undergo skeletal rearrangement (F) and β-scission (G), to produce branched and cracked products, respectively. The branched and cracked products diffuse to the metal sites of the catalyst, where they are hydrogenated to the corresponding paraffins, which then desorb from the catalyst [54, 72].

According to the β-scission mechanism, multi-branched products are more susceptible to cracking than mono-branched products [54]. An ideal hydrocracking process selectively converts the heavy hydrocarbons into middle distillates, and simultaneously minimise cracking (retards secondary cracking) of the middle distillates already present in the feedstock to lighter undesired hydrocarbons (*e.g.,* naphtha) [54].

1.6.2 Hydrocracking catalysts

The most used and successful hydrocracking catalyst in the early days was pelleted tungsten sulphide [70, 71]. This catalyst is tolerant to high concentrations of impurities such as nitrogen, sulphur and oxygen in the feed. However,

disadvantage of using this catalyst is the production of low-octane gasoline, because of its high hydrogenation power [70]. The other hydrocracking catalysts were iron or nickel supported on fluorinated montmorillonite and nickel supported on amorphous silica-alumina (ASA) [70]. The catalysts used in hydrocracking are generally bifunctional, consisting of a hydrogenation function supplied by the metal and a cracking function provided by an acidic support. The metals can be noble metals (platinum, palladium) or non-noble metal sulphides (cobalt, nickel, molybdenum, tungsten) and the acidic support can be ASA or zeolite [54, 70, 71, 72].

Nobel metals are used when the concentration of sulphur in the feedstock is low, because they are not tolerant to higher concentration of sulphur [54]. Palladium-promoted catalysts are generally more active than the transition metal sulphides and the products are also very well hydrogenated [73]. Palladium is more tolerant to carbon monoxide (CO) poisoning than platinum, with the latter deactivating upon exposure to CO [74].

The following are the requirements to be met for a catalyst to be considered as an ideal hydrocracking catalyst, when using *n*-hexadecane (*n*-C_{16}) as a test molecule [54, 72] :

(i) There should be a flat molar product distribution between C_4 and C_{12} centred around C_8,

(ii) Virtually no C_1, C_2, C_{14} or C_{15} forming,

(iii) The C_3 and C_4 should be formed at half molar amounts of the product distribution.

Figure 1.13 shows a typical product distribution of cracked products for the hydrocracking of *n*-C_{16} over an ideal-hydrocracking catalyst.

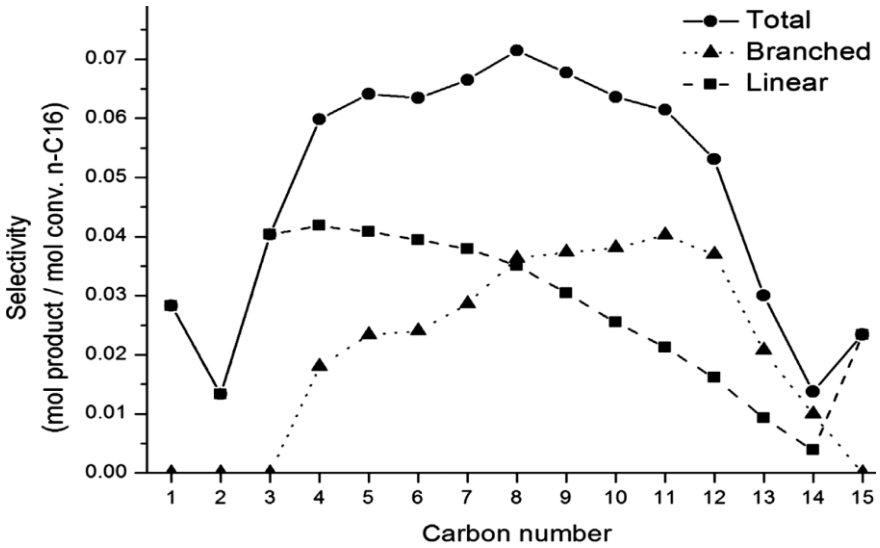

Figure 1.13. The molar distribution of cracked products during the hydrocracking of *n*-C_{16} over Pt/ASA [72].

The cracking product distribution obtained over Pt/ASA catalyst shows that all the requirements of an ideal-hydrocracking catalyst were met (figure 1.13).

In order to fulfil the requirements of the ideal hydrocracking catalyst, the metal function and the acidic function must be a short mutual distance apart to maintain balance. The hydrogenation function should be strong enough and the acidity should be weak or medium [54].

1.6.3 Hydrocracking feedstocks

Different feedstocks are used in the hydrocracking process. Crude oil is traditionally used, whereas the most commonly used is VGO with a typical 350-600 ^{o}C boiling range [75]. However, VGO feedstock consists of various impurities (naphthenic, aromatic species, sulphur, nitrogen, metals, *etc.*) and leads to hydrocracking products containing these impurities [76, 77]. Noble metals are not applied in the hydrocracking of VGO, but transition metal sulphides are applied instead, because transition metal sulphides are resistant to poisoning by the high level of impurities present in VGO (*e.g.,* sulphur) [75 - 77]. The sulphur present in the diesel fuels derived from VGO contributes to air pollution, and it was also found that the amount of sulphur oxide (SOx) emissions and total particulate emissions are proportional to the amount of sulphur contained in the diesel fuel

[77]. Diesel derived from VGO has a cetane number of around 55 which is low compared to the diesel derived from LTFT wax (cetane number 70) [78]. Because of the disadvantages of using VGO as a feedstock to produce diesel, there is a need for an alternative feedstock to produce ultra-low sulphur diesel (ULSD) fuel. The LTFT wax has advantages over crude oil because it contains about 5 ppm of sulphur and about 1 wt. % of aromatics [54, 78]. This makes LTFT wax a potential feedstock for the production ULSD fuel.

1.6.4 Low-temperature Fischer-Tropsch wax as hydrocracking feedstock

Fischer-Tropsch synthesis is the catalytic conversion of syngas ($CO + H_2$) into liquid valuable fuels [79]. It is commercially performed either in low or high temperature conditions. High temperature Fischer-Tropsch synthesis uses an iron-based catalyst at reaction temperatures above 320 ^{o}C and a pressure of 20 bar, and is used for the production of gasoline and linear low molecular mass olefins. On the other hand, LTFT synthesis uses a cobalt-based catalyst at reaction temperatures below 250 ^{o}C (also pressure of 20 bar), and it is used for the production of high molecular weight hydrocarbons, mostly waxes, which can be sold as such or can be hydrocracked to high-quality diesel [79]. Theoretically, the hydrocracking of LTFT wax produces around 80 % of middle distillates, which is twice the maximum middle distillates yield obtained through a Fischer-Tropsch unit alone [54]. De Haan *et al.* [80] studied the hydrocracking of LTFT wax over sulphided and non-sulphided nickel catalysts supported on ASA. It was demonstrated that both catalysts yielded comparable diesel selectivities of 73 - 77 % at conversions of around 52 %, showing that the catalysts were highly selective to diesel but less active [80]. The use of the catalysts containing platinum metal supported on ASA, and a combination of platinum and tungsten supported on ASA, in the hydrocracking of LTFT wax was investigated by Leckel [81]. It was found that the metal dispersion, the support pore structure and acidity had an influence on the activity and selectivity. The larger mesopores were found to be detrimental to the formation of diesel at higher conversions [81]. The importance of acidity in the hydrocracking of LTFT wax was also highlighted by Lee *et al*. [82]. They showed that the conversion increased with increasing acidity [82]. In general,

research shows that regardless of the metal used, the ASA-based catalysts are selective to middle distillates but with low activity [80 - 82].

Zeolites are more active compared to ASA in the cracking of Fischer-Tropsch wax [83]. One of the difficulties associated with the use of alumina supports is the control of acidity, which leads to undesired cracked products and reduction of catalyst life [83]. The superiority of zeolite-based catalysts to their alumina-based counterparts was demonstrated by Nishijima *et al.* [84]. Their findings are depicted in figure 1.14.

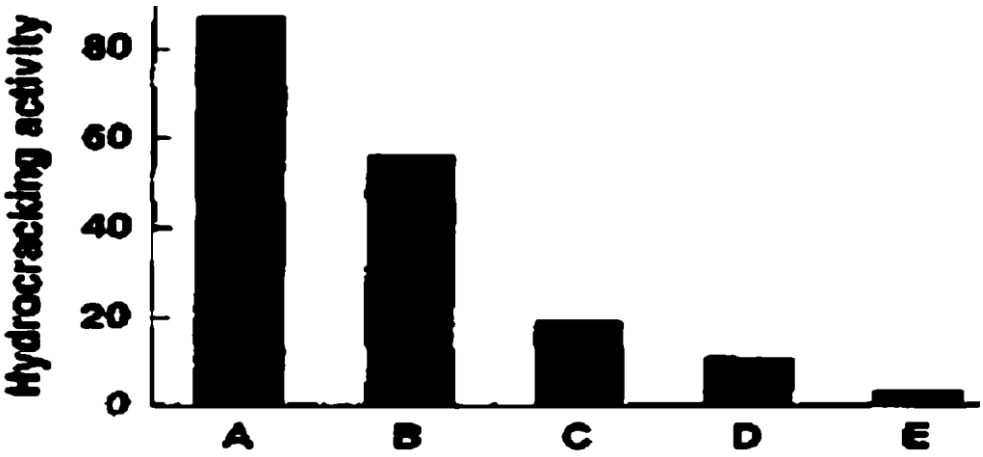

Figure 1.14. A comparison of hydrocracking activity of molybdenum sulfide catalysts based on different supports : (A) USY, (B) Mordenite, (C) ZSM-5, (D) ASA, (E) Alumina [82].

As shown in figure 1.14, USY-based catalyst achieved the highest hydrocracking activity > 80 % and the lowest hydrocracking activity < 10 % was obtained using alumina-based catalyst. The order of hydrocracking activity of the catalysts based on different supports was as follows: USY > Mordenite > ZSM-5 > ASA > alumina [85]. This study also indicated that proper control of external surface and crystal size of the zeolite is very important in hydrocracking, thus implying that hydrocracking catalysts are sensitive to their preparation and pretreatment conditions. Using the acidity criterion, Ali *et al.* [85] showed that the catalyst based on zeolite β was more active than those based on USY and ASA. This was generally attributed to more Brønsted acid sites on zeolite β than on ASA and USY zeolite [85]. Furthermore, Park [86] tested Pt supported on zeolites ZSM-5, ZSM-

22, SAPO-11, Al-MCM-41, H-Y and H-β for the hydrocracking and hydroisomerisation of *n*-C_{16}. The zeolites ZSM-5, H-β and ZSM-22 have stronger acid sites than zeolites Pt/H-Y, Pt/SAPO-11 and Pt/Al-MCM-41. Acidity and metal dispersion were the major factors that influenced selectivities and activities of the different catalysts used [86]. The results of this study are summarised in table 1.4

The table below shows the selectivity obtained using Pt/ZSM-5, Pt/ZSM-22, Pt/SAPO-11, Pt/Al-MCM-41, Pt/H-Y and Pt/H-Beta catalysts.

Table 1.4 : Activity and selectivity of zeolite-based catalysts for the hydrocracking and hydroisomerisation of *n*-C_{16} [86].

Catalyst	Metal dispersion (%)	Conversion (%)	*i*-C_{16} selectivity (wt.%)	Hydrocracking selectivity (wt.%)
Pt/ZSM-5	59	37.1	15.6	84.4
Pt/ZSM-22	41	41.3	31.2	68.8
Pt/SAPO-11	35	44.0	66.6	33.4
Pt/Al-MCM-41	55	44.7	88.9	11.1
Pt/H-Y	45	39.2	75.7	24.3
Pt/H-β	37	42.5	50.7	49.3

The catalysts based on ZSM-5, ZSM-22 and zeolite β were highly selective to hydrocracking, with hydrocracking selectivities of 84.4 %, 68.8 % and 49.3 %, respectively. This high hydrocracking selectivity was attributed to the strong acidity of the catalysts. The catalyst based on Al-MCM-41, H-Y, SAPO-11 zeolites were highly selective to isomerisation because of their moderate acid strength [86]. To this end, most zeolites used for the hydrocracking of LTFT wax are large-pore zeolites [81 - 86]. Since the LTFT wax feed has no bulky molecule, zeolite crystals with fully intact narrow pore structure may also be applied [87]. In the case of large-pore zeolites, the alkene physisorption occurs both in the pores and on the pore mouths, unlike in medium-pore zeolites, where physisorption occurs on the

pore mouths [83]. The dimensions of the pores affect activity and selectivity of the catalysts during the hydrocracking of heavy hydrocarbons to lighter hydrocarbons. Wider pores favour multi-branching of products, while constrained pores favour mono-branching of products [54].

1.7 Purpose of the study

1.7.1 Aim

The aim of this study is to explore a series of 10-member ring zeolites as possible supports for Pd catalysts in the hydrocracking of *n*-C_{16}.

1.7.2 Objectives

The objectives of this study are to:

i. synthesise zeolites ZSM-22, ZSM-48, ZBM-30 and ZSM-23 to different SARs,

ii. characterise the resulting zeolites using physicochemical techniques such as XRD, BET, and SEM in order to understand their properties,

iii. load palladium on the acid form of each zeolite using incipient wetness impregnation method,

iv. evaluate the activity of the Pd/zeolite catalysts in the hydrocracking of *n*-C_{16}.

1.8 Scope of the research

Use of petroleum as a feedstock for the production of diesel fuels raises environmental concerns, because of the emissions (*e.g.,* SOx, NOx, aromatics, *etc.*) associated with it. There is therefore a high demand of ULSD fuels. The hydrocracking process is often used for the production of diesel fuels. The LTFT wax can be hydrocracked to ULSD fuels using appropriate bifunctional catalysts. Much research effort is dedicated to the development of zeolite-based

hydrocracking catalysts. The main aim of the work presented in this dissertation is to contribute to this development.

Chapter 1 gives the rationale for carrying out this study and also include the literature review. The synthesis of zeolites ZSM-22, ZSM-48, ZBM-30 and ZSM-23 were attempted and the modified procedures followed are presented in Chapter 2. Also presented in Chapter 2 are the physicochemical techniques used to investigate the properties of the synthesised zeolites and the analysis thereof. The *n*-C_{16} molecule was chosen as model waxy feedstock. The hydrocracking of *n*-C_{16} was studied over ZSM-22-based and ZSM-23-based catalysts. Chapter 3 presents the details of the reaction conditions used and the analysis of the hydrocracking results obtained. Lastly the conclusions and recommendations are presented in Chapter 4.

1.9 References

[1] A.F. Cronstedt, Ron och beskriting om en obekant bärg ant, som kallas zeolites, Akademeins Handlingar Stockholm, volume 18, 1756, pages 120-130.

[2] M. M. Helmkamp, M. E. Davis, Synthesis of porous silicates, Annual Review of Materials Science, volume 25, 1995, pages 161-92.

[3] L. B. McCusker, C. Baerlocher, Chapter 3 Zeolite structures, Studies in Surface Science and Catalysis, volume 137, 2001, pages 37-67.

[4] W. Lowenstein, The distribution of aluminium in the tetrahedra of silicates and aluminates, American Mineralogist, volume 39, 1954, pages 92-96.

[5] J. Weitkamp, Zeolite and catalysis, Solid State Ionics, volume 131, 2000, pages 175-188.

[6] C. Baerlocher, L. B. McCusker, D. H. Olson, Structure Commission of the International Zeolite Association, 4 July 2013.

[7] G. Gottardi, E. Galli, Natural zeolites, Minerals and Rocks, volume 18, 1985, pages 1-34.

[8] R. Xu, W. Pang, J. Yu, Q. Huo, M. Chen, Chemistry of zeolites and related porous materials : Synthesis and structure, John Wiley and Sons, 2007.

[9] C. Baerlocher, L. B. McCusker, D. H. Olson, Atlas of zeolite framework types, Elsevier, Sixth revised edition, 2007.

[10] J. C. Vedrine, Isomorphous substitution in zeolitic frameworks procedures and characterization, Studies in Surface Science and Catalysis, volume 69, 1991, pages 25-42.

[11] M. H. de St. Claire-Deville, Reproduction of levyne, Comptes Rendus, volume 54, 1862, pages 324-328.

[12] R. M. Barrer, Syntheses and reactions of mordenite, Journal of the Chemical Society, Issue 0, 1948, pages 2158-2163.

[13] R. M. Milton, Molecular sieve science and technology: A historical perspective, Zeolite Synthesis, volume 398, 1989, pages 1-10.

[14] G. T. Kerr, G. T. Kokotailo, Sodium zeolite ZK-4, a new synthetic crystalline aluminosilicate, Journal of the American Chemical Society, volume 83, 1961, page 4675.

[15] R. L. Wadlinger, G. T. Kerr, E. J. Rosinski, Catalytic composition of a crystalline zeolite, United States Patent 3308069, 1967.

[16] R. J. Argauer, G. R. Landolt, Crystalline zeolite ZSM-5 and method of preparing the same, United States Patent 3702886, 1972.

[17] R. P. Gunawardene, H. Gies, B. Marler, Long-chain polyamine and amine boric acid as templates for the synthesis of porous tectosilicates, Zeolites, volume 8, 1988, pages 127-131.

[18] D. Georgiev, B. Bogdanov, K. Angelova, I. Markovska, Y. Hristov, Synthetic zeolites - structure, clasification, current trends in zeolite synthesis: review, International Science conference, Stara Zagora, Bulgaria, 4th-5th June 2009.

[19] C. S. Cundy, P. A. Cox, The hydrothermal synthesis of zeolites : History and development from the earliest days to the present time, Chemical Reviews, volume 103, 2003, pages 663-701.

[20] J. C. Jansen, Chapter 5A The preparation of oxide molecular sieves A. Synthesis of zeolites, Studies in Surface Science and Catalysis, volume 137, 2001, pages 175-227.

[21] C. Martinez, A. Corma, Inorganic molecular sieves: Preparation, modification and industrial application in catalytic processes, Coordination Chemistry Reviews, volume 255, 2011, pages 1558-1580.

[22] X. Bin, Structure-performance relationships in solid-acid aluminosilicates, PhD thesis, University of York, The United Kingdom, 2007.

[23] G. Busca, Acid catalysts in hydrocarbon chemistry, Chemical Reviews, volume 107, 2007, pages 5366-5410.

[24] C. L. Thomas, Chemistry of cracking catalysts, Industrial and Engineering Chemistry, volume 41, 1949, pages 2564-2573.

[25] S. R. Mistry, K. C. Maheria, Synthesis of diarylpyrimidinones (DAPMs) using large pore zeolites, Journal of Molecular Catalysis A : Chemical, volume 355, 2012, pages 210-215

[26] J. P. Marques, I. Gener, P. Ayrault, J. C. Bordado, J. M. Lopes, F. R. Ribeiro, M. Guisnet, Infrared Spectroscopic study of the acid properties of dealuminated BEA zeolites, Microporous and Mesoporous Materials, volume 60, 2003, pages 251-262.

[27] E. Dempsey, Acid strength and aluminum site reactivity of Y zeolites, Journal of Catalysis, volume 33, 1974, 497-499.

[28] E. Dempsey, A tentative model of Y zeolites to explain their acid behavior, Journal of Catalysis, volume 39, 1975, pages 155-157

[29] A. Chatterjee, T. Iwasaki, T. Ebina, H. Tsuruya, T. Kanougi, Y. Oumi, M. Kubo, A Miyamoto, Effects of structural characteristics of zeolites on the properties of their bridging and terminal hydroxyl groups, Applied Surface Science, volumes 130-132, 1998, pages 555-560.

[30] M. G. Clerici, Zeolites for fine chemicals production, Topics in Catalysis, volume 13, 2000, pages 373-386.

[31] G. E. Giannetto, G. R. Perot, M. R. Guisnet, Hydroisomerization and hydrocracking of n-alkanes. 1. Ideal hydroisomerization PtHY catalysts, Industrial & Engineering Chemistry : Product Research and Development, volume 25, 1986, pages 481-490.

[32] B. Wang, Zeolite deactivation during hydrocarbon reactions : Characterisation of coke precursors and acidity, product distribution, PhD thesis, University College London, The United Kingdom, 2007.

[33] A. G. Ashton, S. Batmanian, D. M. Clark, J. Dwyer, F. R. Fitch, A. Hinchcliffe, F.J. Machado, Acidity in zeolites, Studies in Surface Science and Catalysis, volume 20, 1985, pages 101-109.

[34] C. I. Round, S. J. Hill, K. Latham, C. D. Williams, The crystal morphology of zeolite A. The effects of the source of the reagents, Microporous Materials, volume 11, 1997, pages 213-225.

[35] T. O. Drews, M. Tsapatsis, Progress in manipulating zeolite morphology and related applications, Current Opinion in Colloid and Interface Science, volume 10, 2005, pages 233-238.

[36] F. Ocampo, J. A. Cunha, M. R. de Lima Santos, J. P. Tessonnier, M. M. Pereira, B. Louis, Synthesis of zeolite crystals with unusual morphology: Application in acid catalysis, Applied Catalysis A : General, volume 390, 2010, pages 102-109.

[37] M. Kustova, K. Egeblad, K. Zhu, C. H. Christensen, Versatile route to zeolite single crystals with controlled mesoporosity : In situ sugar decomposition for templating of hierarchical zeolites, Chemistry of Materials, volume 19, 2007, pages 2915-2917.

[38] A. Dabrowski, Adsorption - from theory to practice, Advances in Colloid and Interface Science, volume 93, 2001, pages 135-224.

[39] S. J. Gregg, K. S. W. Sing, Adsorption surface area and porosity, Second edition, Academic press, Second Edition, 1982.

[40] Z. Liu, M. F. Ottaviani, L. Abrams, X. Lei, N. J. Turro, Characterization of the external surface of silicalites employing electron paramagnetic resonance, Journal of Physical Chemistry A, volume 108, 2004, pages 8040-8047.

[41] A. Sayari, E. Crusson, S. Kaliaguine, External surface areas of H-ZSM-5 zeolites, Langmuir, volume 7, 1991, pages 314-317.

[42] E. G. Fuentes-Ordonez, J. A. Salbidegoitia, J. L. Ayastuy, M. A. Gutiérrez-Ortiz, M .P. Gonzalez-Marcos, J. R. Gonzalez-Velasco, High external surface Pt/zeolite catalysts for improving polystyrene hydrocracking, Catalysis Today, volume 227 2014, 163-170.

[43] P. B. Weisz, V. J. Frilette, Intracrystalline and molecular shape-selective catalysis by zeolite salts, The Journal of Physical Chemistry, volume 64, 1960, page 382.

[44] S. M. Csicsery, Catalysis by shape selective zeolites-science and technology, Pure and Applied Chemistry, volume 58, 1986, pages 841-856.

[45] Y. Sugi, Shape-selective alkylation of biphenyl catalyzed by H-mordenites, Korean Journal of Chemical Engineering, volume 17, 2000, pages 1-11.

[46] J. L. Schlenker, W. J. Rohrbaugh, P. Chu, E. W. Valyocsik, G. T. Kokotailo, The framework topology of ZSM-48 : A high silica zeolite, Zeolites, volume 5, 1985, pages 355-358.

[47] E. Benazzi, E. Guillon, J. Martens, Catalyst and its use for improving the pour point of hydrocarbon charges, United States Patent 7282465 B2, 2007.

[48] F. G. Dwyer, Highly siliceous porous crystalline material ZSM-22 and its use in catalytic dewaxing of petroleum stocks, United States Patent 4556477, 1985.

[49] T. Demuth, X. Rozanska, L. Benco, J. Hafner, R. A. van Santen, H. Toulhoat, Catalytic isomerization of 2-pentene in H-ZSM-22 - A DFT investigation, Journal of Catalysis, volume 214, 2003, pages 68-77.

[50] R. Zhang, Y. Wang, W. Wu, Dynamic and static synthesis of ZSM-22 zeolite and its characterization, International Conference on Solid State and Materials, volume 22, 2012, pages 54-59.

[51] D. Masih, T. Kobayashi, T. Baba, Hydrothermal synthesis of pure ZSM-22 under mild conditions, Chemical Communications, Issue 31, 2007, pages 3303-3305.

[52] N. Kumar, L. E. Lindfors, R. Byggningsbacka, Synthesis and characterization of H-ZSM-22, Zn-H-ZSM-22 and Ga-H-ZSM-22 zeolite catalysts and their catalytic activity in the aromatization of n-butane, Applied Catalysis A : General, volume 139, 1996, pages 189-199.

[53] C. S. L. Narasimhan, J. W. Thybaut, G. B. Marin, P. A. Jacobs, J. A. Martens, J. F. Denayer, G. V. Baron, Kinetic modeling of pore mouth catalysis in the hydroconversion of n-octane on Pt-H-ZSM-22, Journal of Catalysis, volume 220, 2003, pages 399-413.

[54] C. Bouchy, G. Hastoy, E. Guillon, J.A. Martens, Fischer-Tropsch waxes upgrading via hydrocracking and selective hydroisomerization, Oil Gas Science and Technology- Rev. IFP., volume 64, 2009, pages 91-112.

[55] P. Chu, Silico-crystal method of preparing same and catalytic conversion therewith, United States Patent 4397827, 1981.

[56] C. D. Chang, C. T. W. Chu, P. D. Perkins, Olefins from methanol and/or dimethyl ether, United States Patent 4476338, 1984.

[57] K. Suzuki, Y. Kiyozumi, S. Shin, K. Fujisawa, H. Watanabe, K. Saito, K. Noguchi, Zeolite Synthesis in the System Pyrrolidine-Na_2O-Al_2O_3-SiO_2-H_2O, Zeolites, volume 6, 1986, pages 290-298.

[58] G. Zhao, J. Teng, Y. Zhang, Z. Xie, Y. Yue, Q. Chen, Y. Tang, Synthesis of ZSM-48 zeolites and their catalytic performance in C4-olefin cracking reactions, Applied Catalysis A: General, volume 299, 2006, pages 167-174.

[59] S. Teketel, W. Skistad, S. Benard, U. Olsbye, K. P. Lillerud, P. Beato, S. Svelle, Shape selectivity in the conversion of methanol to hydrocarbons: The catalytic performance of one-dimensional 10-ring zeolites: ZSM-22, ZSM-23, ZSM-48 and EU-1, ACS Catalysis, volume 2, 2012, pages 26-37.

[60] R. F. Lobo, H. van Koningsveld, New description of the disorder in zeolite ZSM-48, Journal of the American Chemical Society, volume 124, 2002, pages 13222-13230.

[61] W. B. Genetti, A. R. Bishop, N. M. Page, G. J. Howsmon, L. L. Ansell, J. W. Johnson, Production of fuels and lube oils from Fischer-Tropsch wax, European Patent 1563036 B1, 2011.

[62] P. Caullet, S. Lacombe, J. Paillaud, N. Bais, L. Rouleau, Process for preparation of ZBM-30-type zeolites using a diammonium ether-type

compound as an organic structuring agent, United States Patent 7622099 B2, 2009.

[63] G. Hastoy, E. Guillon, J. Martens, Method for synthesizing ZBM-30 zeolite from a mixture of amine compounds, United States Patent 7544347 B2, 2009.

[64] W. Huybrechts, G. Vanbutsele, K. J. Houthoofd, F. Bertinchamps, C. S. L. Narasimhan, E. M. Gaigneaux, J. W. Thybaut, G. B. Marin, J. F. M. Denayer, G. V. Baron, P. A. Jacobs, J. A. Martens, Skeletal isomerization of octadecane on bifunctional ZSM-23 zeolite catalyst, Catalysis Letters, volume 100, 2005, pages 235-242.

[65] C. J. Plank, E. J. Rosinski, M. K. Rubin, B. Cynwyd, Crystalline zeolite ZSM-23 and synthesis thereof, United States Patent 4076842, 1978.

[66] L. Ye, W. Zhendong, L. Yun, L. I. Xianbo, L. Yueming, W. U. Peng, Synthesis of ZSM-23 zeolite using isopropylamine as template, Chinese Journal of Catalysis, volume 30, 2009, pages 525-530.

[67] B. Marler, C. Deroche, H. Gies, C. A. Fyfe, H. Grondey, G. T. Kokotailo, Y. Feng, S. Ernst, J. Weitkamp, D. E. Cox, The structure of zeolite ZSM-23 (MTT) refined from synchrotron x-ray powder data, Journal of Applied Crystallography, volume 26, 1993, pages 636-644.

[68] C. Kebin, Z. Zhen, T. Zhijian, H. Sheng, Y. Lijun, L. Tianshu, W. Bingchun, M. Xiangbin, G. Shanbin, T. Mingwei, L. Yanfeng, Hydroisomerization performance of platinum supported on ZSM-22/ZSM-23 intergrowth zeolite catalyst, Petroleum Science, volume 10, 2013, pages 242-250.

[69] S. Cheng, Y. Yang, K. Zhang, J. Wang, Zeolite beta made from mesoporous materials and its hydrocracking performance, Catalysis Today, volume 116, 2006, pages 2-5.

[70] J. Scherzer, A. J. Gruia, Hydrocracking Science and Technology, New York, 1996.

[71] L. F. Hatch, A chemical view of refining, Hydrocarbon Process, volume 48, 1969, pages 77-88.

[72] H. Deldari, Suitable catalysts for hydroisomerization of long-chain normal paraffins, Review, Applied Catalysis A: General, volume 293, 2005, pages 1-10.

[73] P. Treccani, Refining and petrochemicals, Encyclopaedia of Hydrocarbons, volume 2, 2008, pages 273-297.

[74] R. Brosius, J. C. Q. Fletcher, Hydrocracking under Fischer–Tropsch conditions; the effect of CO on the mass transfer resistance by metal clusters, Journal of Catalysis, volume 317, 2014, pages 318-325.

[75] M. A. Ali, T. Tatsumi, T. Masuda, Development of heavy oil hydrocracking catalysts using amorphous silica-alumina and zeolites as catalyst supports, Applied Catalysis A: General, volume 233, 2002, pages 77-90.

[76] K. H. Algelt, M. M. Boduszynski, Composition and analysis of heavy petroleum fractions, Sixth edition, New York, 1994.

[77] S. K. Oh, D. S. Baik, Y. C. Han, Emission characteristics in ultra-low sulfur diesel, International Journal of Automotive Technology, volume 4, 2003, pages 95-100.

[78] D. Leckel, Upgrading of Fischer-Tropsch products to produce diesel, Haldor Topsoe Catalysis Forum, Munkerupgaard, 19 - 20 August 2010.

[79] M. E. Dry, The Fischer–Tropsch process: 1950 - 2000, Catalysis Today, volume 71, 2002, pages 227-241.

[80] R. de Haan, G. Joorst, E. Mokoena, C. P. Nicolaides, Non-sulfided nickel supported on silicated alumina as catalyst for the hydrocracking of n-hexadecane and of iron-based Fischer-Tropsch wax, Applied Catalysis A: General, volume 327, 2007, pages 247-254.

[81] D. Leckel, Noble metal wax hydrocracking catalysts supported on high-siliceous alumina, Industrial &. Engineering Chemistry Research, volume 46, 2007, pages 3505-3512.

[82] J. Lee, S. Hwang, J. G. Seo, U. G. Hong, J. C. Jung, I. K. Song, Pd catalyst supported on SiO_2-Al_2O_3 xerogel for hydrocracking of paraffin wax to middle distillate, Journal of Industrial and Engineering Chemistry, volume 17, 2011, pages 310-315.

[83] K. S. Triantafyllidis, V. G. Komvokis, M. C. Papapetrou, I. A. Vasalos, A. A. Lappas, Microporous and mesoporous aluminosilicates as catalysts for the cracking of Fischer-Tropsch waxes towards the production of “clean” bio-fuels, From Zeolites to Porous MOF Materials - the 40th Anniversary of International Zeolite Conference, 2007, pages 1344-1350.

[84] A. Nishijima, T. Kameoka, T. Sato, H. Shimada, Y. Nishimura, Y. Yoshimura, N. Matsubayashi, M. Imamura, Catalyst design and development for upgrading hydrocarbon fuels, Catalysis Today, volume 29, 1996, pages 179-184.

[85] M. A. Ali, T. Tatsumi, T. Masuda, Development of heavy oil hydrocracking catalysts using amorphous silica-alumina and zeolites as catalyst supports, Applied Catalysis A: General, volume 233, 2002, pages 77-90.

[86] K. Park, S. Ihm, Comparison of Pt/zeolite catalysts for n-hexadecane hydroisomerisation, Applied Catalysis A : General, volume 203, 2000, pages 201-209.

[87] R. S. Kukard, The effect of zeolite type on the hydrocracking of long n-paraffins, MSc thesis, University of Cape Town, South Africa, 2008.

CHAPTER 2
Synthesis and characterisation of zeolites

2.1 Introduction

This chapter presents the general description of reagents, equipment and the procedures for synthesising zeolites ZSM-22, ZSM-48, ZBM-30 and ZSM-23. After every synthesis, the resulting zeolites were characterised with X-ray diffraction (XRD), scanning electron microscopy (SEM) and Brunauer-Emmett-Teller (BET) surface area analysis. Whenever the attempted synthesis was not successful, the procedure was either modified or another procedure was used instead. The modifications differed for each zeolite synthesis and are briefly explained in the experimental (zeolite synthesis) section of this chapter. The ZSM-22 and ZSM-23 zeolites were the only zeolites amongst the four to be synthesised to three levels of silica-to-alumina ratios (SARs), *viz.,* 60, 80 and 120. The SARs reported in this work were calculated from the components of the synthesis gel, *i.e.*, no elemental analysis was done to determine the SARs of the final zeolites produced. For ease of reference, these zeolites are designated as ZSM-X (Y), where X is Mobil zeolite number and Y is the SAR.

2.2 Experimental: Zeolite synthesis

The procedures for the synthesis of the zeolites ZSM-22, ZSM-48, ZBM-30 and ZSM-23 are presented. Different parameters were varied during the preparation of the zeolites. A Parr reactor with a capacity of 1000 ml was used for the synthesis of all the zeolites, and is pictured in figure 2.1.

Figure 2.1 Zeolite synthesis equipment: The 1000 ml Parr reactor.

2.2.1 Synthesis of ZSM-22

The general descriptions of the reagents and amounts used for the synthesis of zeolite ZSM-22 are given in table 2.1. Hexamethylenediamine (HMDA) was used as structure-directing agent (SDA).

Table 2.1 : Reagents used for the synthesis of ZSM-22 zeolites.

Reagents	ZSM-22 (60)	ZSM-22 (80)	ZSM-22 (120)
	Amount		
Silica source (Colloidal silica, Ludox AS-40, Aldrich)	69.4 ml	91.1 ml	132.5 ml
Alumina source [$Al_2(SO_4)_3.18H_2O$, 98 %, Aldrich]	6.782 g	6.676 g	6.472 g
SDA (HMDA, 70 %, Aldrich)	50.2 ml	49.4 ml	47.9 ml
Mineraliser [Potassium hydroxide, 85 %, Rochelle]	17.117 g	16.848 g	16.332 g
Solvent (Distilled water)	591.5 ml	564.5 ml	513.0 ml

The ZSM-22 zeolites were synthesised using the procedure reported by Bygnningsbacka *et al.* [1], with some modifications, which entailed variations of the SARs. The synthesis gels used had the following molar composition:

$$27\ HMDA: 13\ K_2O: Al_2O_3: x\ SiO_2: 3670\ H_2O$$

Two solutions, A and B, were prepared. Solution A was prepared by mixing colloidal silica and distilled water in a beaker without stirring. This solution was then stirred for 15 min. Solution B was prepared by mixing aluminium sulphate octadecahydrate, distilled water, HMDA and potassium hydroxide in a beaker, followed by stirring for 15 min. Solution B was then transferred into solution A under vigorous stirring and the stirring continued for 30 min. The mixture was then transferred into a 1000 ml Parr reactor and allowed to crystallise at 160 ^{o}C for 72 h

with stirring. The reactor was then allowed to cool to room temperature. The crystalline white product was recovered by vacuum filtration and washed with distilled water until the pH of the filtrate was 7. The washed product was dried in an oven at 110 ^{o}C for 12 h, followed by calcination at 550 ^{o}C for 15 h.

2.2.2 Synthesis of ZSM-48

The ZSM-48 zeolites were synthesised using different SDAs, namely, HMDA, pyrrolidine and hexamethonium bromide ($HMBr_2$), following previously reported procedures [2 - 4].

2.2.2.1 Synthesis using HMDA as SDA

The list of reagents used for this synthesis is presented in table 2.2 below.

Table 2.2 : Reagents used for the HMDA-directed synthesis of ZSM-48.

Reagents	Amount
Silica source (Colloidal silica, Ludox AS-40, Aldrich)	247.580 g
Alumina source [$Al_2(SO_4)_3.18H_2O$, 100-110 %, Riedel-de Haen]	6.135 g
SDA (HMDA, 70 %, Aldrich)	278.2 ml
Mineraliser (NaOH, 99 %, Rochelle)	7.070 g
Solvent (Distilled water)	323.3 ml

Zeolite ZSM-48 was synthesised using the procedure previously reported by Zhao *et al.* [2], with some modifications, which included the concentration of the mineraliser and SDA. The molar composition of the synthesis gel was as follows:

$$0.0083\ Al_2O_3: SiO_2: 0.08\ Na_2O: 25\ H_2O: 1.35\ HMDA$$

In a typical synthesis, sodium hydroxide was mixed with distilled water in a beaker and stirred until a clear solution was obtained. To this solution, HMDA was added under stirring, followed by the addition of aluminium sulphate octadecahydrate. Lastly colloidal silica was added to the aluminium sulphate octadecahydrate mixture and stirred until homogeneity was attained. After aging at room temperature for 2 h, the mixture was transferred into the 1000 ml Parr reactor and allowed to crystallise at 160 ^{o}C for 96 h with stirring. After crystallisation the reactor was cooled to room temperature. The product was filtered, washed with distilled water until the pH of the filtrate was 7 and then dried at 120 ^{o}C overnight. The SDA was removed by calcination at 600 ^{o}C for 3 h.

2.2.2.2 Synthesis using pyrrolidine as SDA

Table 2.3 shows the sources, assay and the amount of the reagents used for the synthesis of the zeolite ZSM-48.

Table 2.3 : Reagents used for the pyrrolidine-directed synthesis of ZSM-48.

Reagents	Amount
Silica source (Fumed silica, Aerosil200, Degussa)	26.704 g
Alumina source [$Al(NO_3)_3.9H_2O$, 98.5 %, Aldrich]	2.836 g
SDA (pyrrolidine, 99 %, Aldrich)	30.9 ml
Mineraliser (NaOH, 99 %, Rochelle)	12.870 g
pH modifier (H_2SO_4, 98 %, Rochelle)	8.1 ml
Solvent (Distilled water)	666.2 ml

A modification of the procedure reported by Meriaudeau *et al*. [3] was used. The synthesis gel consisted of the following molar composition:

$$0.5\ Al_2O_3: 60\ SiO_2: 43\ NaOH: 20\ H_2SO_4: 50\ pyrrolidine: 5000\ H_2O$$

Fumed silica was added to an aqueous solution of sodium hydroxide and distilled water in a beaker, under vigorous stirring. To this solution, pyrrolidine, aluminium nitrate nonahydrate dissolved in sulphuric acid, and distilled water were added. The hydrogel was stirred for 3 h at room temperature, transferred into the 1000 ml Parr reactor and allowed to crystallise at 180 ^{o}C for 48 h, with stirring. After

crystallisation the autoclave was cooled to room temperature. The white crystalline product was then recovered by vacuum filtration and washed with distilled water until the pH of the filtrate was 7. The product was dried at 120 ^{o}C overnight and the SDA was then removed by calcination at 550 ^{o}C for 15 h.

2.2.2.3 Synthesis using $HMBr_2$ as SDA

Table 2.4 below provides the details of the reagents used for the synthesis of zeolite ZSM-48.

Table 2.4 : Reagents used for the $HMBr_2$-directed synthesis of ZSM-48.

Reagents	Amount
Silica source (Fumed silica, Aerosil 200, Degussa)	23.010 g
Alumina source [$Al(OH)_3$, 98 %, Merck]	0.500 g
SDA ($HMBr_2$, 100 %, Aldrich)	5.780 g
Mineraliser (NaOH, 99 %, Rochelle)	1.080 g
Water (Distilled water)	344.6 ml

The synthesis procedure followed was previously reported by Giordano *et al*. [4], without any modifications. The molar gel composition used for this synthesis was as follows:

$$6\ Na_2O:\ 2.5\ HMBr_2:\ 60\ SiO_2:\ 0.5\ Al_2O_3:3000\ H_2O$$

The zeolite was synthesised by mixing aluminium hydroxide with distilled water in a beaker and stirred to a clear solution, followed by addition of an aqueous solution of sodium hydroxide, and further homogenised by stirring. To the resulting

solution, $HMBr_2$ was added, and stirred until a homogeneous mixture was obtained. Lastly, fumed silica was added under stirring and the mixture was again stirred until homogeneity. The final synthesis mixture was transferred into a 1000 ml Parr reactor and allowed to crystallise at 160 ^{o}C. Three crystallisation times were used for this synthesis, *viz.,* 72 h, 96 h and 168 h. After crystallisation the reactor was allowed to cool to room temperature. The white crystalline product was recovered by vacuum filtration, washed with distilled water until the pH of the filtrate was 7 and dried at 120 ^{o}C overnight. The SDA was removed by calcination at 550 ^{o}C for 10 h.

2.2.3 Synthesis of ZBM-30

One synthesis procedure of ZBM-30 followed involved the use of triethylenetetramine (TETA) as SDA, and the other procedure involved the use of a 1:1 mixture of TETA and pyrrolidine.

2.3.3.1 Synthesis using TETA as SDA

The reagents and amounts used for the synthesis of ZBM-30 are given in table 2.5.

Table 2.5 : Reagents used for the TETA-templated synthesis of ZBM-30.

Reagents	Amount
Silica source (Fumed silica, Aerosil 200, Degussa)	43.565 g
Alumina source [$Al(OH)_3$, 98 %, Merck]	0.939 g
SDA (TETA, 60 %, Aldrich)	90.0 ml
Water (Distilled water)	617.1 ml

The procedure adopted for the synthesis of ZBM-30 was that previously reported by Hastoy *et al*. [5], without any modification, and with the following molar composition:

$$0.5\ \text{TETA}: 0.083\ Al_2O_3: SiO_2: 50\ H_2O$$

Triethylenetetramine was mixed with distilled water in a beaker. To this solution, fumed silica was added under stirring. Aluminium hydroxide was then added to the mixture containing TETA, distilled water and fumed silica and stirred until a homogeneous mixture was obtained. The resulting gel was left to age at room temperature for 2 h, and thereafter transferred to a 1000 ml Parr reactor and allowed to crystallise at 170 ^{o}C for 120 h. After crystallisation the reactor was allowed to cool to room temperature. The white crystalline product was recovered by vacuum filtration, washed with distilled water until the pH of the filtrate was 7 and dried at 100 ^{o}C overnight. The SDA was removed by calcination at 550 ^{o}C for 12 h.

2.2.3.2 Synthesis using a mixture of TETA and pyrrolidine as SDA

The types of sources used and amounts are shown in table 2.6.

Table 2.6 : Details of reagents used for the (TETA + pyrrolidine)-templated synthesis of ZBM-30.

Reagents	Amount
Silica source (Fumed silica, Aerosil 200, Degussa)	47.256 g
Alumina source [$Al(OH)_3$, 98 %, Merck]	1.022 g
SDA [TETA (60 %) + Pyrrolidine (60 %), Aldrich]	465.2 ml + 166.4 ml
Solvent (Distilled water)	101.8 ml

The method used for the synthesis of ZBM-30 using SDA in the form of a mixture of two amine compounds was previously reported by Hastoy *et al.* [5]. It was adopted in this study without any modification, using the following molar gel composition:

286 TETA: 304 pyrrolidine: Al_2O_3: 120 SiO_2: 120 H_2O

A solution of TETA and pyrrolidine in distilled water was prepared in a beaker and stirred. Fumed silica was added under continuous stirring, followed by addition of aluminium hydroxide. The gel was further stirred until a homogenous mixture was obtained, which was then transferred to a 1000 ml Parr reactor, and allowed to crystallise at 170 ^{o}C for 168 h with stirring. After crystallisation the reactor was cooled to room temperature. The white crystalline product was recovered by vacuum filtration, washed with distilled water until the pH of the filtrate was 7, and dried at 100 ^{o}C overnight. The SDA was removed by calcination at 550 ^{o}C for 12 h.

2.2.4 Synthesis of ZSM-23

Table 2.7 shows the list of the reagents used for the synthesis of ZSM-23, together with the amount of each reagent used. Pyrrolidine was used as SDA. This zeolite was synthesised to three SARs of 60, 80 and 120.

Table 2.7 : Reagents used for the synthesis of ZSM-23.

Reagent	ZSM-23 (60)	ZSM-23 (80)	ZSM-23 (120)
	Amount		
Silica source (Fumed silica, Degussa)	14.638 g	19.391 g	28.753 g
Alumina source [$Al(NO_3)_3.9H_2O$,98.5 %, Aldrich]	3.097 g	3.077 g	3.038 g
SDA (pyrrolidine, 99 %)	34.0 ml	33.7 ml	33.3 ml
Mineraliser (NaOH, 99 %, Rochelle)	13.536 g	13.449 g	13.277 g
pH modifier (H_2SO_4, 98 %, Rochelle)	8.4 ml	8.3 ml	8.2 ml
Solvent (Distilled water)	674.2 ml	669.9 ml	661.9 ml

The ZSM-23 zeolites with different SARs were synthesised according to the procedure reported previously by Robson [6], with modification. The molar concentration of the SDA was increased (from 48 to 50) and the crystallisation time was decreased from 50 h to 48 h compared to the procedure reported by Robson [6]. The following molar gel composition was used:

$$0.5\ Al_2O_3 : x\ SiO_2 : 20.6\ Na_2O : 18.8\ H_2SO_4 : 50\ \text{pyrrolidine} : 4610\ H_2O$$

Sodium hydroxide was mixed with distilled water in a beaker, and fumed silica was added to this aqueous solution, under stirring. Aluminium nitrate nonahydrate was also mixed with distilled water in a separate beaker, and then added to the first

mixture of fumed silica and aqueous sodium hydroxide. Thereafter, pyrrolidine and sulphuric acid (dropwise) were added. The homogeneous mixture was stirred for 3 h at room temperature, transferred into a 1000 ml Parr reactor and allowed to crystallise at 180 ^{o}C for 48 h under stirring. After crystallisation the reactor was cooled to room temperature. The crystalline white product was recovered by vacuum filtration, washed with distilled water until the pH of the filtrate was 7, dried at 120 ^{o}C overnight, and finally the SDA was removed by calcination at 550 ^{o}C for 10 h.

2.2.5 Generation of the H-form of the zeolites

The zeolites were converted to the H-form using the following procedure:
Ion-exchange for all samples was carried out using 1 M NH_4Cl solution. The NH_4Cl solution was added to the zeolite sample (10 ml/ g zeolite) and stirred for 1 h at room temperature. After stirring, the mixture was left at room temperature for 30 min. The mixture was then separated by decanting and a fresh NH_4Cl solution was added. The ion-exchange for all the samples was repeated 3 times. The NH_4^+-form of the zeolite sample was then washed free of Cl^- ions (*i.e.,* confirmed by the addition of 1 M $AgNO_3$ solution to the filtrate). The washed sample was then dried in an oven at 110 ^{o}C for 12 h and then calcined at 550 ^{o}C for 3 h.

2.3 Experimental: Physicochemical characterisation

It is essential to characterise the zeolites after synthesis and modification in order to understand their properties. This allows a better rationalisation of their performance in an assigned application. The physicochemical techniques used in this study for the characterisation of the zeolites are XRD, SEM and BET surface area measurements. This section gives details of the instrument used and the procedure followed when characterising the zeolites.

2.3.1 X-ray diffraction

The X-ray diffraction patterns for the various zeolite samples were recorded on a Philips PW 1830 X-ray diffractometer using, a Cu-Kα radiation (λ = 0.15405 nm)

operating at a voltage of 40 kV, and a tube current of 40 mA. The X-ray diffraction patterns were recorded with a scan step size of 0.025^{o} and the goniometer 2θ values varying from 5^{o} to 75^{o} degrees. The selected region of 2θ values ($5 - 50^{o}$) was sufficient to characterise the zeolite phases present. Samples were prepared by gently grinding the solid to a fine powder using a pestle and mortar, after which approximately 1 g of the sample was packed into the sample holder. The XRD patterns were then recorded on the computer equipped with PC-APD diffraction software and saved in Microsoft Excel 2010 format for analysis. The patterns plotted and presented in the results section were obtained using the Origin 6.1 software.

2.3.2 Scanning electron microscopy

To prepare the sample holders, a double-sided tape was mounted on the transparency and cut into 12 mm x 5 mm pieces. During the sample preparation the cover of tape was removed; the piece was held with a fine point tweezers and dipped into sample. The excess material was gently removed from the tape by tapping the tweezers on the side of the sample bottle. The other double-sided tape was mounted on the stub and its covering was taken off. The double-sided tape carrying the material was now mounted on the one that was mounted on the stub. The stub was blown with dry nitrogen to remove the remaining loose material on the stub and the sample holder. One stub could carry ± 14 of the 12 mm x 5 mm pieces of tape carrying different samples.

The stub containing the samples was now put in the Emitted K550X sputter coater (Ashford, England) and coated for 2 min with gold. Samples were viewed in a JSM-840 scanning electron microscope (JEOL, Tokyo, Japan), operated at an accelerating voltage of 5 kV and lowest beam which would achieve the optimum resolution for a specific magnification. The low beam intensity was used as a precaution to avoid sample damage. The images were captured using a frame grabber, Orion 6.604 (Orion, Brussels, Belgium). At least three different spots of each sample were viewed to analyse each sample. Most samples were analysed at the following magnifications: 10 000, 7500, 5 000, 4 000, 3 000, 2 000, 1 000, 500 and 100 times (x). Each sample was therefore analysed for at least 3 h.

2.3.3 Brunauer-Emmett-Teller surface area analysis

The BET surface areas of the synthesised zeolites were measured using a Micromeritics Tristar-Surface area and Porosity Analyser 3000 equipped with a Win 3000 software. Zeolite samples (typical mass 0.15 < m < 0.25 g) were added to the sample tubes and degassed under nitrogen at 200 ^{o}C for 4 h. Brunauer-Emmett-Teller surface area analysis was performed, taking N_2 volume adsorption at relative pressures (P/P_0) in the range of 0.05 - 0.99. The analysis was performed at -196 ^{o}C.

2.4 Results and discussion

2.4.1 X-ray diffraction analysis

The XRD characterisation results and analysis of the four different types of zeolites studied are presented in this section. The method used to calculate relative % XRD crystallinity was adopted from Van Hoof *et al*. [7]. Relative % XRD crystallinities of zeolite samples were calculated using the sum of the intensities of the characteristic peaks (shown by asteriks in the XRD patterns in figures 2.2 and 2.7) and equation 2.1 [7].

$$\text{Relative \% XRD crystallinity} \frac{\sum \text{of the intensities of the characteristic peaks (sample)}}{\sum \text{of the intensities of the characteristic peaks (reference)}} \text{ x } 100 \qquad 2.1$$

Among all the synthesised zeolite samples, the one with the highest sum of the characteristic peak intensities was selected as the reference sample (*i.e.,* 100 % crystalline), and it was used to calculate the relative % XRD crystallinity of the other samples [7]. The width of the most intense diffraction peak gives information about the mean crystallite size of the zeolite samples. Sherrer [8] showed that the relationship between the line broadening at half the maximum intensity and mean crystallite size is given by the following equation:

$$\mathrm{L} = \frac{\lambda}{\Delta \cos \theta} \qquad 2.2$$

where, L is the mean crystallite size; λ is X-ray wavelength; Δ is the line broadening at half the maximum intensity and θ is the Bragg angle (^{o}).

2.4.1.1 ZSM-22

The ZSM-22 zeolites were synthesised at a gel of pH 12 - 13. Figure 2.2 shows the XRD patterns of ZSM-22 samples synthesised at different pH values.

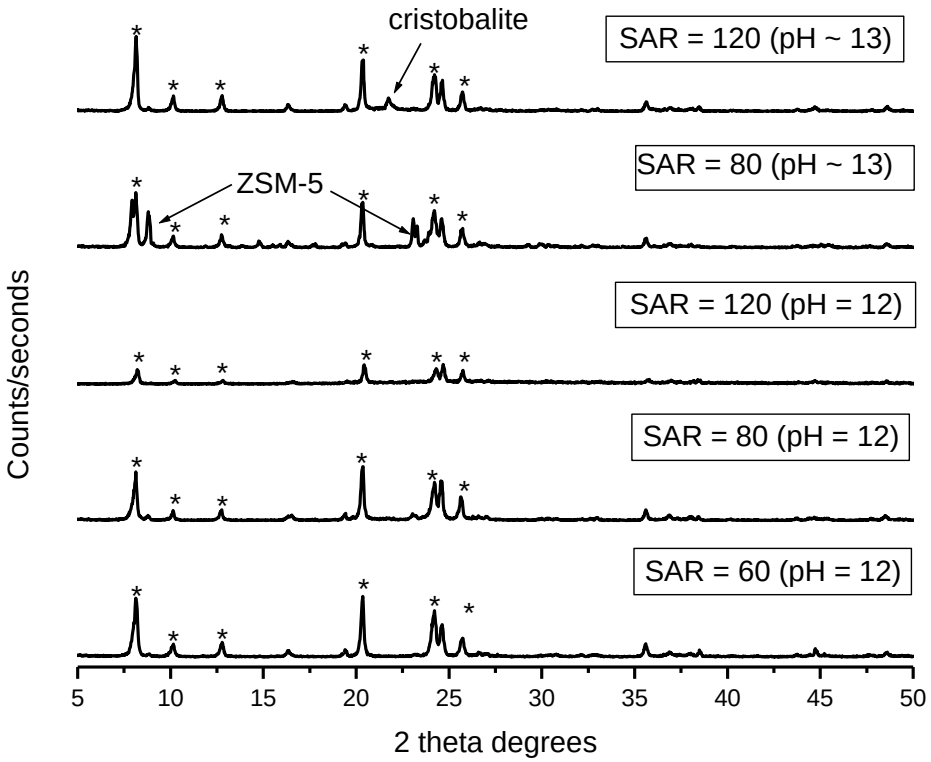

Figure 2.2 The XRD patterns of ZSM-22 synthesised using HMDA as SDA at 160 ^{o}C for 72 h and calcined at 550 ^{o}C for 15 h (asteriks indicate characteristic peaks of the ZSM-22 zeolite).

It is important to note from figure 2.2 that all ZSM-22 materials synthesised at pH 12 show similar diffraction patterns, in accordance with the TON topology [1]. This confirms the successful synthesis of ZSM-22 in this range of SARs. Also worth noting from this figure is the decrease in peak intensities as the SAR of the material increases, suggesting a concomitant decrease in relative crystallinity of these materials as supported by data in table 2.8. Therefore, phase pure ZSM-22 was produced for the three SARs when the pH of the synthesis gel was kept at 12. However, increasing the initial gel pH to 13 degrades the structure of ZSM-22, with foreign phases such as cristobalite and ZSM-5 being detected as impurities for the

SAR of 80 and 120. The formation of these impurities has also been observed by other researchers [9, 10].

To supplement the XRD patterns in figure 2.2, table 2.8 shows the relative % XRD crystallinity of the zeolite ZSM-22 samples calculated using the intensities of the characteristic peaks (as shown by asteriks in figure 2.2) and equation 2.1 (appendix A1). Also shown in table 2.8 is the average crystallite sizes calculated using the Sherrer equation (appendix A3).

Table 2.8 : The relative % XRD crystallinity and average crystallite sizes of the ZSM-22 samples with different SAR and gel pH

SAMPLE	Relative % XRD crystallinity	Average crystallite sizes (μm)
ZSM-22 [SAR = 60 (pH = 12)]	100	0.080
ZSM-22 [SAR = 80 (pH = 12)]	87.3	0.086
ZSM-22 [SAR = 120 (pH = 12)]	34.2	0.080
ZSM-22 [SAR = 80 (pH ~ 13)]	85.5	0.048
ZSM-22 [SAR = 120 (pH ~ 13)]	99.8	0.096

As table 2.8 shows, the ZSM-22 (120) material synthesised at pH 12 has the lowest relative % XRD crystallinity of the three ZSM-22 samples prepared at the same pH. The relative % XRD crystallinity is seen to decrease with increasing SAR for materials prepared from the synthesis gel of pH 12. However, this trend is in contradiction with the known fact, that zeolite materials become more siliceous as SAR increases, thus leading to an increase in relative % XRD crystallinity [11]. Also, there is no specific trend in % XRD crystallinity data for the response of a particular SAR to changes in gel pH from 12 to 13. Compounding to this observation is the co-existence of impurity phases when a synthesis gel of pH 13 was used. The ZSM-22 materials have average crystallite sizes in the range 0.04 - 0.10 μm. Table 2.8 shows that the average crystallite sizes of the ZSM-22 materials synthesised at gel

pH 12 increased with an increase in SAR from 60 to 80 and subsequently decreased as the SAR was increased to 120. The largest and smallest crystallite sizes were observed on materials synthesised at gel pH larger than 12, as shown in table 2.8.

2.4.1.2 ZSM-48

Figure 2.3 below shows the XRD patterns of materials synthesised according to ZSM-48 protocol synthesised using pyrrolidine and HMDA as SDAs, and together with the literature XRD pattern of the material synthesised using pyrrolidine as SDA for comparison.

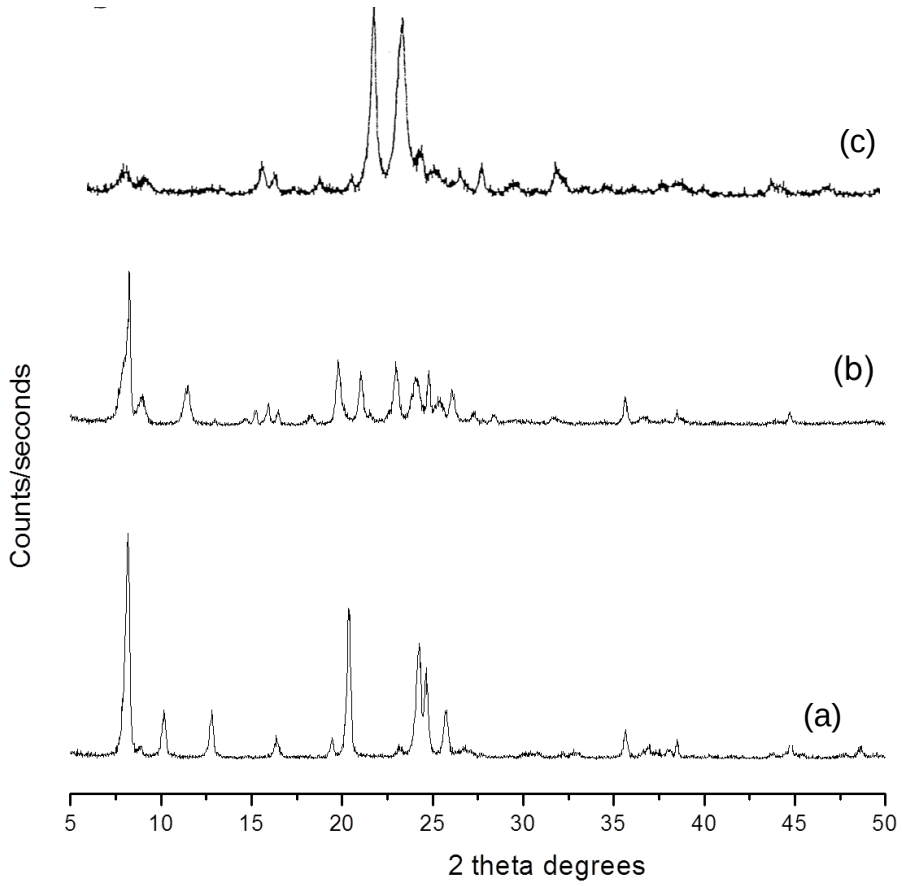

Figure 2.3 The XRD patterns of materials obtained from ZSM-48 synthesis protocols, using different templates: (a) HMDA at 160 ^{o}C for 96 h, (b) pyrrolidine at 180 ^{o}C for 48 h and (c) The reference pattern [3].

As the figure above suggests, none of the two independent synthesis protocols produced the required ZSM-48, because materials produced different XRD

patterns compared to the literature reference. Instead, ZSM-22 [from HMDA, figure 2.3 (a)] and ZSM-23 [from pyrrolidine, figure 2.3 (b)] were produced from these routes as the XRD patterns suggest. This finding is not surprising because HMDA and pyrrolidine are known to direct these zeolite structures, and have also been demonstrated in this chapter (figures 2.2 and 2.7). Since the XRD patterns obtained were not in agreement with that of ZSM-48, another synthesis protocol using $HMBr_2$ as SDA was employed. The XRD patterns of the resulting ZSM-48 materials at different crystallisation times are shown in figure 2.4.

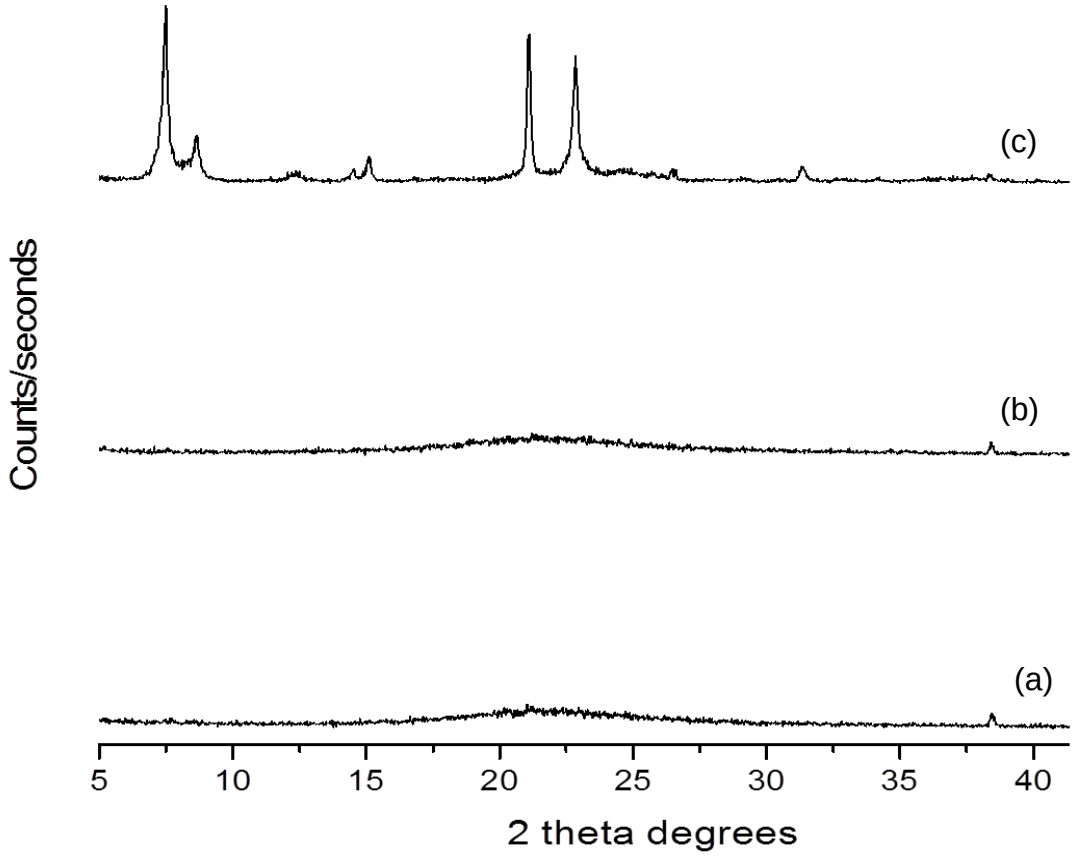

Figure 2.4 The XRD patterns of ZSM-48 crystallised at 160 ^{o}C for (a) 72 h, (b) 96 h and (c) 168 h, using $HMBr_2$ as SDA.

The XRD patterns of the ZSM-48 materials synthesised for 72 and 96 h show that the materials are completely amorphous, as shown by the absence of any Bragg reflections and the appearance of broad hump around 20 - 25^{o} 2θ. The sample synthesised for 196 h exhibit an XRD pattern that is in good agreement with the one reported by Meriaudeau *et al*. [3]. As compared to the XRD pattern reported

by Meriaudeau *et al*. [3], the peak around 6^{o} 2θ in figure 2.4 (c) is more intense, suggesting that the material is highly crystalline. The relative crystallinity of the ZSM-48 samples was not calculated because only one sample synthesised for 168 h was crystalline. The average crystallite size of the ZSM-48 material free of structural impurities was calculated using the Sherrer equation and found to be 0.086 µm.

2.4.1.3 ZBM-30

Zeolite ZBM-30 was synthesised using TETA alone as SDA, and also using a combination of TETA and pyrrolidine to direct the structure. Figure 2.5 shows the XRD pattern of the sample synthesised using TETA as a sole SDA at 170 ^{o}C for 120 h.

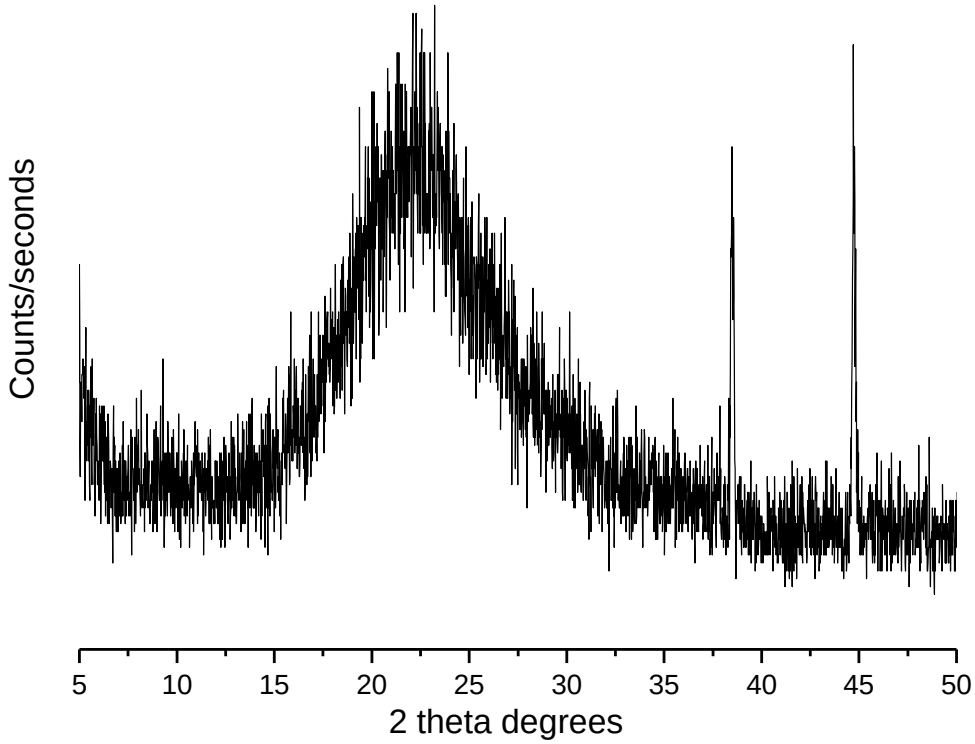

Figure 2.5 The XRD pattern of ZBM-30 synthesised using TETA as SDA at 170 ^{o}C for 120 h.

The appearance of broad hump around 20 - 25^{o} 2θ in figure 2.5 shows that the material produced is completely amorphous and that crystalline ZBM-30 was not produced. An approach of using a dual SDA was then attempted, following the

procedure previously reported by Hastoy *et al.* [5]. Figure 2.6 shows XRD patterns of the material produced using the combination of TETA and pyrrolidine as SDA.

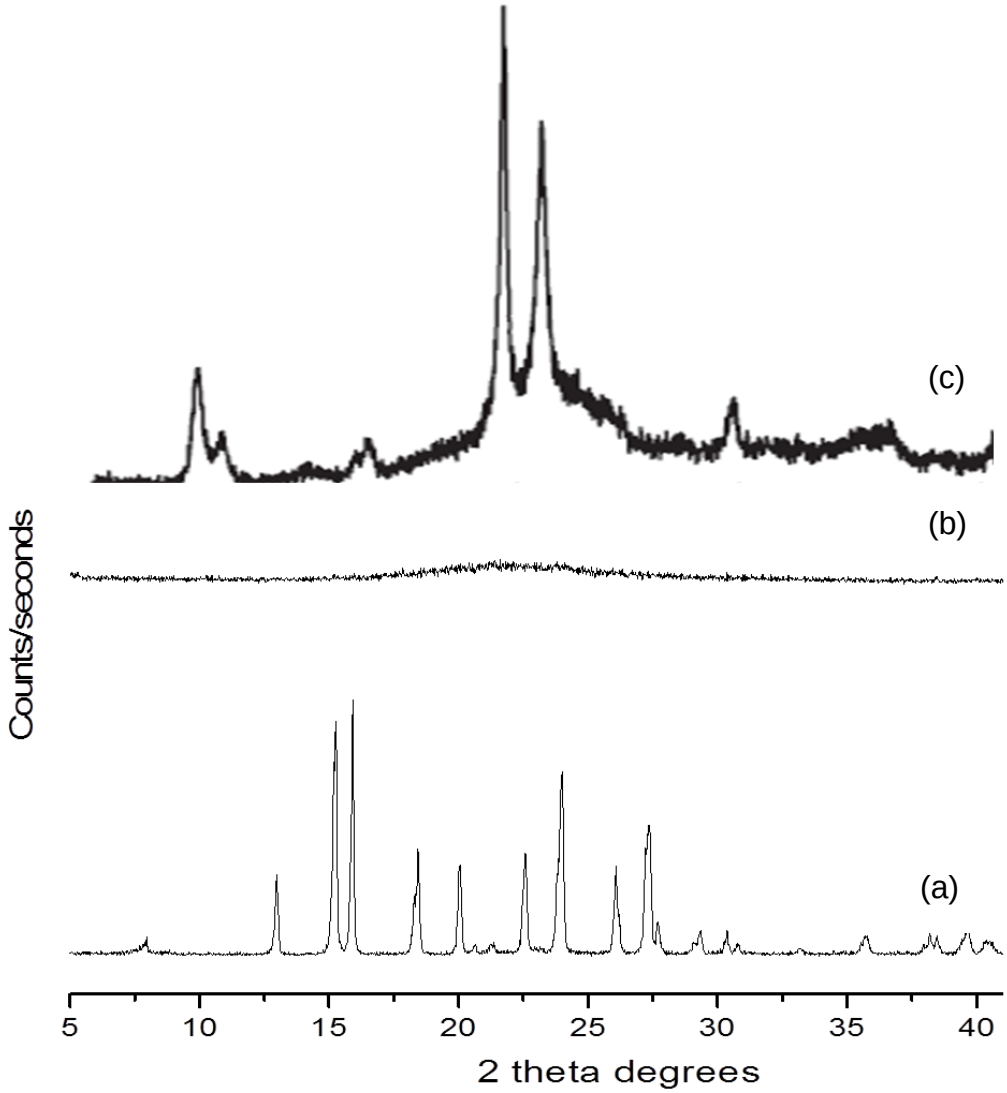

Figure 2.6 The XRD patterns of materials obtained from ZBM-30 synthesis protocols using a combination of TETA and pyrrolidine as SDA at 170 ^{o}C for 168 h, as a function of silica source: (a) Fumed silica (b) Ludox AS-40 (c) The reference pattern [12].

The XRD pattern in figure 2.6 (b) showed that the material produced using Ludox-AS-40 as the silica source is completely amorphous. A crystalline material was produced when fumed silica was used as silica source as evidenced by the absence of the broad XRD feature around 20 - 25^{o} 2θ in figure 2.6 (a). The XRD pattern of the crystalline material in figure 2.6 (a) does not match that of ZBM-30 [figure 2.6 (c)]. By analogy with literature, this XRD pattern shows that the main product formed is ZSM-39 [13], and ZBM-30 was not produced at all. The

synthesis was only limited to one SAR of 120 due to the unsuccessful synthesis of ZBM-30 following the synthesis protocols reported by Hastoy *et al.* [5].

2.4.1.4 ZSM-23

Figure 2.7 shows the XRD patterns of materials synthesised according to ZSM-23 protocol with SARs of 60, 80 and 120, together with the reference XRD pattern reported by Robson [6].

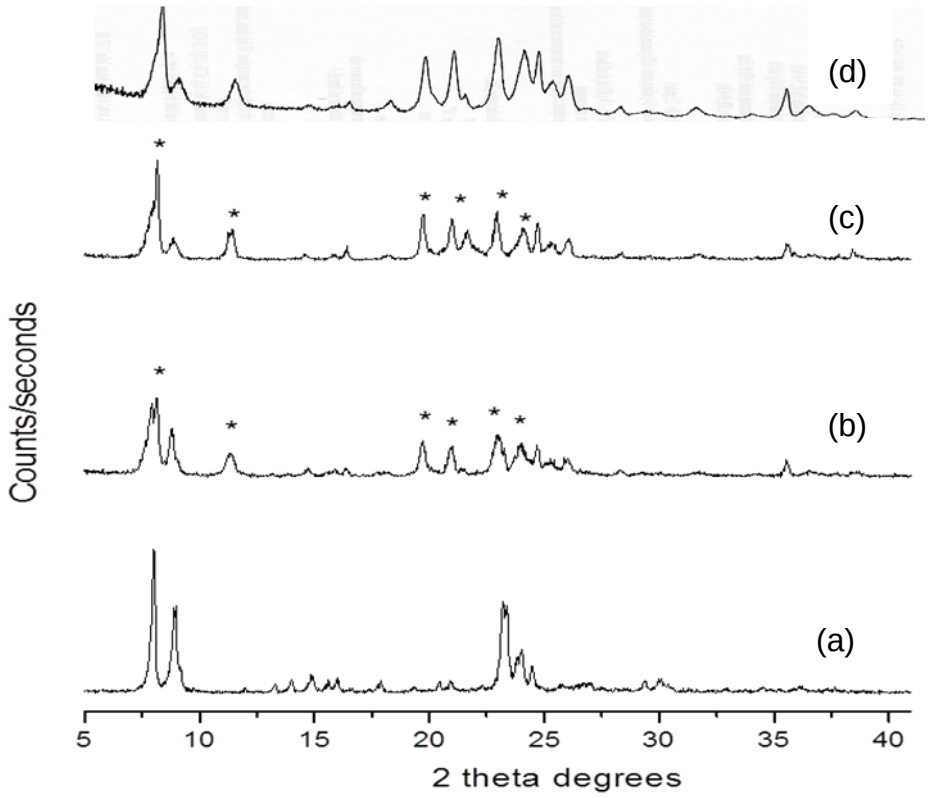

Figure 2.7 The XRD patterns of ZSM-23-type materials synthesised using pyrrolidine as SDA at 180 ^{o}C for 48 h, as a function of SAR : (a) 60, (b) 80 (c) 120 and (d) Literature reference pattern [6]; (with asteriks indicating characteristic peaks).

The XRD pattern of ZSM-23 (120) material is in good agreement with the MTT framework topology as reported in the literature by Robson [6]. All the characteristic peaks (shown by asteriks) in the XRD pattern of MTT framework topology are present without any impurities. Also the XRD pattern of ZSM-23 (80) material is in good agreement with the one reported in the literature [6]. However, the ZSM-23 (60) XRD pattern shows that the material is not pure ZSM-23, since the ZSM-23 characteristic peaks are absent and the dominating phase is that of

ZSM-5 material. Ye *et al.* [14] also reported on the ZSM-5 impurity or competing phase during the synthesis of ZSM-23, which seems difficult to avoid. In their study, Ye *et al*. [14] synthesised ZSM-23 zeolites at different SAR, ranging from 20 to 300, and observed that pure ZSM-5 was the main competing phase at SAR between 30 and 60. They concluded that ZSM-5 is the competitive growth crystal phase at SAR below 60, which seems to support the finding of this study.

Table 2.9 shows the relative % XRD crystallinity of the impurity-free ZSM-23 materials (calculations shown in appendix A2).

Table 2.9 : Relative % XRD crystallinity of the ZSM-23-type samples with different SAR.

Sample	Relative % XRD crystallinity	Average crystallite sizes (μm)
ZSM-23 (60)*	-	0.094
ZSM-23 (80)	81	0.035
ZSM-23 (120)	100	0.080

*ZSM-5 obtained instead of ZSM-23 - Relative % XRD crystallinity not determined because of ZSM-5 phase

The data in table 2.9 suggests that the relative % XRD crystallinity of ZSM-23 materials increases with increasing SAR (> 80). This observation is in line with the expectation that as the SAR increases, a zeolite becomes more siliceous and lead to high relative % XRD crystallinity [11]. Also shown in table 2.9 is the average crystallite size of the ZSM-23 material following the same trend as the relative % XRD crystallinity. The ZSM-23 (60) *(predominantly ZSM-5)* has a larger crystallite size than the pure ZSM-23 (80) and ZSM (120) materials (table 2.9). The relative % XRD crystallinity was not calculated for this material [ZSM-23 (60)], because its XRD pattern suggested it was ZSM-5, and would require a different reference material.

2.4.2 Scanning electron microscopy analysis

Scanning electron micrographs and approximate crystal sizes in terms of average length of the zeolite samples were recorded. The SEM results are presented and discussed below for each zeolite phase obtained.

2.4.2.1 ZSM-22

Figure 2.8 shows the SEM micrographs of ZSM-22 samples synthesised with different SARs. Amongst the five ZSM-22 materials samples synthesised with different gel pH, only the materials tested for hydrocracking of *n*-hexadecane were analysed with SEM.

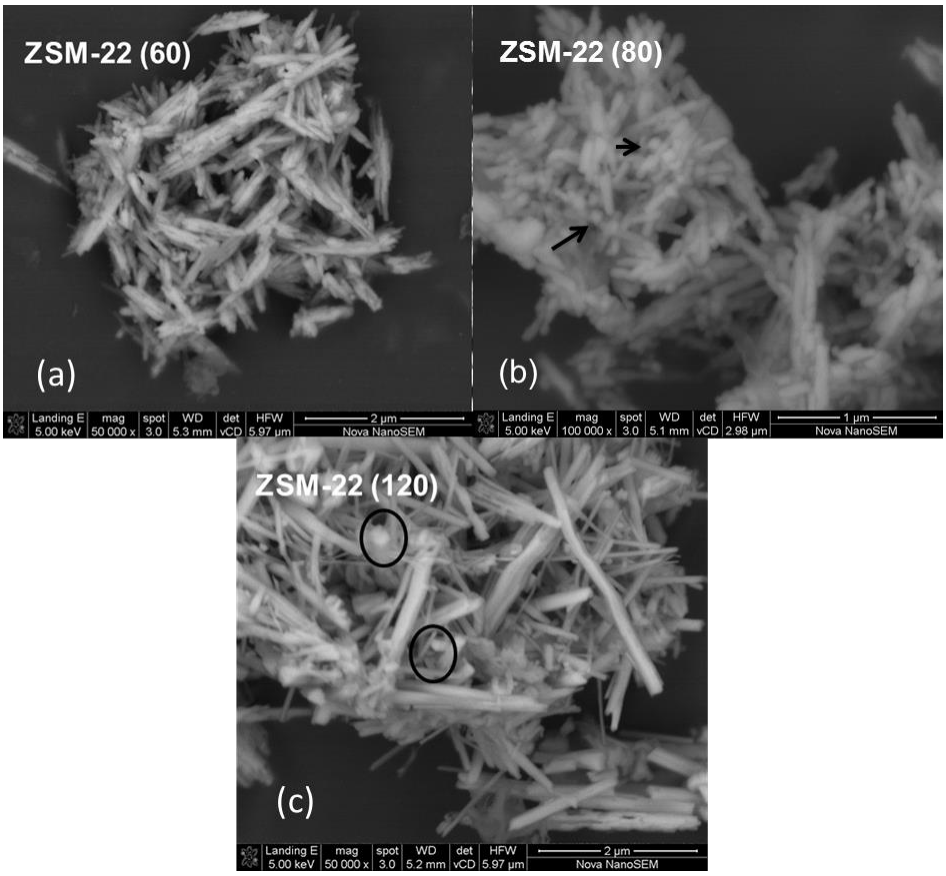

Figure 2.8 The SEM images of ZSM-22 material prepared using HMDA as SDA at 160 ^{o}C for 72 h (calcined at 550 ^{o}C for 15 h), as affected by the gel pH: (a) 12, (b) ~13 (arrows indicating ZSM-5 phases) and (c) ~13 (circles indicating the cristobalite phases).

The crystals of the three ZSM-22 materials are needle-shaped as shown in figure 2.9, which are typical of ZSM-22 materials [10, 15]. It can also be noticed in figure 2.8 (c), that the cristobalite impurity phase is present as round phases (circled), as reported elsewhere [15], and this observation is in line with the XRD pattern of this material in figure 2.2. The needle-shaped crystals of the ZSM-22 (80) material are surrounded by some small spherical crystals (indicated by arrows in figure 2.8) and the XRD pattern of this material in figure 2.2 shows that ZSM-5 phase is present in this material, suggesting that these small spherical crystals may represent ZSM-5 phase. There are no grain-like amorphous phases present on the micrographs, which confirms the absence of amorphous materials outside the zeolite crystals, and is in agreement with the XRD patterns of the materials in figure 2.2.

Table 2.10 shows the crystal lengths of the ZSM-22 materials measured from the SEM micrographs in figure 2.9.

Table 2.10 : The average crystal lengths of ZSM-22 materials synthesised using HMDA as SDA at 160 ^{o}C for 72 h and calcined at 550 ^{o}C for 15 h.

Sample	Average crystal length (μm)
ZSM-22 (60)	0.6
ZSM-22 (80)	1.2
ZSM-22 (120)	1.2

The needle-shaped crystals of the ZSM-22 materials are 0.6 - 1.2 μm in length, as shown in table 2.10. Noteworthy is that the average crystal length of impurity free ZSM-2 (60) material is half the materials having cristobalite and ZSM-5 phases. The observed large crystal particles of the ZSM-22 (80) and ZSM (120) materials can be as a result of the presence of foreign phases in these materials.

2.4.2.2 ZSM-48

The SEM analysis of the materials synthesised using HMDA and pyrrolidine were not done since the materials produced were ZSM-22 and ZSM-23, respectively. The SEM analysis was only done for the ZSM-48 materials synthesised using $HMBr_2$ as SDA at different crystallisation times of 78 h, 96 h and 168 h, and calcined at 550 ^{o}C for 10 h.

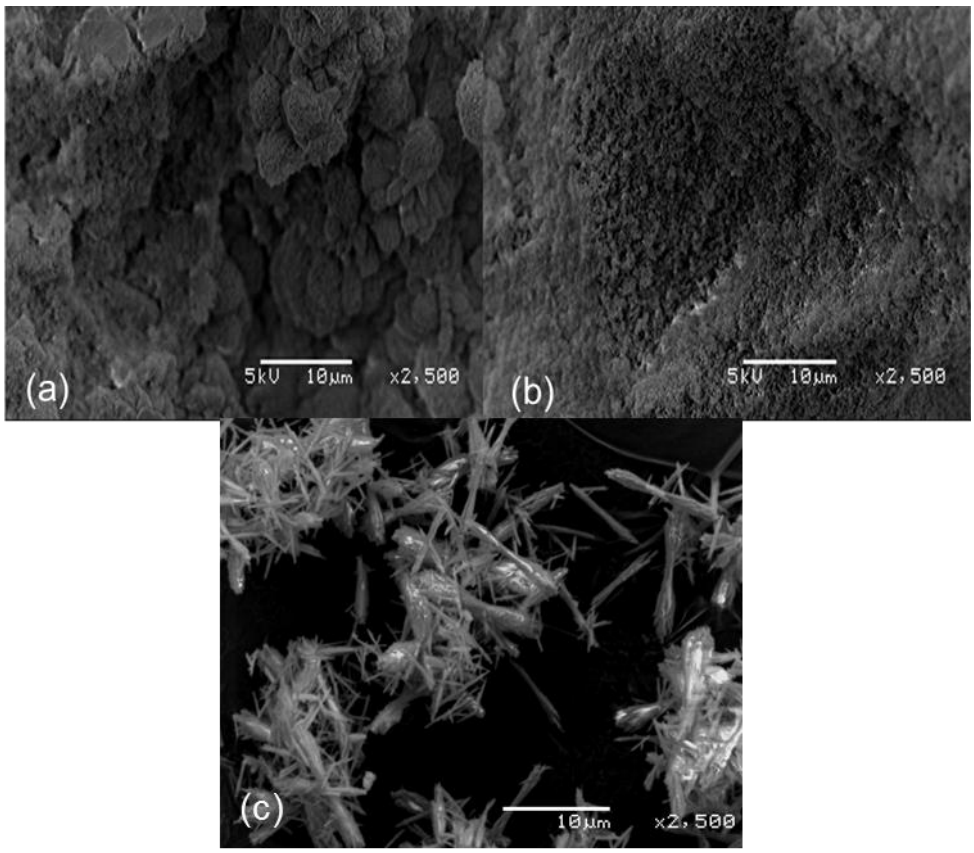

Figure 2.9 The SEM images of ZSM-48 samples synthesised using $HMBr_2$ as SDA for: (a) 72 h (b) 96 h and (c) 168 h, and calcined at 550 ^{o}C for 10 h.

The presence of grain-like phase observed in figure 2.9 (a and b), shows that the materials synthesised for 72 h and 96 h are completely amorphous, which is in good agreement with their XRD patterns (figure 2.4). However, the material synthesised at for 168 h shows needle-shaped crystals 4.2 - 11.3 µm in length. Some of these crystals are found in bundles diverging from a central point where they are connected, which is consistent with other researchers' previous

observations [16]. Figure 2.9 (c) also shows the absence of grain-like amorphous phase. This absence of grain-like phase suggests a change in the structure of ZSM-48 materials from amorphous to highly crystalline material at prolonged crystallisation time and this observation is in line with the XRD patterns of these materials in figure 2.4.

2.4.2.3 ZSM-23

The three materials characterised by SEM were those tested for the hydrocracking of *n*-hexadecane. As explained in the XRD results section, the material produced with SAR of 60 was not ZSM-23 but ZSM-5. Figure 2.10 shows the SEM images of the ZSM-23 samples with different SAR.

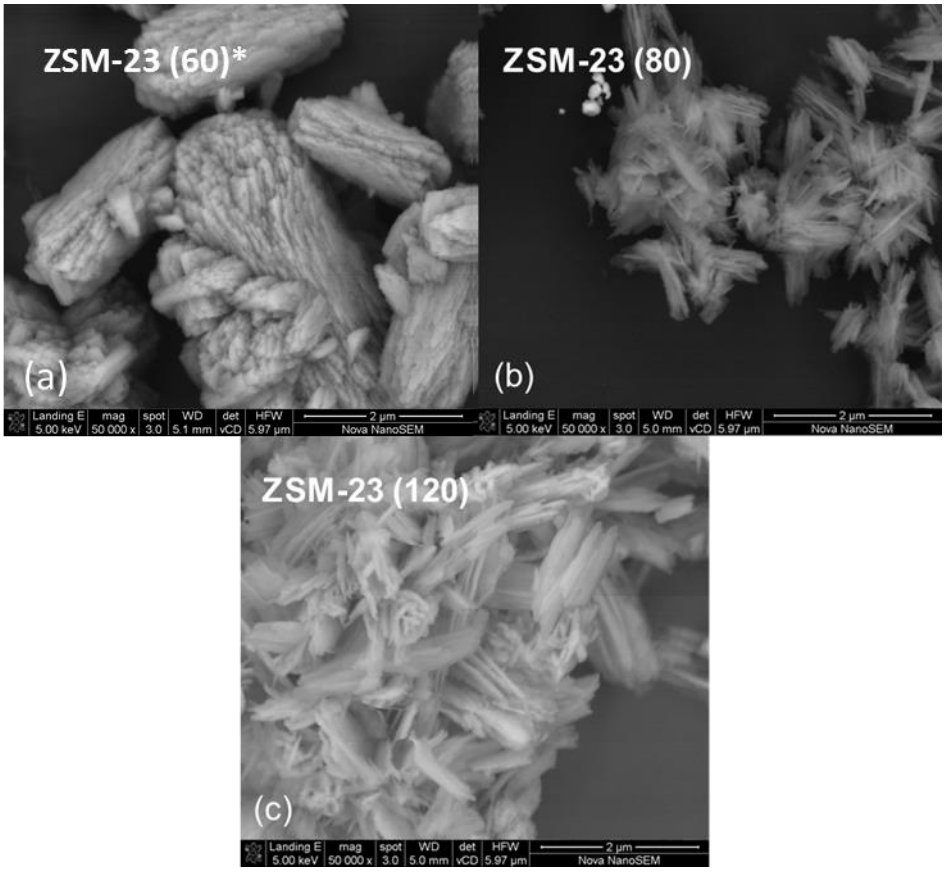

Figure 2.10 The SEM images of the materials prepared using pyrrolidine as SDA at 180 ^{o}C for 48 h and calcined at 550 ^{o}C for 10 h, as a function of SAR: (a) 60 (*ZSM-5 produced), (b) 80 and (c) 120.

The crystals of ZSM-23 (8) materials in figure 2.10 are needle-shaped, with crystal lengths in the range 0.8 - 0.9 µm. Robson [6] also showed that the crystal habit of the ZSM-23 zeolites is that of needles or bundles of needles, which is similar to the observations in this study. The crystal shapes of the material prepared with a synthesis gel of SAR = 60 is that of bundles of rods, and the material produced was ZSM-5 instead of ZSM-23. Table 2.11 presents the average crystal lengths of sizes of the ZSM-23-type materials.

Table 2.11 : The average crystal lengths of ZSM-23-type materials synthesised using pyrrolidine as SDA at 180 °C for 48 h and calcined at 550 ^{o}C for 10 h.

Sample	Average crystal length (µm)
ZSM-23 (60)*	2.4
ZSM-23 (80)	0.8
ZSM-23 (120)	0.9

*ZSM-5 obtained instead of ZSM-23. Hence the outlying result for the crystal length.

The material with SAR = 60 has larger crystals compared to impurity-free ZSM-23 materials, *i.e.*, ZSM-23 (80) and ZSM-23 (120). It can be seen in table 2.11 that the presence of ZSM-5 phase favoured the formation of larger crystals. There is no observable crystal length trend in terms of SAR for the impurity-free ZSM-23 materials and the particle sizes of these materials are almost equal.

2.4.3 BET surface area analysis

The BET surface area measurements were carried out on ZSM-22 and ZSM-23 with SARs of 60, 80 and 120. These zeolites were the only samples impregnated with palladium and tested for catalytic activity in the hydrocracking of *n*-C_{16}.

2.4.3.1 ZSM-22

Table 2.12 shows the variation of BET surface area of ZSM-22 with synthesis parameters (gel pH and SAR).

Table 2.12 : The BET surface areas of ZSM-22 samples.

Zeolite	BET surface area (m^2/g)
ZSM-22 (60), pH 12	189
ZSM-22 (80), pH ~ 13	112
ZSM-22 (120), pH ~ 13	83

The structural impurity-free zeolite ZSM-22 (60), obtained from a gel of pH 12, has the highest BET surface area of 189 m^2/g and which is close to the theoretical BET surface area of the TON structure (230 m^2/g) calculated by simulating the adsorption of nitrogen over the TON structure [15]. From table 2.12, it can be observed that the BET surface areas of the materials obtained from gel pH ~ 13 decreased when the SAR was increased to 120. The reason for lower BET surface area of the ZSM-22 (80) and ZSM-22 (120) materials compared to the ZSM-22 (60) material may be due to the presence of cristobalite and ZSM-5 phases. Teketel *et al.* [15] achieved BET surface areas in the range 98 - 226 m^2/g, which covers the range of the BET surface areas obtained in this study.

2.4.3.2 ZSM-48

The BET surface area measurement revealed that the crystalline ZSM-48 material has a surface area of 124 m^2/g. For ZSM-48 materials, the reported surface areas are around 300 m^2/g [2, 17]. The crystal lengths of this material are in the range 4.2 - 11.3 μm [see figure 2.9 (c)], suggesting that the low surface area obtained compared to the literature surface area can be due to the large crystals of this material.

2.4.3.3 ZSM-23

The BET surface areas of the ZSM-23 samples with SAR of 60 (ZSM-5 impurity phase), 80 and 120 are shown in table 2.12.

Table 2.13 : The BET surface areas of ZSM-23 samples.

Zeolite	BET surface area (m^2/g)
ZSM-23 (60)*	321
ZSM-23 (80)	213
ZSM-23 (120)	204

*ZSM-5 obtained instead of ZSM-23

The trend in the above table suggests the BET surface area decreases with an increase in SAR. A similar trend was observed by Ji *et al.* [19]. However the material with a SAR of 60 was predominately ZSM-5 as deduced from its XRD pattern, and may not be directly compared with the other ZSM-23 zeolites in table 2.13. According to the literature, as the SAR increases the BET surface area decreases [14, 18].

2.5 Conclusions

The synthesis of zeolites ZSM-22, ZSM-48, ZBM-30 and ZSM-23 was carried out. The XRD patterns of the materials showed that ZSM-22, ZSM-48 and ZSM-23 were successfully synthesised, and the synthesis of ZBM-30 was not successful. ZSM-22 materials were prepared to three levels of SARs, *viz.*, 60, 80 and 120. Impurity-free ZSM-22 materials were produced when the synthesis gel of pH 12 was used. However, impurity phases such as cristobalite and ZSM-5 were observed when the synthesis gel pH was increased to 13 for the ZSM-22 (80) and ZSM-22 (120) materials. The relative % XRD crystallinity decreased with an increase in SAR for the materials prepared at gel of pH 12, but there is no observable specific trend in relative % XRD crystallinity data for the response of a particular SAR to changes in gel pH from 12 to 13. SEM images of ZSM-22 zeolites showed that the crystals were needle-shaped. The crystal length of the impurity-free ZSM-22 (60) was found to be half the lengths of the materials containing ZSM-5 and cristobalite impurities, *i.e.,* ZSM-22 (80) and ZSM-22 (120), suggesting that the presence of the impurity phases influences the crystal habit of the ZSM-22 materials. The BET surface area of the ZSM-22 materials decreased with an increase in SAR. The smaller the crystal lengths of the ZSM-22 materials, the higher the BET surface area.

A number of SDAs have been investigated for their ability to direct the structure of ZSM-48 during hydrothermal synthesis. These included HMDA, pyrrolidine and $HMBr_2$. The first two SDAs led to the formation of unexpected zeolitic phases, *viz.,* ZSM-22 (from HMDA) and ZSM-23 (from pyrrolidine). The correct ZSM-48 was only produced using $HMBr_2$, but at prolonged crystallisation time (168 h), as evidenced by the XRD patterns. The material was highly crystalline with no amorphous phase as suggested by the XRD patterns in comparison with that reported in literature. The SEM images of these materials also showed that as the crystallisation time was increased the morphology of the materials changed from grain-like morphology, suggesting an amorphous material, to needle-shaped crystals at higher crystallisation time of 168 h, suggesting a crystalline material. The large crystals of this material led to a low BET surface area of 124 m^2/g, which is lower than the surface areas of ZSM-48 materials reported in the

literature. This successful synthesis at the advanced stage of the research deferred catalytic activity investigations.

Several attempts to synthesise ZBM-30 also failed to produce the expected framework topology as confirmed by XRD. The attempts included the use of TETA and a (1 TETA : 1 pyrrolidine) mixture as SDAs to template the structure of this zeolite. A different zeolite was produced when using (1 TETA : 1 pyrrolidine) mixture as SDA, *viz.,* ZSM-39. As a consequence of the failure to produce the correct material, catalytic activity was not tested on these products.

Pyrrolidine was also used to direct the structure of ZSM-23 to three levels of SARs. Two of these SARs produced materials with the expected XRD signatures for ZSM-23, namely 80 and 120, with the lower SAR of 60 producing pure ZSM-5 under the same synthesis conditions from a similar synthesis gel. The SAR was also found to have an effect on the relative % XRD crystallinity, whereby the increase in SAR was accompanied by the increase in relative XRD crystallinity. The crystals of ZSM-23 materials were needle-shaped, with lengths shorter than those of the ZSM-23 (60) predominantly ZSM-5. It was observed that the crystal behaviour of this ZSM-23 (60) material was in the form of bundles of rods, which is not typical of ZSM-23 materials, thus complementing the XRD patterns. The BET surface area of the ZSM-23 (60) was the highest in comparison with the impurity-free ZSM-23 materials. The BET surface area of the impurity-free ZSM-23 materials decreased slightly upon increasing the SAR from 80 to 120.

2.6 References

[1] R. Byggningsbacka, L. Lindfors, N. kumar, Catalytic activity of ZSM-22 zeolites in the skeletal isomerization reaction of 1-butene, Industrial and Engineering Chemistry Research, volume 36, 1997, pages 2990-2995.

[2] G. Zhao, J. Teng, Y. Zhang, Z. Xie, Y. Yue, Q. Chen, Y. Tang, Synthesis of ZSM-48 zeolites and their catalytic performance in C_4-olefin cracking reactions, Applied Catalysis A: General, volume 299, 2006, pages167-174.

[3] P. Meriaudeau, V. A. Tuan, V. T. Nghiem, G. Sapaly, C. Naccache, Comparative evaluation of the catalytic properties of SAPO-31 and ZSM-48 for the hydroisomerization of n-octane: Effect of the acidity, Journal of Catalysis, volume 185, 1999, pages 435-444.

[4] G. Giordano, J. B. Nagy, E. G. Derouane, Zeolite synthesis in presence of hexamethonium ions, Journal of Molecular Catalysis, volume 305, 2009, pages 34-39.

[5] G. Hastoy, E. Guillon, J. Martens, Method for synthesizing ZBM-30 zeolite from a mixture of amine compounds, United States Patent 7544347 B2, 2009.

[6] H. Robson, Verified synthesis of zeolitic materials, 2001, page 217.

[7] J. H. C Van Hooff, J. W. Roelofsen, Techniques of zeolite characterization, Studies in Surface Science and Catalysis, volume 85, 1991, pages 241-283.

[8] P. Scherrer; Bestimmung der grosse und der inneren Struktur von der kolloidteilchen mittels Röntgenstrahlen, Gottinger News, volume 2, 1918, page 98.

[9] D. Verboekend, A. M. Chabaneix, K. Thomas, J. Gilson, J. Perez-Ramirez, Mesoporous ZSM-22 zeolite obtained by desilication: Peculiarities associated with crystal morphology and aluminium distribution, Crystal Engineering Communications, volume 13, 2011, pages 3408-3416.

[10] D. Masih, T. Kobayashi, T. Baba, Hydrothermal synthesis of pure ZSM-22 under mild conditions, Chemical Communications, Issue 31, 2007, pages 3303-3305.

[11] N. H. Tamer, Synthesis and characterization of zeolite beta, MSc thesis, The Graduate School of Natural and Applied Sciences of Middle East Technical University, Turkey, 2006.

[12] C. Bouchy, G. Hastoy, E. Guillon, J. A. Martens, Fischer-Tropsch waxes upgrading via hydrocracking and selective hydroisomerization, Oil Gas Science and Technology- Rev. IFP., volume 64, 2009, pages 91-112.

[13] H. Gies, Crystal structure of dodecasil 3C, another synthetic clathrate compound of silica, Journal of Crystallography, volume 167, 1984, pages 73-82.

[14] L. Ye, W. Zhendong, L. Yun, L. Xianbo, L. Yueming, W. Peng, Synthesis of ZSM-23 zeolite using isopropylamine as template, Chinese Journal of Catalysis, volume 30, 2009, pages 525-530.

[15] S. Teketel, Studies of the Methanol-to-hydrocarbon (MTH) reaction over new 8- and 10-ring acidic zeolites, MSc thesis, University of Oslo, Norway, 2009.

[16] K. Suzuki, T. Hayakawa, The effects of seeding in the synthesis of zeolite ZSM-48 in the presence of tetramethylammonium ion, Microporous and Mesoporous Materials, volume 77, 2005, pages 131-137.

[17] S. Teketel, W. Skistad, S. Benard, U. Olsbye, K. P. Lillerud, P. Beato, S. Svelle, Shape selectivity in the conversion of methanol to hydrocarbons: The catalytic performance of one-dimensional 10-ring zeolites: ZSM-22, ZSM-23, ZSM-48, and EU-1, American Chemical Society Catalysis, volume 2, 2012, pages 26-37.

[18] D. Ji, B. Wang, G. Qian, Q. Gao, G. Lu, L. Yan, J. Suo, A highly efficient catalytic C4 alkane cracking over zeolite ZSM-23, Catalysis Communications, volume 6, 2005, pages 297-30.

CHAPTER 3
Zeolite-based catalysts for the hydrocracking of *n*-hexadecane

3.1 Introduction

The literature in Chapter 1 shows that a great deal of research on the use of medium-pore zeolites as supports for hydrocracking and hydroisomerisation noble metal catalysts were focused on using short-chain hydrocarbons, neither of which is representative of low-temperature Fischer-Tropsch (LTFT) wax [1-5]. The *n*-hexadecane (*n*-C_{16}) used in this study was chosen because of its high molecular weight to be representative of LTFT wax. It also allows for a simpler experimental handling and the reaction products can be analysed in reasonable time using gas chromatography (GC).

The activity and selectivity of noble metal catalysts supported on zeolites for the hydrocracking of *n*-C_{16} were investigated in this study. Palladium (Pd) was chosen as the noble metal catalyst supported on zeolites ZSM-22 and ZSM-23. Several factors such as silica-alumina ratio (SAR), surface area and size of the zeolite crystallite on the product distribution, reaction conditions [*i.e.*, temperature and weight hourly space velocity (WHSV)] were investigated in this study. The WHSV is defined as the mass flow rate of the reactant molecules divided by the mass of the catalyst in the reactor. The reciprocal of WHSV is a measure of the time spent by reactant molecules in contact with the catalyst.

The conditions used, mainly in terms of temperature and pressure, were those typical for cracking products obtained by LTFT synthesis. A trickle bed reactor used was equipped with a vaporiser so that the products are in vapour phase before analysis by an on-line GC.

3.2 Experimental

3.2.1 Preparation of Pd/zeolite catalysts

The zeolites used in this study have been synthesised according to procedures described in Chapter 2. Each zeolite was synthesised to three SARs. Hydrocracking catalysts were prepared by incipient wetness impregnation method of these zeolites with aqueous solutions of $[Pd(NH_3)_4](NO_3)_2$ (6.4 wt. %, Alfa Aesar) to achieve Pd loadings 0.5 wt. %. Calculation of the amount of Pd complex required to achieve this loading was accomplished by using equation 3.1:

$$M_m = (M_z \times W_m)/W_s \qquad 3.1$$

where,

M_m = mass of the noble metal complex (g) (salt)

M_z = mass of the zeolite (g)

W_m = desired metal loading (%)

W_s = noble metal complex assay (%)

About 2 g of each zeolite support was used for the loading. The metal precursor (0.156 g) was mixed with water to ensure the volume of the solution is equal to that of the zeolite pore volume. The metal complex and the water solution were then mixed with the support until it was incipient wet. The bifunctional wet catalyst was left to dry overnight at room temperature, compressed into flakes using a stainless steel press die at 147 kPa, crushed and sieved to particle sizes of 500 - 850 µm. The catalysts were pelletised in order to minimise the hydrodynamic wall effects, reduce the pressure drop over the reactor and to handle easily during loading into the reactor.

3.2.2 Catalytic activity studies

3.2.2.1 The reactor

Figure 3.1 shows the schematic representation of the reactor used for the hydrocracking experiments. It consists of a stainless steel tube with body length of 50 cm.

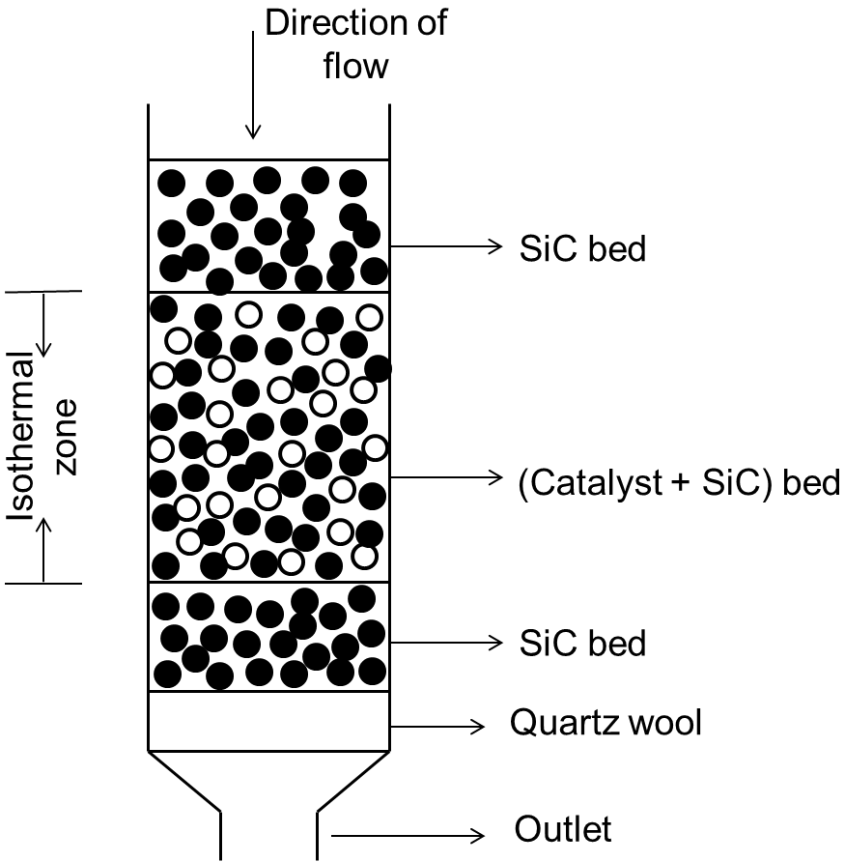

Figure 3.1 Schematic representation of the hydrocracking reactor used.

3.2.2.2 Catalytic loading and hydrocracking of *n*-C_{16}

Before each loading of the catalyst into the reactor, the reactor was rinsed with acetone, and left to dry. A small piece of glass wool was placed around the central thermowell and pushed to the bottom to cover the outlet port of the reactor. Silicon carbide (SiC) was added into the reactor until the beginning of the isothermal zone, followed by the physical mixture of the pelletised catalyst (2 g) and SiC (20 g) and finally by gentle tapping to help settle the bed to a height of 40 cm below

the upper lip of the reactor (*i.e.*, the beginning of the isothermal zone). The reactor was filled to within approximately 1 cm of the top with SiC and while gently tapping to help settle the bed.

Prior to the catalytic test run, each catalyst was reduced in hydrogen for 6.7 h at 350 ^{o}C. The temperature was increased to 350 ^{o}C (1 ^{o}C /min) and kept isothermal for 2.5 h. Nitrogen gas (N_2) was flushed through at a rate of 250 ml/min for 0.4 h and thereafter hydrogen gas (H_2) was also flushed through at rate of 50 ml/min at 450 ^{o}C. Finally the temperature was dropped to the desired reaction temperature (215 - 255 ^{o}C) in H_2/N_2. The feed *n*-C_{16} (99 %, Sigma-Aldrich) was then introduced into the reactor after the catalyst reduction and the catalytic test run was started. The reactor pressure used was 20 bar, WHSV = 0.5 h^{-1} and 1.0 h^{-1}, and H_2/C_{16} mole ratio = 10 was used during the course of the catalytic test runs. The products were analysed with an on-line GC.

The GC (Varian 3900) was equipped with non-polar column and a flame ionisation detector, and H_2 gas was used as a carrier gas. The results presented are on a carbon basis. The total conversion (conversion *via* cracking and isomerisation) was calculated using the following equation:

$$\text{Conversion (mol \%)} = 1 - \frac{\mathrm{A}_{n-\mathrm{C}_{16}}}{\sum_{i=\mathrm{C}_1}^{n-\mathrm{C}_{16}} \mathrm{A}_{\mathrm{C}_i}} \qquad 3.2$$

where, $\mathrm{A}_{n-\mathrm{C}_{16}}$ is the peak area of unconverted *n*-C_{16}. The selectivity of cracking and isomerisation was obtained using the following equation:

$$\text{Selectivity (mol \%)} = \frac{\mathrm{A}_i \mathrm{C}_i}{\sum_{i=\mathrm{C}_1}^{n-\mathrm{C}_{16}} \mathrm{A}_{\mathrm{C}_i}} \qquad 3.3$$

where, A_i is the peak area corresponding to carbon species C_i.

3.3 Results and discussion

Since the main focus of this work is on hydrocracking, the results of this study were mainly discussed in terms of the selectivity to *n*-C_{16} cracking and less about the selectivity to C_{16} isomerisation (*i*-C_{16}). The influence of reaction conditions (*i.e.*, temperature and WHSV) and physical properties (*i.e.*, surface area, SAR and crystallite size) on the activity and selectivity of some of the zeolites used in the hydrocracking experiments was investigated. It must be noted that the presence of *n*-C_{16} species will be omitted in the product distribution analysis, due to their presence in the feed.

3.3.1 Hydrocracking of *n*-C_{16} over Pd/ZSM-22 catalysts

3.3.1.1 The effect of reaction conditions on conversion and selectivity to cracking products

The reaction temperatures used for the zeolite-based catalysts were 215 ^{o}C and 225 ^{o}C. Table 3.1 shows the catalytic activity data for Pd/ZSM-22 catalysts of different SARs (60, 80 and 120).

Table 3.1 : The *n*-C_{16} cracking results over ZSM-22-based catalysts.

Experimental conditions and catalytic parameters	ZSM-22 (60) (impurity-free) 0.080 μm (XRD) 321 m^2/g (BET)		ZSM-22 (80) (with ZSM-5-impurity) 0.048 μm (XRD) 213 m^2/g (BET)		ZSM-22 (120) (with cristobalite impurity) 0.096 μm (XRD) 204 m^2/g (BET)		
Reaction temperature (^oC)	215	225	225	225	225	230	235
WHSV (h^{-1})	0.5	0.5	0.5	1.0	0.5	0.5	0.5
Conversion (mol %)	24.6	34.5	97.5	42.1	8.5	11.4	16.3
Cracking selectivity (mol %)	9.4	12.8	95.2	77.8	61.0	67.2	65.6
i-C_{16} selectivity (mol %)	90.6	87.2	4.8	22.2	39	32.8	34.4
C_4/C_{12}	1.6	1.9	11.3	7.1	6.6	5.0	5.5

Typical reaction temperatures ranged from 215 ^oC to 235 ^oC. The conversion generally increased with increasing reaction temperature over the Pd/ZSM-22 (60) and Pd/ZSM-22 (120) catalysts. This increase in conversion with increasing reaction temperature can be attributed to the increase in the kinetic energy of the

reactant molecules, leading to higher reactivity [6]. It is known that as the reaction temperature increases, the thermal cracking component increases, thus leading to an increase in cracking products [7]. Interestingly, the catalytic cracking selectivity of the Pd/ZSM-22 (60) showed a pure increase with reaction temperature, while the Pd/ZSM-22 (120) catalysts increased through a maximum and decreased as the reaction temperature increased to 235 ^{o}C. It is important to note that of the three SARs studied, only that of 60 showed performance close to ideal behaviour, with C_4/C_{12} ratios of 1.6 and 1.9, *i.e*., less secondary cracking occurred over the Pd/ZSM-22 (60) catalyst. At shorter contact times, fresh reactant molecules flush out the other reactant molecules already in contact with the catalyst [6], hence when the WHSV was increased from 0.5 h^{-1} to 1.0 h^{-1} (shortened contact time), the conversion decreased from 97.5 % to 42.1 % and the catalytic cracking selectivity decreased from 95.2 % to 77.8 %. The reported data correspond to the steady state activity rather than the initial activity of the catalysts, hence the error bars are relatively small.

3.3.1.2 The effect of SAR on catalytic activity and selectivity to cracking products

The conversion increased from 34.5 % to 97.5 % as the SAR increased from 60 to 80 and then decreased to 8.5 % upon further increase of the SAR to 120 at a reaction temperature of 225 ^{o}C and constant WHSV of 0.5 h^{-1} (see table 3.1). The observed results in terms of conversion are not in line with literature, because according to literature the increase in SAR, which is the decrease in acid sites, it is expected that the increase in SAR should correlate with a decrease in conversion [7, 8]. The observed results could be as a result of the ZSM-5 and cristobalite impurities present in the ZSM-22 (80) and ZSM-22 (120) supports, respectively.

.

The relationship between the selectivity to cracking products and the SAR of the ZSM-22-based catalysts was also investigated at a reaction temperature of 225 ^{o}C and WHSV of 0.5 h^{-1}. Figure 3.2 (plotted using data in table 3.1) shows the relationship between the SAR of the ZSM-22-based catalysts and the selectivity to cracking products.

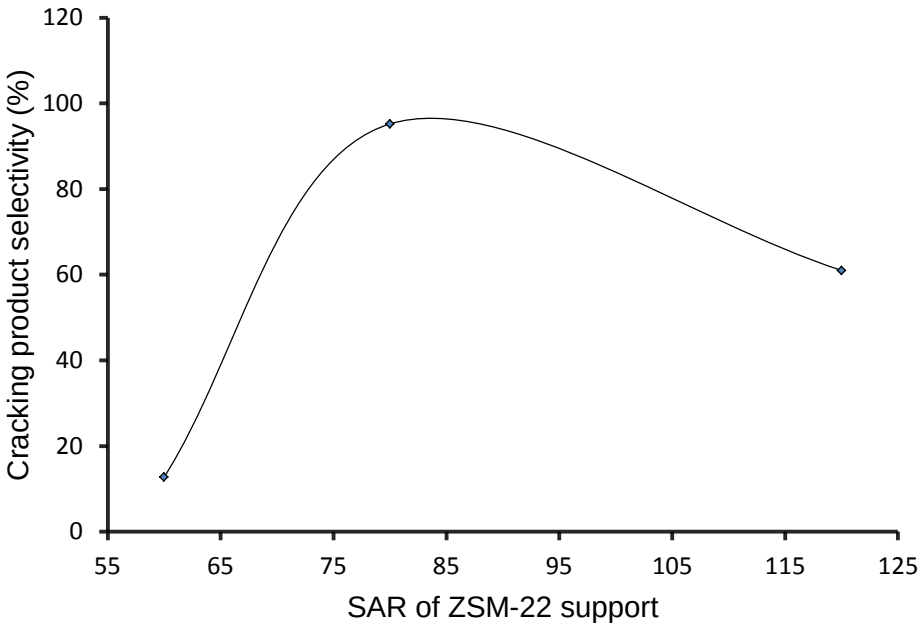

Figure 3.2 Cracking product selectivity as a function of the SAR of ZSM-22 support in the hydrocracking of *n*-C_{16} at 225 ^{o}C and WHSV of 0.5 h^{-1}.

The selectivity to cracking products seems to increase to a maximum and then decrease. The Pd/ZSM-22 (60) catalyst achieved the lowest catalytic cracking selectivity and is highly selective to isomerisation (*i*-C_{16}) (table 3.1). However, one would expect highest cracking selectivity over the Pd/ZSM-22 (60) catalysts by virtue of its low SAR (more acidity) [7, 8]. The observed high selectivity to *i*-C_{16} can be best explained by pore mouth lock-and-key catalysis being more prevalent on the external surface of the ZSM-22 zeolite crystals [9]. In relation to these result, Claude *et al.* [9], showed that over Pt/ZSM-22 (60) catalyst, the *n*-C_{16} feed penetrated with one end into a pore opening or with both ends each into a different pore opening and thus leading to the production of more of *i*-C_{16} compared to cracked products. The high selectivity to *i*-C_{16} was due to the acid sites located in the pore very near the pore entrance [9]. It is worth noting that the *n*-C_{16} conversion also follows the same trend as a function of SAR.

3.3.1.3 The effect of BET surface area of ZSM-22 support on the catalytic activity and selectivity to cracking products

Table 3.2 shows how the BET surface area (discussed in Chapter 2) of the ZSM-22 materials is related to the conversion and catalytic cracking selectivity.

Table 3.2 : Correlation of ZSM-22 BET surface area with catalytic data at 225 ^{o}C` and WHSV of 0.5 h^{-1}.

Sample	BET surface area (m^2/g)	Conversion (mol %)	Catalytic cracking selectivity (mol %)
ZSM-22 (60)	189	34.5	12.8
ZSM-22 (80)	112	97.5	95.2
ZSM-22 (120)	83	8.5	61.0

The Pd/ZSM-22 (120) is less active compared to the other ZSM-22-based catalysts, probably due to its lower BET surface area. However, the catalytic cracking selectivity is higher compared to that achieved over the Pd/ZSM-22 (60) with higher BET surface area and higher conversion. The Pd/ZSM-22 (80) catalyst with BET surface area of 112 m^2/g is the best performer in the series, in terms of both *n*-C_{16} conversion and selectivity to cracked products.

3.3.1.4 The effect of structural properties of ZSM-22 support on the catalytic perfomance

The table 3.3 shows the relative % XRD crystallinity and crystallite size of ZSM-22 materials (discussed in Chapter 2), and their effect on *n*-C_{16} conversion and catalytic cracking selectivity.

Table 3.3 : Correlation of XRD structural data of ZSM-22 with catalytic perfomance.

Sample	Relative % XRD crystallinity	Crystallite sizes (μm)	Conversion (mol %)	Catalytic cracking selectivity (mol %)
ZSM-22 (60)	100	0.080	34.5	12.8
ZSM-22 (80)	85.5	0.048	97.5	95.2
ZSM-22 (120)	99.8	0.096	8.5	61.0

From table 3.3, it can be seen that the ZSM-22 (80) support with the lowest relative % XRD crystallinity and small crystallite size is more active compared to the other ZSM-22 (60 and 120) supports. It is also observed in table 3.3 that the selectivity to cracking products increases with decreasing relative % XRD crystallinity of the three supports.

3.3.1.5 Product distribution over ZSM-22-based catalysts

The product distributions for the hydrocracking of *n*-C_{16} on various ZSM-22-based catalysts are shown in figure 3.3.

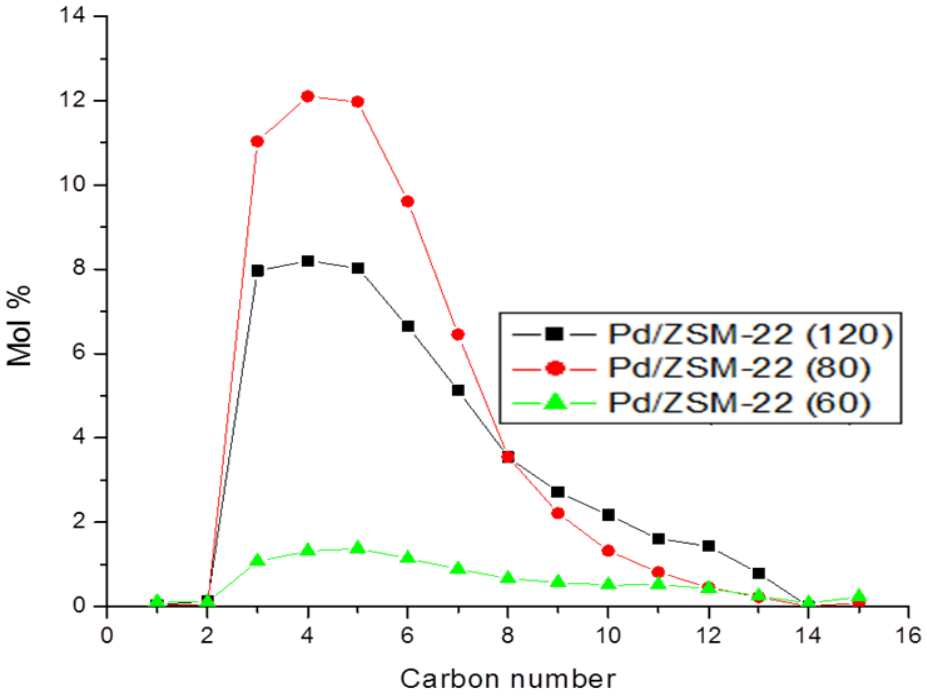

Figure 3.3 Carbon number distributions of the hydrocracking products of *n*-C_{16} over ZSM-22-based catalysts (temperature = 225 ^{o}C and WHSV = 0.5 h^{-1}).

There are virtually no C_1, C_2, C_{14} and C_{15} products appearing in the product distributions of the three ZSM-22-based catalysts. The absence of these products suggest that the metal-catalysed reactions (methanolysis and hydrogenolysis), which are mono-functional reactions did not occur, implying that a bifunctional mechanism occurred [10, 11]. The product distributions of all the ZSM-22-based catalysts show a maximum around C_3 - C_6 implying that secondary cracking occurred [11, 12]. The Pd/ZSM-22 (80) catalyst produced the most C_3 - C_6 hydrocarbons followed by Pd/ZSM-22 (120) and Pd/ZSM-22 (60) catalysts.

The amount of secondary cracking that occurred is normally measured by the C_4/C_{12} ratio. If C_4/C_{12} = 1, then pure primary cracking (ideal hydrocracking) occurs. If C_4/C_{12} > 1, then secondary cracking (non-ideal hydrocracking) occurs. Also, if C_4/C_{12} >> 1, then secondary cracking is more extensive [11]. The C_4/C_{12} ratio of Pd/ZSM-22 (80) is 11.3, which is about double that of Pd/ZSM-22 (120), *i.e.*, 6.6 in table 3.1. These high values of C_4/C_{12} ratios show that these catalysts are far from ideal behaviour and that the extent of secondary cracking is worse for these two cases. Evidence for this observation can be seen in figure 3.3, wherein the C_4 selectivity of Pd/ZSM-22 (80) is higher than that of Pd/ZSM-22 (120). Less

secondary cracking occurred over Pd/ZSM-22 (60) catalyst, with C_4/C_{12} ratio of 1.9 (see table 3.1) and is also evidenced in figure 3.3 with low C_4 selectivity.

3.3.2 Hydrocracking of *n*-C_{16} over ZSM-23 based catalysts

3.3.2.1 The effect of reaction conditions on conversion and selectivity to cracking products

The reaction conditions used for this investigation are similar to those used for ZSM-22-based catalysts. The WHSV was also kept constant at 0.5 h^{-1} for the ZSM-23 (80) and ZSM-23 (120)-based catalysts, and increased from 0.5 h^{-1} to 1.0 h^{-1} for the ZSM-23 (60) based catalyst and the details are presented in table 3.4.

Table 3.4 : The *n*-C_{16} cracking results over ZSM-23-based catalysts.

Experimental conditions and catalytic parameters	ZSM-23 (60)*		ZSM-23 (80)		ZSM-23 (120)		
Reaction temperature (^oC)	225	225	215	225	225	230	235
WHSV (h^{-1})	0.5	1.0	0.5	0.5	0.5	0.5	0.5
Conversion (mol %)	99.9	79.0	14.5	42.0	4.3	6.2	8.8
Cracking selectivity (mol %)	100	96.9	71.6	76.0	14.3	22.9	29.9
i-C_{16} selectivity (mol %)	0	3.1	28.4	24.0	85.7	77.1	70.1
C_4/C_{12}	-	11.7	7.8	5.2	2.2	1.5	2.3

*ZSM-5 obtained instead of ZSM-23.

As shown in table 3.4, no C_{12} was produced over the Pd/ZSM-23 (60)* catalyst, hence no entry of the C_4/C_{12} ratio value at WHSV = 0.5 h^{-1}. The conversion increases with an increase in reaction temperature over both the Pd/ZSM-23 (80) and Pd/ZSM-23 (120) catalysts. This increase in conversion is also attributed to the increase in kinetic energy of the *n*-C_{16} molecules as the temperature increases [6].

The catalytic cracking selectivity also increases with increasing reaction temperature over the Pd/ZSM-23 (80) and Pd/ZSM-22-1(20) catalysts. As with the ZSM-22-based catalysts, the results obtained can be attributed to the increase in the thermal cracking component as the reaction temperature increases [7]. The Pd/ZSM-23 (60)* shows a decrease in conversion and catalytic cracking selectivity with an increase in WHSV, which is similar to what was observed over the Pd/ZSM-22 (80) catalyst (see table 3.1). At reaction temperature of 225 ^{o}C and WHSV of 0.5 h^{-1}, this catalyst, Pd/ZSM-23 (60)*, (dominated by the ZSM-5 phase) achieved the highest conversion and cracking selectivity compared to the pure ZSM-23-based catalysts.

3.2.2.2 The effect of SAR on catalytic activity and selectivity to cracking products

The conversion of the *n*-C_{16} feedstock decreased with an increase in SAR of the supports. The highest conversion (99.9 %) was achieved over Pd/ZSM-23 (60)* and lowest conversion achieved (4.3 %) over Pd/ZSM-23 (120) (table 3.4). The Pd/ZSM-23 (120) is less active because of few active sites present in the zeolite lattice due the high SAR as compared to both Pd/ZSM-23 (60 and 80) [6, 7]. Figure 3.4 (plotted using data in table 3.4) shows the relationship between the SAR of the ZSM-23 support and catalytic cracking selectivity at 225 ^{o}C.

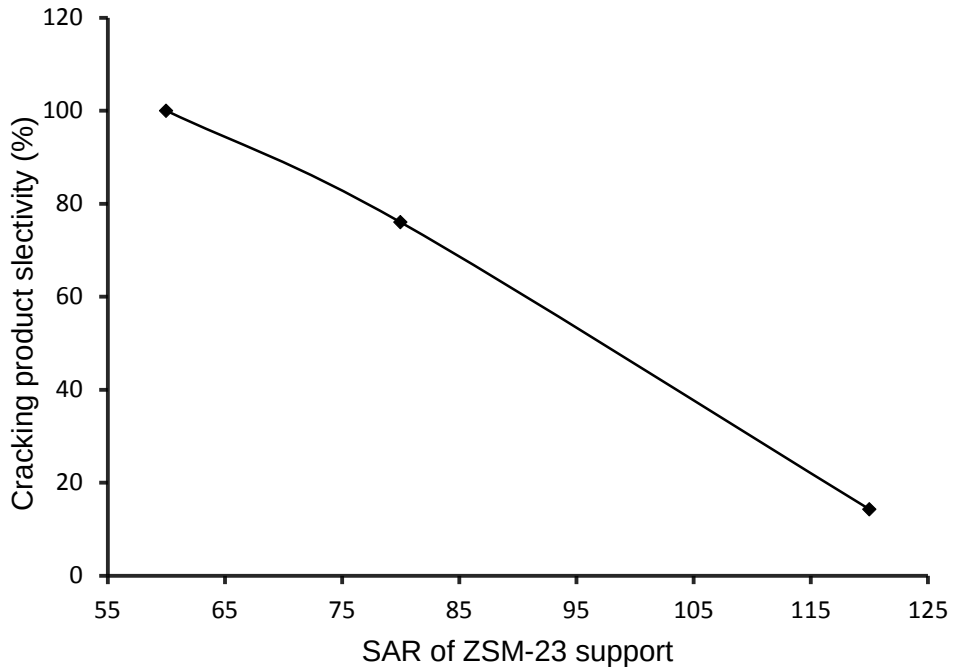

Figure 3.4 Cracking product selectivity v/s the SAR of ZSM-23 support in the hydrocracking of *n*-C_{16}.

Comparison of the ZSM-23-based catalysts at reaction temperature of 225 ^{o}C shows a clear decrease in the selectivity to cracking products with increasing SAR (figure 3.4). It is interesting to note that for the ZSM-23-based catalyst at reaction temperature of 225 ^{o}C, the low SAR favours the high selectivity to cracking products. This observed trend can be due to the available acid sites present on each catalyst as the SAR decreases, since cracking occurs at the acid function of the zeolite, and therefore, the more acid sites present the more the cracking selectivity [6 - 8]. It is also worth noting that the decrease in cracking selectivity with SAR is accompanied by an increase in isomerisation selectivity (*i*-C_{16}).

3.3.2.3 The effect of BET surface area ZSM-23 support on the catalytic activity and selectivity to cracking products

The table below shows how the catalytic conversion and cracking selectivity vary with the BET surface area of ZSM-23 materials.

Table 3.5 : The correlation of BET surface area with conversion and catalytic cracking selectivity over ZSM-23 supports at 225 ^{o}C.

Sample	BET surface area (m^2/g)	Conversion (mol %)	Catalytic cracking selectivity (mol %)
ZSM-23 (60)*	321	99.9	100
ZSM-23 (80)	213	42.0	76.0
ZSM-23 (120)	204	4.3	14.3

*ZSM-5 obtained instead of ZSM-23

It is observed that the highest conversion and catalytic cracking selectivity were obtained over the Pd/ZSM-23 (60)* with the highest BET surface area. Over the three ZSM-23-based catalysts, the conversion and catalytic cracking selectivity increase with an increase in BET surface area of the supports. This can be attributed to the higher surface area giving rise to higher accessibility of the *n*-C_{16} molecules to the active sites of the support.

3.3.2.4 The effect of structural properties of ZSM-23 support on the catalytic perfomance

Table 3.6 shows the relative % XRD crystallinity and crystallite sizes of the ZSM-23 materials (discussed in Chapter 2). Also shown in table 3.6 is the conversion and catalytic cracking selectivity obtained over ZSM-23-based catalysts.

Table 3.6: Correlation of XRD structural data of ZSM-23 with catalytic perfomance.

Sample	Relative % XRD crystallinity	Crystallite sizes (μm)	Conversion (mol %)	Catalytic cracking selectivity (mol %)
ZSM-23 (60)*	-	0.094	99.9	100
ZSM-23 (80)	81.0	0.035	42.0	76.0
ZSM-23 (120)	100	0.080	4.3	14.3

*ZSM-5 obtained instead of ZSM-23 (see Chapter 2)

The catalytic cracking selectivity and conversion decreases with an increase in relative % XRD crystallinity of the pure ZSM-23 materials. Worthy to note is that the material with 100 % crystallinity is less selective to cracking products, which is similar to the 100 % relative ZSM-22 (60) material. The predominantly ZSM-5 material [ZSM-23 (60)] with the largest crystallite size is more active and highly selective to cracking reactions, achieving 100 mol % cracking selectivity.

3.3.2.5 Product distribution over ZSM-23-based catalysts

The figure below shows the product distributions for the hydrocracking of *n*-C_{16} on ZSM-23-based catalysts under similar reaction conditions.

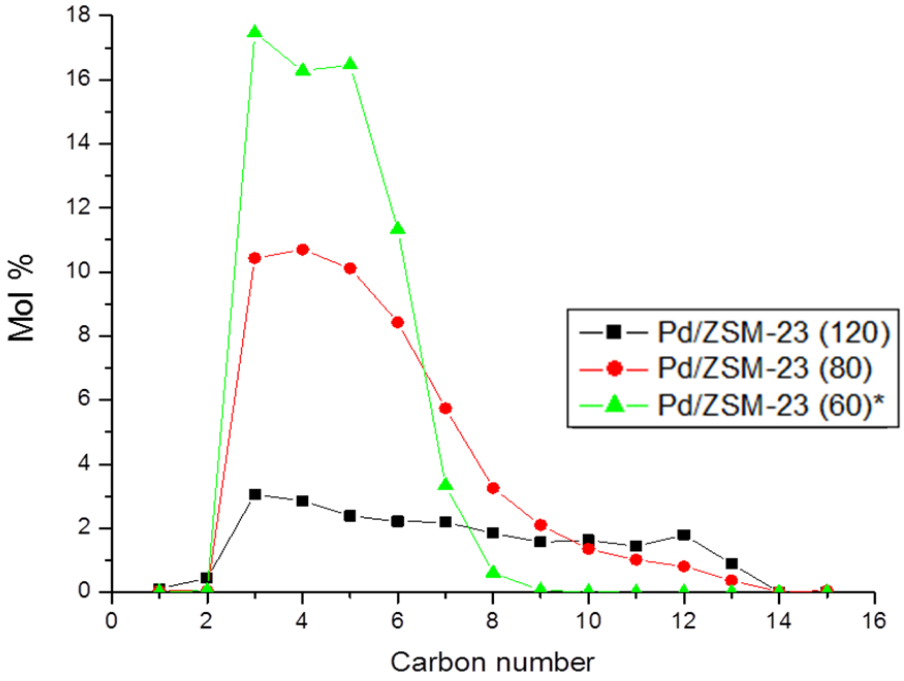

Figure 3.5 Carbon number distributions of the hydrocracking products of *n*-C_{16} over ZSM-23-based catalysts (Temperature = 225 ^{o}C and WHSV = 0.5 h^{-1}).

The selectivity to C_1 and C_2 gaseous products over the three catalysts is very low (< 1) and can be neglected. Also there is virtually no C_{14} and C_{15} formed over the three catalysts, suggesting that the metal-catalysed reactions (methanolysis and hydrogenolysis) did not occur, thus implying that only bifunctional mechanism occurred [10, 11]. The Pd/ZSM-23 (80) and Pd/ZSM-23 (60)* catalysts' product distributions show a maximum at C_3 - C_6, with the most C_3 - C_6 produced over the Pd/ZSM-23 (60)* catalyst, implying that secondary cracking occurred excessively over this catalyst. Similar behaviour of ZSM-5-based catalysts during the hydrocracking of *n*-C_{16} was observed by Ndimande [11] and Kukard [12], with the product distributions of Pd/ZSM-5 (90) showing a maximum around low carbon numbers (C_3 - C_6), suggesting that these ZSM-5 containing catalysts at low Pd loadings (< 1 wt. %) favours secondary cracking [11, 12]. The Pd/ZSM-23 (120) catalyst product distribution shows that less secondary cracking occurred over this

catalyst and the C_4/C_{12} ratio is not too high (see table 3.4), suggesting an approach to ideal cracking behaviour.

3.3.3 Hydrocracking over a physical mixture of Pd/ZSM-5 (90) and Pd/ZSM-22 (60) catalysts

This study on the composite catalysts involving a physical mixture of ZSM-5 (90) and ZSM-22 (60) based catalysts was prompted by the presence of ZSM-5 phase in ZSM-22 (80) (Chapter 2), which showed both a high conversion and high selectivity to cracking products. It is therefore not meant for a direct comparison with the catalysts in this study, because of the many variables that are involved. The Pd/ZSM-22 (60) catalyst that gave the highest *i*-C_{16} selectivity of 87.2 % (see table 3.1) was physically mixed with Pd/ZSM-5 (90) catalyst. The Pd loading of the Pd/ZSM-5 and Pd/ZSM-22 catalysts was 0.5 %. The two catalysts were physically mixed to investigate the effect of synergism. The evidence of a synergism would be the mono-branching of *n*-C_{16} to *i*-C_{16} [over Pd/ZSM-22 (60)] leading to pure primary cracking over the Pd/ZSM-5 (90) catalyst.

Table 3.7 shows catalytic activity data of the Pd/ZSM-5 (90) and the catalyst comprising of the mixture of Pd/ZSM-5 (90) and Pd/ZSM-22 (60). For ease of reference, the catalyst comprising of the physical mixture of Pd/ZSM-5 (90) and Pd/ZSM-22 (60) will be designated as Pd/ZSM-5/ZSM-22 in this chapter.

Table 3.7 : The *n*-C_{16} cracking results obtained over Pd/ZSM-5/ZSM-22 and Pd/ZSM-5 (90) catalysts.

Experimental conditions and catalytic parameters	ZSM-5 (90)	Pd/ZSM-5/ZSM-22				
Reaction temperature (^oC)	225	225	230	235	245	255
WHSV (h^{-1})	1.0	1.0	1.0	1.0	1.0	1.0
Conversion (mol %)	72.7	18.2	25.5	34.9	67.7	93.0
Cracking selectivity (mol %)	97.3	53.4	55.3	55.5	63.1	73.1
i-C_{16} selectivity (%)	2.7	46.6	44.7	44.5	36.9	26.9
C_4/C_{12}	6.4	1.1	1.2	1.2	1.5	1.7

The cracking selectivity of Pd/ZSM-5/ZSM-22 is less than that obtained over Pd/ZSM-5 (90), but higher than that obtained over Pd/ZSM-22 (60) (table 3.1). The C_4/C_{12} = 1.1 obtained over Pd/ZSM-5/ZSM-22 catalyst at 225 ^oC, suggest an ideal hydrocracking behaviour since less secondary cracking occurred. Even though

secondary cracking was reduced, it is not pure primary cracking and thus not showing any real evidence of synergism.

3.3.3.1 The effect of reaction temperature on the catalytic activity and selectivity to cracking products over Pd/ZSM-5/ZSM-22

Figure 3.6 shows the relationship between the conversion, selectivity (*i*-C_{16} and cracking) and the reaction temperature at WHSV of 1.0 h^{-1}, plotted using the data in table 3.7.

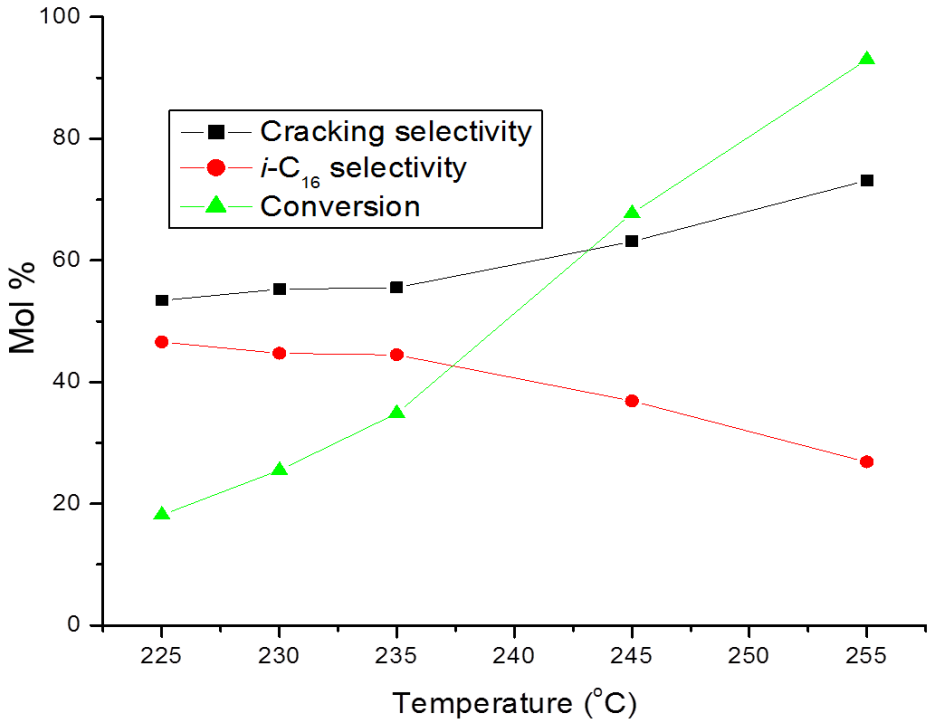

Figure 3.6 The conversion, *i*-C_{16} selectivity and cracking selectivity as a function of temperature over Pd/ZSM-5/ZSM-22 catalyst.

The conversion increases with increasing reaction temperature. Similar to the Pd/ZSM-23 (120) and Pd/ZSM-22 (120), this increase in conversion with increasing temperature can be attributed to the increase in the kinetic energy of the reactant molecules [6]. As the reaction temperature increases from 225 ^{o}C to 255 ^{o}C, the cracking selectivity increases from 55.3 % to 73.1 %, which can be ascribed to the thermal cracking component increasing with an increase in

reaction temperature [7]. The reaction temperature increase is also accompanied by the decrease in *i*-C_{16} selectivity.

3.3.3.2 Product distribution over Pd/ZSM-5/ZSM-22 at reaction temperature of 225 ^{o}C

Figure 3.7 shows the product distributions obtained over Pd/ZSM-5/ZSM/22, Pd/ZSM-22 (60) and Pd/ZSM-5 (90) catalysts.

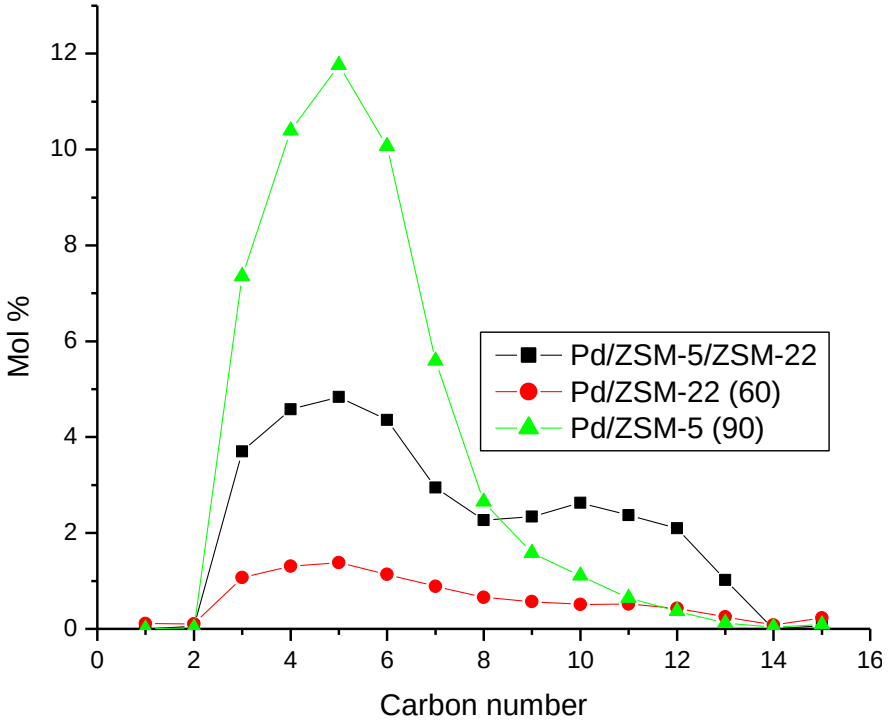

Figure 3.7 Carbon number distributions of the *n*-C_{16} hydrocracking products over Pd/ZSM-5/ZSM-22, Pd/ZSM-22 (60) and Pd/ZSM-5 (90) at 225 ^{o}C.

The amount of C_1, C_2, C_{14} and C_{15} formed for the three catalysts is negligible confirming that no metal-catalysed reactions occurred [10, 11]. The product distribution over the ZSM-5-based catalyst is a maximum around C_3 - C_6, clearly showing that secondary cracking occurred [11]. The secondary cracking observed in figure 3.7 over ZSM-5-based catalyst is also supported by the C_4/C_{12} of 6.2 (table 3.7). The product distribution over the physical mixture also shows a maximum around C_3 - C_6, but the amount of C_3 - C_6 products is less compared to that obtained over Pd/ZSM-5 (90), suggesting that less secondary cracking occurred over the Pd/ZSM-5/ZSM-22. To support the low amount of C_3 - C_6

produced over Pd/ZSM-5/ZSM-22, there is a second maximum around C_9 - C_{13} showing a shift away from over cracking because of the presence of higher carbon numbers. The Pd/ZSM-22 (60) product distribution shows that less C_3 - C_6 products are produced compared to the other catalysts, this is evidenced by the height of the C_3 - C_6 maximum obtained over this catalyst. In terms of the C_3 - C_6 maxima, the order of the increasing amounts of C_3 - C_6 hydrocarbons produced over the three catalysts is as follows:

Pd/ZSM-5 > Pd/ZSM-5/ZSM-22 > Pd/ZSM-22

This order of catalytic performance agrees with zeolite acidity, with the ZSM-5 having the strongest acid sites and ZSM-22 being weakly acidic [13]. Therefore, it is expected that the hybrid or mixture of the two zeolites would produce moderate acidity that is intermediate in strength between the two zeolites. Because cracking is acid-catalysed, the zeolite with strongest acid sites would produce high concentrations of cracking products and that with weak acid sites would produce lower concentrations of cracking products, and the moderately acidic one would produce intermediate amounts of cracked products.

3. 4 Conclusions.

A narrow reactor temperature range was investigated, *i.e.*, 215 - 255 ^{o}C, to approximate cracking products obtained by LTFT synthesis conditions, and the WHSV was varied between 0.5 h^{-1} and 1.0 h^{-1}. The catalytic activity of the zeolite-based catalysts in this study was reported in terms of *n*-C_{16} conversion and selectivity to cracked products.

The Pd/ZSM-22 (60) and Pd/ZSM-23 (120) catalysts with high BET surface areas and 100% crystallinity were highly selective to *i*-C_{16}. This suggests that high BET surface area and 100 % relative XRD crystallinity of the acidic support favours isomerisation (*i*-C_{16}). The Pd/ZSM-22 (80), Pd/ZSM-22 (120), Pd/ZSM-23 (60) and Pd/ZSM-23 (80) catalysts were selective to cracking products. Non-ideal hydrocracking behaviour was observed over these catalysts since secondary cracking occurred (*i.e*., C_4/C_{12} >> 1). The Pd/ZSM-23 (60), which is predominantly ZSM-5, achieved the highest cracking products selectivity of 100 % and is similar to what was observed by other researchers when using ZSM-5 as support.

The Pd/ZSM-22 (60) and Pd/ZSM-23 (120) catalysts with high isomerisation selectivity, achieved C_4/C_{12} ratio close to 1, suggesting that almost ideal hydrocracking was achieved over these catalysts. Along this line of reasoning, the Pd/ZSM-5/ZSM-22 behaved in a manner close to that of an ideal hydrocracking catalyst. Because of the secondary cracking observed over the Pd/ZSM-22 (80), Pd/ZSM-22 (120), Pd/ZSM-23 (60) and Pd/ZSM-23 (80), none of these catalysts can be recommended for the hydrocracking of LTFT wax to middle-distillates, since the already produced middle-distillates would be cracked further to undesired light products when processed over these catalysts. On the other hand, the Pd/ZSM-22 (60) and Pd/ZSM-23 (120) would be suitable for diesel dewaxing because of their high selectivity to isomerisation (*i*-C_{16}).

3.5 References

[1] B. Wang, Q. Gao, J. Gao, D. Ji, X. Wang, J. Suo, Synthesis, characterization and catalytic C4 alkene cracking properties of zeolite ZSM-23, Applied Catalysis A: General, volume 274, 2004, pages 167-172.

[2] T. Demuth, X. Rozanska, L. Benco, J. Hafner, R. A. van Santen, H. Toulhoat, Catalytic isomerization of 2-pentene in H-ZSM-22—A DFT investigation, Journal of Catalysis, volume 214, 2003, pages 68-77.

[3] D. Verboekend, K. Thomas, M. Milina, S. Mitchell, J. Perez-Ramirez and J. Gilson, Towards more efficient monodimensional zeolite catalysts: n-alkane hydro-isomerisation on hierarchical ZSM-22, Catalysis Science and Technology, volume 1, 2011, pages 1331-1335.

[4] P. Meriaudeau, V. A. Tuan, V. T. Nghiem, G. Sapaly, C. Naccache, Comparative evaluation of the catalytic properties of SAPO-31and ZSM-48 for the hydroisomerisation of n-Octane: Effect of the Acidity, Journal of Catalysis, volume 185, 1999, pages 435-444.

[5] G. Zhao, J. Teng, Y. Zhang, Z. Xie, Y. Yue, Q. Chen, Y. Tang, Synthesis of ZSM-48 zeolites and their catalytic performance in C4-olefin cracking reactions, Applied Catalysis A: General, volume 299, 2006, pages 167-174.

[6] S. Mehla, Synthesis, characterization and evaluation of zeolites for hydro-isomerization of model feed n-hexadecane, MSc thesis, Indian Institute of Technology – Madras, India, 2012

[7] S. Mehla, K. R. Krishnamurthy, B. Viswanathan, M. John, Y. Niwate, K. Kumar, Shivanand M. Pai, B. L. Newalkar, n-Hexadecane hydroisomerization over Pt/ZSM-12: role of Si/Al ratio on product distribution, Journal of Porous Materials, volume 20, 2013, pages 1023-1029.

[8] G. Busca, Acid catalysts in hydrocarbon chemistry, Chemical Reviews, volume 107, 2007, pages 5366-5410.

[9] M. C. Claude, G. Vanbutsele, J. A. Martens, Dimethyl Branching of Long n-alkanes in the range from decane to tetracosane on Pt/H–ZSM-22 bifunctional catalyst, Journal of Catalysis, volume 203, 2001, pages 213-231.

[10] F. Regali, M. Boutonnet, S. Jaras, Hydrocracking of n-hexadecane on noble metal/silica–alumina catalysts, Catalysis Today, volume 214, 2013, pages 12-18.

[11] C. Ndimande, Ideal hydrocracking catalysts for the conversion of FT wax to diesel, MSc thesis, University of Cape Town, South Africa, 2013.

[12] R. S. Kukard, The effect of zeolite type on the hydrocracking of long n-paraffins, MSc thesis, University of Cape Town, South Africa, 2008.

[13] K. Park, S. Ihm, Comparison of Pt/zeolite catalysts for n-hexadecane hydroisomerisation, Applied Catalysis A : General, volume 203, 2000, pages 201-209.

CHAPTER 4
Conclusions and recommendations

4.1 Conclusions

The aim of this work was to synthesise and characterise zeolites ZSM-22, ZSM-48, ZBM-30 and ZSM-23, as well as test them for potential use as supports to hydrocracking metal catalyst (palladium).

The ZSM-22 zeolites with different SAR were synthesised using HMDA as SDA and different gel pH (12 and 13). XRD analysis revealed that impurity-free ZSM-22 materials can be synthesised using a synthesis gel of pH 12. A higher synthesis gel of pH 13 led to the production of ZSM-22 materials containing impurity phases such as ZSM-5 and cristobalite, which were clearly visible in SEM micrographs, and supported by XRD. It was also observed that the relative % XRD crystallinity increased with decreasing SAR. SEM micrographs showed needle-shaped crystals with lengths in the range 0.6 - 1.2 µm. The 100% crystalline material [ZSM-22 (60)] had the highest BET surface area and the presence of impurities influenced the decrease in BET surface area of the materials.

The ability of the HMDA, pyrrolidine and $HMBr_2$ to direct ZSM-48 material was investigated. Pyrrolidine and HMDA unexpectedly produced ZSM-23 and ZSM-22, respectively. However, impurity-free ZSM-48 structure was directed by $HMBr_2$ at a prolonged synthesis time of 168 h and the XRD patterns showed that amorphous materials were produced at shorter crystallisation times (72 h and 96 h). The SEM images of these materials showed a change in morphology from grain-like to needle-shaped crystals with increasing crystallisation time. Also, good complementarity was observed between SEM and XRD, with XRD-amorphous materials showing amorphousness characteristics in SEM. The large crystals (4.2 - 11.3 µm) obtained led to a low BET surface area of 124 m^2/g. This zeolite was not tested for catalytic activity because of its evasive synthesis at the time of testing.

The attempt to synthesise ZBM-30 using triethylenetetramine (TETA) as SDA produced an amorphous material, as evidenced by the XRD pattern. When a (1 TETA : 1 pyrrolidine) mixture was used to direct the structure of ZBM-30, the XRD pattern showed that a different and unexpected phase (ZSM-39) was produced. The failure to successfully synthesise ZBM-30 deferred catalytic activity tests on these materials.

ZSM-23 synthesis was carried out using pyrrolidine, and impurity-free ZSM-23 materials were successfully synthesised with SAR ≥ 80, as evidenced by XRD analysis. However with SAR = 60, ZSM-5 was produced. Relative % XRD crystallinity of the impurity-free materials increased with an increase in SAR. SEM micrographs showed needle-shaped morphology, and the crystal shape of the ZSM-23 (60) was bundles of rods, which is different to the 100% pure ZSM-23 materials. BET surface area decreased upon the increase of SAR from 80 to 120 and the ZSM-23 (60) *(predominantly ZSM-5)* material had the highest BET surface area.

The Pd/ZSM-22 and Pd/ZSM-23 catalysts were tested for catalytic activity during the hydrocracking of *n*-C_{16}. As the reaction temperature increased the conversion and catalytic cracking selectivity increased over all the catalysts except over Pd/ZSM-22 (120) catalyst. It was found that the Pd/ZSM-22 (60) and Pd/ZSM-23 (120) catalysts, with 100 % crystallinity and higher BET surface area, were highly selective to *i*-C_{16}, and less secondary cracking occurred over these catalysts at 225 ^{o}C. Secondary cracking occurred extensively over the Pd/ZSM-22 (80), Pd/ZSM-22 (120), Pd/ZSM-23 (60) and Pd/ZSM-23 (80) catalysts, as augmented by the high C_4/C_{12} ratio. Amongst the catalysts that were highly selective to cracking products, Pd/ZSM-23 (80) catalyst performed better as a hydrocracking catalyst *(with low C_4/C_{12} ratio)*.

The 0.5 wt. % Pd/ZSM-22 (60) catalyst with the highest isomerisation selectivity was physically mixed with 0.5 wt. % Pd/ZSM-5 (90) catalyst. Hydrocracking over a combination of these catalysts showed that over cracking was minimised compared over Pd/ZSM-5 (90) catalysts, where secondary cracking occurred extensively. Based on the C_4/C_{12} = 1.1, it can be concluded that the physically-

mixed catalyst's behaviour is also close to that of an ideal hydrocracking behaviour.

4.2 Recommendations

These zeolites showed the potential of processing LTFT wax into middle distillate fuels, even though secondary cracking occurred extensively. Extensive secondary cracking normally occurs because of the non-close proximity (non-ideal hydrocracking behaviour) of the metal and acid functions of the bifunctional catalyst. To curb the secondary cracking over these catalysts, two possible routes can be followed :

(i) Since the metal and acid functions are not balanced, varying the palladium loadings to determine the optimum loading for a balance between the two functions (ideal hydrocracking behaviour).

(ii) The addition of oxygenates or water to adsorb on the active sites of the catalysts to decrease the number of acid sites responsible for further cracking.

Appendices

Appendix A1

The intensities of the characteristic peaks of zeolite ZSM-22 used to calculate the relative % XRD crystallinity are shown in table A1. The peaks were numbered from left to right of the XRD pattern in figure 2.2 (shown by asteriks).

Table A1. The intensities of characteristic peaks of ZSM-22 samples.

Peak #	Peak intensities (counts per second)				
	ZSM-22 (60), pH 12	ZSM-22 (80), pH 12	ZSM-22 (120), pH 12	ZSM-22 (80), pH ~ 12	ZSM-22 (120), pH ~ 12
1	595	493	151	562	762
2	119	92	38	112	159
3	149	106	42	135	151
4	615	548	199	449	524
5	471	383	159	380	361
6	190	240	142	190	177
	Total = 2139	Total = 1867	Total = 731	Total = 1828	Total = 2134

Equation 2.1 was used to calculate the relative % crystallinity, *e.g.,* for ZSM-22 (80), pH 12, the % crystallinity was calculated as follows:

$$\frac{\sum \text{of the intensities of the characteristic peaks (sample)}}{\sum \text{of the intensities of the characteristic peaks (reference)}} \times 100 = \% \text{ XRD crystallinity}$$

$$\frac{1867}{2139} \times 100 = \% \text{ XRD crystallinity}$$

$$\% \text{ crystallinity} = 87.3\ \%$$

Appendix A2

The intensities of the characteristic peaks of zeolite ZSM-23 used to calculate the relative % XRD crystallinity are shown in table A2. The six characteristic peaks were numbered from left to right of the XRD pattern in figure 2.8 (shown by asterisks).

Table A2. The intensities of characteristic peaks of ZSM-23 samples.

Peak #	Peak intensities	
	ZSM-23 (SAR = 80)	ZSM-23 (SAR = 120)
1	353	445
2	108	142
3	161	204
4	130	188
5	188	219
6	149	146
	Total = 1089	Total = 1344

Equation 2.1 was also used to calculate the relative % crystallinity of the ZSM-23 materials, *e.g.,* for ZSM-23 (80) the % crystallinity was calculated as follows:

$$\frac{\sum \text{of the intensities of the characteristic peaks (sample)}}{\sum \text{of the intensities of the characteristic peaks (reference)}} \times 100 = \% \text{ crystallinity}$$

$$\frac{1089}{1344} \times 100 = \% \text{ crystallinity}$$

$$\% \text{ crystallinity} = 81.0\ \%$$

Appendix A3

The Scherrer equation below was used to calculate the mean crystallite size of the zeolite materials.

$$L = \frac{\lambda}{\Delta \cos \theta}$$

where:

L is the mean crystallite size;

λ is X-ray wavelength;

Δ is the line broadening at half the maximum intensity;

θ is the Bragg angle.

The figure below shows the XRD pattern of ZSM-22 (60).

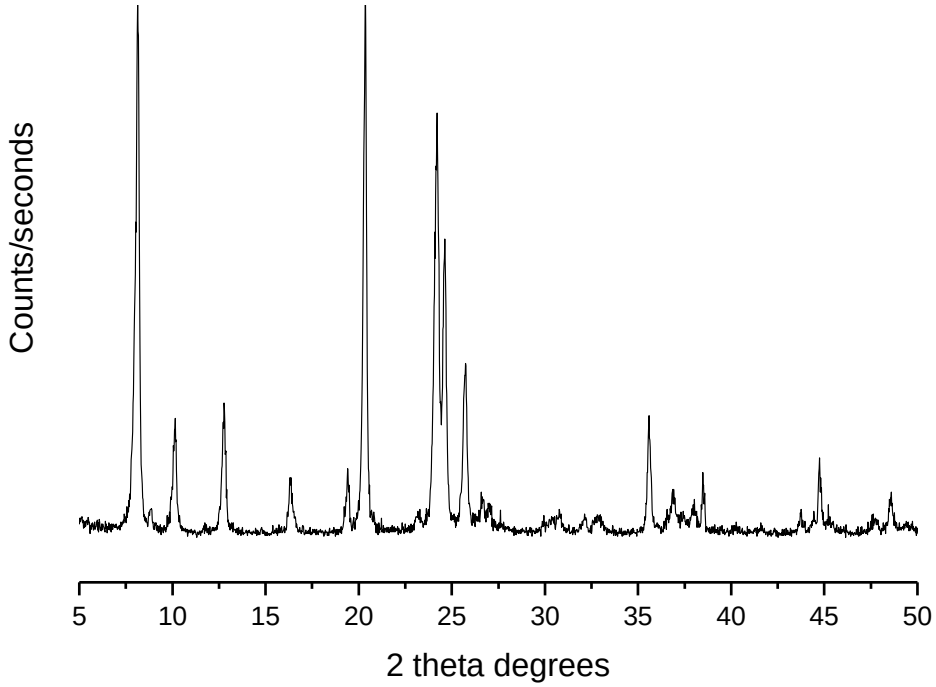

The most intense peak for all the zeolite samples was used to calculate the crystallite size. The XRD pattern of ZSM-22 (60) serves as an example to illustrate how the crystallite sizes of the materials in Chapter 2 were calculated using Scherrer equation.

The figure below shows an expansion of the most intense peak in the region 7.5° - 8.5° 2θ of the XRD pattern of ZSM-22 with a SAR of 60.

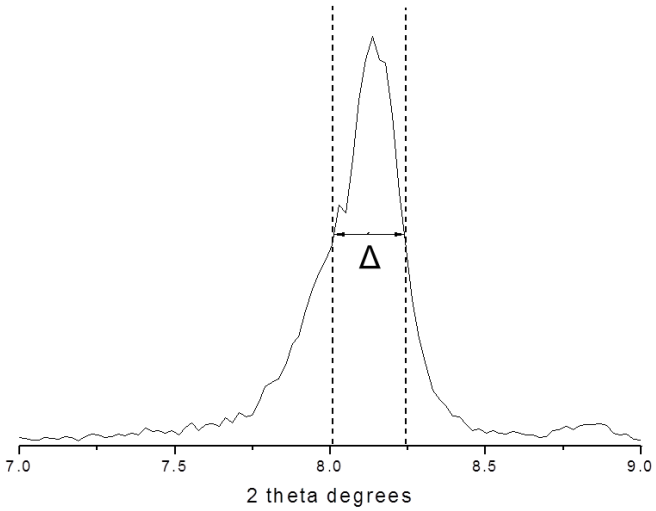

$\lambda = 15.405\ \text{nm}$

$$\Delta = \frac{(8.24 - 8.02)}{2} \times \frac{\pi}{180} = \ 1.92 \times \ 10^{-3}$$

$2\theta = 8.14°$

$$\theta = \frac{8.14°}{2} \ = 4.07°$$

Therefore,

$$\mathrm{L} = \frac{0.15405\ \text{nm}}{\Delta \cos \theta} \ = \ \frac{15.405\ \text{nm}}{1.92 \times \ 10^{-3} \cos \ (4.07°)} \ = 80.4372\ \text{nm} \frac{\mu\text{m}}{10^{3}\text{nm}}$$

$$\mathrm{L} = 0.0804\ \mu\text{m}$$